

ISSN : 0025-0422

JOURNAL  
OF  
THE MAHARAJA SAYAJIRAO UNIVERSITY OF BARODA:  
SCIENCE & TECHNOLOGY

VOL. 56  
2022



Accredited Grade A+ by NAAC

*Published by*

The Maharaja Sayajirao University of Baroda  
Vadodara, Gujarat, India



**JOURNAL  
OF  
THE MAHARAJA SAYAJIRAO UNIVERSITY OF BARODA:  
SCIENCE & TECHNOLOGY**

**Editorial Board**

**V. K. Srivastava**  
Vice Chancellor  
(Editor-in-Chief)

**P. K. Jha**  
(Editor)

**P. T. Deota**  
(Chemical Sciences)

**U. D. Patel**  
(Engineering Sciences)

**K. Muralidharan**  
(Mathematical Sciences)

**Padmaja Sudhakar**  
(Environmental & Geological Sciences)

**Prof. Devarshi Gajjar**  
(Biological & Pharmaceutical Sciences)

**JOURNAL  
OF  
THE MAHARAJA SAYAJIRAO UNIVERSITY OF BARODA:  
SCIENCE & TECHNOLOGY**

**VOL. 56  
2022**

**EDITOR  
Prof. P. K. Jha**



**Accredited Grade A+ by NAAC**

*Published by*  
**The Maharaja Sayajirao University of Baroda**  
**Vadodara, Gujarat, India**

ISSN : 0025-0422

---

**Printed by Shri Jatin H. Somani**, Manager, The Maharaja Sayajirao University of Baroda Press (Sadhana Press), Near Palace Gate, Palace Road, Vadodara, and Edited by **Prof. P. K. Jha**, Editor (Science & Technology) at the Maharaja Sayajirao University of Baroda, Vadodara - 390 002, (India), 2022.

# CONTENTS

<b>Sr.No.</b>	<b>Topic</b>	<b>Page No.</b>
1.	BIOEQUIVALENCE STUDY OF RALTEGRAVIR TABLETS BY DEVELOPING VALIDATED LC-ESI-MS/MS METHOD Dibya Das, Dhiman Halder, Anirbandeep Bose, Tapan Kumar Shaw, Himangshu Sekhar Maji, Tapan Kumar Pal	1-9
2.	CHEMOSELECTIVE STUDY OF SUBSTITUTED BENZYL ALCOHOLSOXIDATION BYMORPHOLINIUM FLUOROCHROMATE IN NON AQUEOUS MEDIUM Jitendra Ojha, Bhawana Arora, Pallavi Mishra	10-17
3.	OPTIMIZATION OF HOMOMORPHIC ENCRYPTION SCHEME FOR WIRELESS SENSOR NETWORKS USING PSO ALGORITHM Sangeeta Rani, Dinesh Kumar & Vikram Singh	18-26
4.	SESIMIC DAMAGE ESTIMATION OF UNIDIRECTIONAL SETBACK TYPE OF 3D IRREGULAR BUILDINGS Hemil M. Chauhan and Kaushal B. Parikh	27-36
5.	INVESTIGATION OF IMPACT OF DIFFERENT CONVENTIONAL AND UNCONVENTIONAL GEOMETRIES OF TALL BUILDING ON WIND FLOW AND DRAG FORCE USING CFD Kamlesh A. Mehta and Rd. Jigar Sevalia	37-46

## Bioequivalence Study of Raltegravir Tablets by Developing Validated LC-ESI-MS/MS Method

Dibya Das<sup>1</sup>, Dhiman Halder<sup>2</sup>, Anirbandeep Bose<sup>3</sup>, Tapan Kumar Shaw<sup>1\*</sup>,  
Himangshu Sekhar Maji<sup>1\*</sup>, Tapan Kumar Pal<sup>2,3</sup>

<sup>1</sup>Department of Pharmaceutical Technology, JIS University, Kolkata-700109, India.

<sup>2</sup>Bioequivalence Study Centre, Dept. of Pharm. Tech., Jadavpur University, Kolkata-700032, India.

<sup>3</sup>TAAB Biostudy Services, 69 Ibrahimpur Road, Jadavpur, Kolkata -700032, India.

Raltegravir is an antiretroviral drug used in the treatment of HIV-1 infection. The determination of Raltegravir containing dosage forms in human plasma already have reported based on different chromatographs techniques were found to be tedious, time-consuming and less cost-effective. So it is essential to develop a cost-effective, simple, less time consuming and non-tedious for determination and quantitation of Raltegravir in human plasma. In this work we have developed a validated high performance liquid chromatography with positive ion electrospray ionization tandem mass spectrometry method (LC-ESI-MS/MS) for rapid determination of Raltegravir levels in human plasma which is cost-effective, simple, less time consuming and non-tedious. The validated method was successfully applied to perform a pharmacokinetic study and bioequivalence of two different tablets, one was test and the other was reference (both containing 400 mg Raltegravir). The pharmacokinetic data demonstrated that the test product was not significantly different with the reference product in terms of AUC (90% confidence interval) and the relative bioavailability of test preparation was found to be 98.94%. The developed analytical method was very efficient and accurate for the estimation of Raltegravir in human plasma and was successfully applied for establishing the bioequivalence of Raltegravir. Hence the objective of this study was to establish the bioequivalence of these two different products Raltegravir by developing a new and validated LC-ESI-MS/MS method.

**Keywords:** Raltegravir, Human plasma, LC-ESI-MS/MS, Bioequivalence.

### 1. Introduction

Raltegravir is an antiretroviral drug used in the treatment of HIV-1 infection. The drug inhibits the activity of HIV-1 integrase, which impedes the insertion of HIV-1 DNA into the host cell genome [1]. The activity of HIV-1 reverse transcriptase, polymerase and human DNA polymerases  $\alpha$ ,  $\beta$ , and  $\gamma$  do not appear to be affected by Raltegravir [2]. Due to an alternative mechanism of action, synergistic activity is seen when the medication is used in combination with other antiretroviral, including reverse transcriptase inhibitors or protease inhibitors. The drug has inhibitory effects on a wide range of clinical isolates of HIV-1 and HIV-2, which is resistant to non-nucleoside reverse transcriptase inhibitors and has reduced susceptibility to protease inhibitors [3].

For comparative pharmacokinetic studies, it is essential to quantify the Raltegravir in human plasma samples. The Literature survey reveals that high

performance liquid chromatography (HPLC) and liquid chromatography-tandem mass spectrometry [4,5] methods have been employed for the determination of Raltegravir in dosage forms and human plasma. Previously reported methods were found to be tedious, time-consuming and less cost-effective. The plasma extraction technique used in the previous studies was also not found to be cost-effective, and the total run time was found lengthy because LC-MS/MS was not used [6]. LC-MS/MS method has been reported for the determination of Raltegravir by negative mode [7].

Hence, the objective of this work was to develop a new validated bioanalytical technique that might be cost-effective, simple, less time consuming and non-tedious for determination and quantitation of Raltegravir in human plasma by LC-ESI-MS/MS method and to apply the same for estimation of different pharmacokinetic parameters; and to justify the bioequivalence of the test product.

### 2. Materials and Methods

#### 2.1 Chemicals and reagents

Raltegravir (API, Purity 97.89%) procured from

---

\*Corresponding author.

Email: hsmaji@jisuniversity.ac.in



Mceuil & Argus Pharmaceuticals Ltd., Haryana, India; the test tablet provided by an Indian company (the sponsor); Reference tablet (Isentress 400mg) manufactured by Merck Sharp &Dohme procured from the local market, Propranolol procured from ShubhamBiopharma, Mumbai, India (used as an internal standard in the chromatography study). Merck Pvt. Ltd, Mumbai, India was chosen to procure acetonitrile, dimethyl sulphoxide (DMSO) and formic Acid (all are HPLC grades). Water was purified to obtain 18.2 MΩ-cm using the Milli-Q gradient system of Millipore (Elix, Milli-Q A10 Academic, Bedford, MA, USA). The CPU (Clinical Pharmacological Unit) of TAAB Biostudy Services, Kolkata, India was chosen to procure the blank human plasma consisting of the anticoagulant EDTA-K3.

## 2.2 Ethical clearance, Volunteer Consenting and Study Design details

The study protocol, Informed Consent Form, Subject Information Sheet, Case Record Form and other related documents were submitted to the HURIP Independent Bioethics Committee, Kolkata, West Bengal, India

[CDSCO Registration No.: ECR/103/Indt WB/2013/RR-19]. For initiation of the study, ethical clearance was obtained before the study. In the presence of a clinical investigator, the study coordinator, volunteers and other study team members were informed about the whole study procedure and its benefits of it. After collecting written informed consent from the volunteers, twenty-four healthy human volunteers were screened and included in the study. Health protection and Volunteers' rights during the study were ensured by the study team and by the ethics committee. The study was randomized, openlabeled, two treatment, two periods and blinded. Due to the comparative pharmacokinetic study, the volunteers have been exposed to both the test and reference drugs. The maintained washout period between the two study periods was 10 Days.

## 2.3 Drug information and Dosing

In the present study, a comparative pharmacokinetic study of single-dose Raltegravir 400 mg manufactured by an Indian company was compared under the framework of BA/BE studies. Isentress 400mg, manufactured by Merck Sharp & Dohme, The Netherlands was used as a reference product. After the clinical and vital parameters examination of the volunteers, they were given either

test or reference product based on the randomization code (Table 1) in each clinical period. The drug was taken with 240±2 ml of drinking water on an empty stomach with at least 10h fasting condition in a single dose without chewing.

Table 1 – Demographic data of Healthy Human Volunteers

	Age (Years)	Height (cm)	Weight (kg)	BMI (kg/m <sup>2</sup> )
Mean ± SD	36.54 ± 6.61	162.96 ± 6.05	58.17 ± 5.39	21.90 ± 1.54
Maximum	45	171	72	23.94
Minimum	25	150	51	19.33

## 2.4 Sampling schedule and Blood collection

Throughout the analysis, volunteers were asked not to change their eating habits. Total of 15 venous blood samples were collected pre-dose (0 h) and the following post-dose intervals of time were 0.5 h, 1.0 h, 2.0 h, 3.0 h, 3.5 h, 4.0 h, 4.5 h, 5.0 h, 6.0 h, 8.0 h, 10.0 h, 12.0 h, 24.0 h and 48.0 h. The sampling was done by the phlebotomist (study team member) [8]. 5ml of blood was taken at each time point. Collected blood samples were centrifuged immediately with EDTA. Plasma was separated and stored frozen at -20 °C with appropriate labeling of the volunteer code number, collection time and study date.

## 2.5 Instrumentation

The liquid chromatographic system consists of a Shimadzu series LC-20 AD Binary pump, CTO-10 AS VP Column oven, SIL 20 AC Autosampler, and CBM-20A Lite System Control Compartment. The LC-ESI-MS/MS system API 2000 with triple quadrupole tandem mass spectrometer (Applied Biosystems/MDS SCIEX,) was used for the quantitative determination of Raltegravir and propranolol (IS) in human plasma. Data acquisition, processing, and quantitation were performed with Analyst 1.6.3 software (Applied Biosystems/ MD SCIEX).

## 2.6 Chromatographic conditions

The mobile phase for the chromatographic separation was done using 0.1% formic acid in Milli-Q water as mobile phase (Pump A) and another mobile phase 0.1% formic acid in acetonitrile (Pump B) in gradient mode, on a Phenomenex Kinetics C18 column (50x3mm; 5µm), the flow rate was 0.5 ml/min and the injection volume was 10µL with a run time of 7.0 minutes with autosampler temperature maintained at 15°C.

## 2.7 Internal Standard (IS) selection

Different types of drug compounds were tested

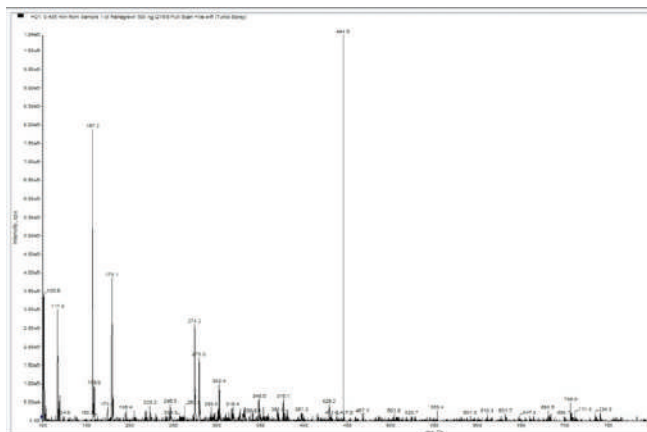


Fig. 1 – The Q1 scan of Raltegravir

for the selection of a suitable IS during the method development, like letrozole, diclofenac, tolbutamide, metoprolol and propranolol. Finally, propranolol was selected as IS for its excellent response, good peak shape and rapid elution rate. It has also shown high recovery, chromatographic and ionization properties with the analyte. In the selected mobile phase and column, propranolol (IS) showed no interference with the performance as well as the intensity of molecular ion peak in the mass spectrometric analysis remained unaffected and co-eluted properly.

### 2.8 Mass spectrometry

The mass spectra of the compounds were determined using a turbo electrospray ionization interface with multiple reaction monitoring. Positive ionization mode was used for the measurement of ions. Optimization of tuning parameters was done by injecting 100 ng/ml of standard solution, which contained Raltegravir (Analyte) and propranolol (IS) at 10 ml/min by using an external syringe pump that was directly affixed to the mass spectrometer. Needle spray was done at an applied high voltage was 5.5 kV. A scan Dwell (ms) time of 200.00 msec was used to program the instrument. Raltegravir (the analyte) and propranolol (IS) were measured using the MRM transition of  $m/z$  445.300  $\rightarrow$  361.100,  $m/z$  260.300  $\rightarrow$  116.100, respectively, other mass spectrometric conditions are for Raltegravir and propranolol DP (V): 65 and 33, FP (V): 399 and 393, CXP: 19.66 and 15.03, CE (eV): 33 and 28, EP (V): 8.60 and 8.50 respectively. 400°C was set as the turbo ion spray source temperature along with a voltage of 5500.00 V. The nebulizer gas (GS1) had a value of 55.00 psi. Accompanied by a turbo ion spray gas (GS2) at 45 psi 30.00 and 5.00 (arbitrary scale) were the curtain gas (CUR) and the collision-associated

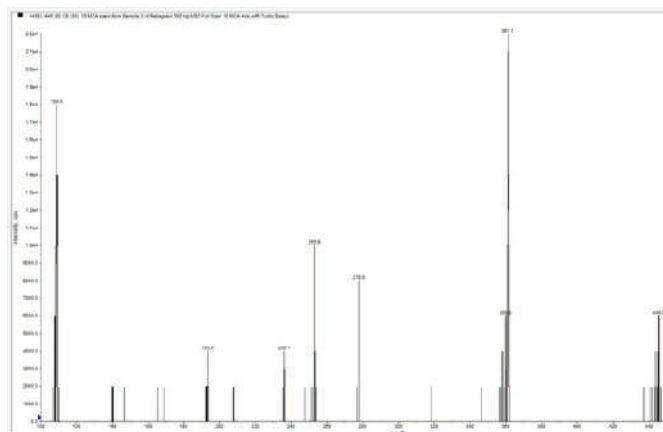


Fig. 2 – The MS2 scan of Raltegravir

dissociation (CAD) gas flow, respectively, that were maintained in the instrument. The Q1 scan and MS2 scan of Raltegravir are shown in Fig. 1 and Fig. 2 respectively. Fig. 3 shows the MRM chromatogram of Raltegravir and IS in plasma.

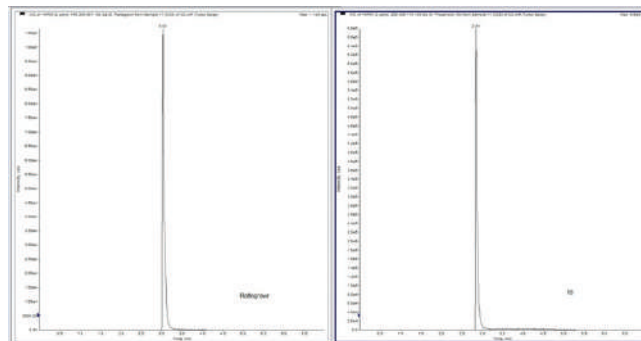


Fig. 3 – MRM chromatogram of Raltegravir and IS in plasma

### 2.9 Preparations of Standard solutions

Using DMSO, 1 mg/ml of Raltegravir and IS solutions were prepared respectively. Further dilution of these solutions with the mobile phase was made to attain a stock solution of 8  $\mu$ g/ml for IS and 10  $\mu$ g/ml for Raltegravir. Further dilution of these stock solutions was made to attain eight working solutions for calibration standards. All solutions were kept at a temperature of 2-8°C. The prepared concentrations were 62.5 ng/ml, 125 ng/ml, 250 ng/ml, 500 ng/ml, 1000 ng/ml, 2000 ng/ml, 4000 ng/ml, and 8000 ng/ml.

### 2.10 Preparations of quality control samples

The eight-point standard calibration solutions of Raltegravir were used to prepare four types of quality control samples: LLOQ, LQC, MQC and HQC. The calibration concentration of the LLOQ has the lowest at 62.50 ng/ml. The middle concentration of the second (125 ng/ml) and third (250 ng/ml) calibration concentrations, i.e. the LQC was 187.5 ng/ml.



Similarly, the middle concentration of the sixth (2000 ng/ml) and seventh (4000 ng/ml) of the calibration concentrations, i.e. the MQC had a concentration of 3000 ng/ml. Likewise, the middle concentration of the seventh (4000 ng/ml) and eighth (8000 ng/ml) of the calibration concentrations, i.e. the HQC had a concentration of 6000 ng/ml.

### 2.11 Preparations of the calibration curve

By spiking appropriate analyte and IS in blank human plasma, eight-point standard calibration solutions of Raltegravir were prepared to yield final concentrations. The QC samples of LLOQ, LQC, MQC, and HQC were prepared at three concentration levels of the analyte. Using the concentration on the X-axis and a peak area ratio of the drug and IS on Y-axis, the calibration curve was plotted.

### 2.12 Sample preparation

The protein precipitation technique was used for the extraction of the drug from plasma sample collected [9,10,11,12]. A blank plasma sample of 100 $\mu$ l was added to a 2ml plastic micro-centrifuge tube. 50 $\mu$ l of both the working solutions of IS [8  $\mu$ g/ml] and Raltegravir was spiked into the blank plasma sample and vortexed for a minute. Following this, 300 $\mu$ l ice-cold acetonitrile was added and further vortexed for another 10 min. The resulting sample was centrifuged at 12000rpm at 4 $^{\circ}$ C for 5min. 250 $\mu$ l of the upper organic layer was transferred to the autosampler vials, and 10 $\mu$ l aliquot of the collected layer was injected into the chromatographic system [13,14].

## 3. Bioanalytical method validation

### 3.1 Selectivity

Separate healthy human volunteers were selected for the collection of blank plasma for the establishment of selectivity of the method. For determination of the selectivity, the lower limit of quantification or LLOQ level was used. As per the USFDA and EMA guidelines, the acceptance criteria for selectivity are that the analyte area response should not be more than 20% in the blank than the LLOQ at retention time. [15,16]

### 3.2 Carryover

To analyze the possibility of interference of an injected run from an immediate previous run, blank samples were injected after HQC sample. If the carryover from a high concentration injection is <20% of the area of LLOQ, it qualifies under USFDA and EMA. [15,16]

### 3.3 Sensitivity

The sensitivity method was confirmed by injecting the spiked plasma level at LLOQ five times. The USFDA and EMA guidelines state that the analyte peak area at LLOQ has to be higher than five times the blank's peak area. USFDA guide states that the accuracy of the injected LLOQ samples should be within  $\pm 20\%$  of the coefficient of variation (CV %). [15,16]

### 3.4 Linearity

The eight-point (62.5 ng/ml, 125 ng/ml, 250 ng/ml, 500 ng/ml, 1000 ng/ml, 2000 ng/ml, 4000 ng/ml, and 8000 ng/ml) standard calibration curve the linearity was evaluated through regression analysis. The standard calibration curve was constructed, taking the drug/IS ratio on Y-axis and concentration on X-axis to determine the correlation coefficient ( $R^2$ ) of the standard curve [15,16,17].

### 3.5 Accuracy

Five replications of four different concentrations (LLOQ, LQC, MQC, and HQC) were used for the evaluation of the accuracy of the method. The ratio of the drug to IS peak area was determined, and the line equation ( $y=mx+c$ ) was used to back-calculate the concentration. The deviation of the estimated back-calculated value from the theoretical concentration was determined to calculate the accuracy. As per the guideline of USFDA and EMA, the acceptance criteria for accuracy is  $\pm 15\%$  of the theoretical concentration except at LLOQ, where it should be within  $\pm 20\%$  [15,16,18].

### 3.6 Precision

The precision of the analytical procedure was assessed after injecting the spiked plasma samples into five replicates at LLOQ, LQC, MQC, and HQC levels. For the back-calculated concentrations for the repeated injections, the CV percent was calculated. The CV percent of the response of injections injected on the same day was used to determine intraday precision. The CV percent of the measured values of the samples injected on various days was used to determine inter-day accuracy. According to the guidelines set out by the USFDA and the EMA [15,16,19].

### 3.7 Extraction Recovery

The determination of the potentiality of the sample preparation using the Protein Precipitation Technique (PPT) to extract Raltegravir and IS from biological

samples was done by comparison of chromatographic responses found in LQC, MQC and HQC levels of extracted samples to that of the un-extracted samples of similar concentration corresponding 100% recovery.

### 3.8 Matrix Effect

The plasma constituents' effect over the ionization of the analyte and IS was determined by comparing the chromatographic responses of the extracted (Post) LQC, MQC and HQC samples with the analyte's response from neat samples at equivalent concentrations.

### 3.9 Stability

There are different types of stability studies performed here to estimate the drug stability in plasma; there are autosampler stability, freeze-thaw stability, benchtop stability, long-term stability, and short-term stability. The Blank Human plasma was spiked with the analyte and IS at the concentration of three quality control LQC, MQC, and HQC in five replicates followed by extraction and analyzed after completing the suitable storage condition for individual stability tests. For testing the stabilities of the analyte in the stock, the solution was analyzed by freshly preparing the Quality Control samples from the stock solution before the study. For analysis of the short-term stability study, the spiked plasma sample was stored for 24 hours at -20°C before extraction. The Freeze and thaw stability study was done by storing samples at -20°C and exposed to three repeated freeze and thaw cycles by freezing at -20°C and thawing at normal laboratory conditions. The samples were kept in an autosampler maintained at 15°C for 24 hours before injecting to determine the autosampler stability. The samples were kept on abenchtop maintained at room temperature or normal

laboratory conditions for 24 hours before injecting to determine the benchtop stability. A Long-term stability study was done by storing the spiked plasma sample for 12 days at -20°C before extraction and analysis. Freshly spiked Quality Control sample at HQC, MQC, and LQC was used to determine the stability testing accuracy against the stability samples. If it is within  $\pm 15\%$ , then it is acceptable under USFDA and EMA guidelines [15,16,20].

## 4. Results and Discussions

### 4.1 Selectivity

Blank plasma samples devoid of response and which indicated no interference of plasma at RT comparable to Raltegravir was observed in the chromatograms. Hence, the requirements of selectivity were met by the selectivity method as the peak area at RT in blank samples showed a deviation of  $\leq 20\%$  when compared to that of analyte LLOQ.

### 4.2 Carryover

The Raltegravir RT was devoid of any response when injected after HQC, in a blank chromatogram. The developed method was free of carryover problems as the analyte peak response was lower than 20% of LLOQ.

### 4.3 Sensitivity

At LLOQ, the blank's peak area was  $>5x$  in comparison to the peak area of the analyte. The precision (%CV) values of 0.078% to 7.86% were observed for the Raltegravir. Hence, the developed method was sensitive because the LLOQ concentration was found 62.50 ng/ml in plasma.

### 4.4 Linearity

The R<sup>2</sup> value of 0.9965 (Fig.4) was recorded for

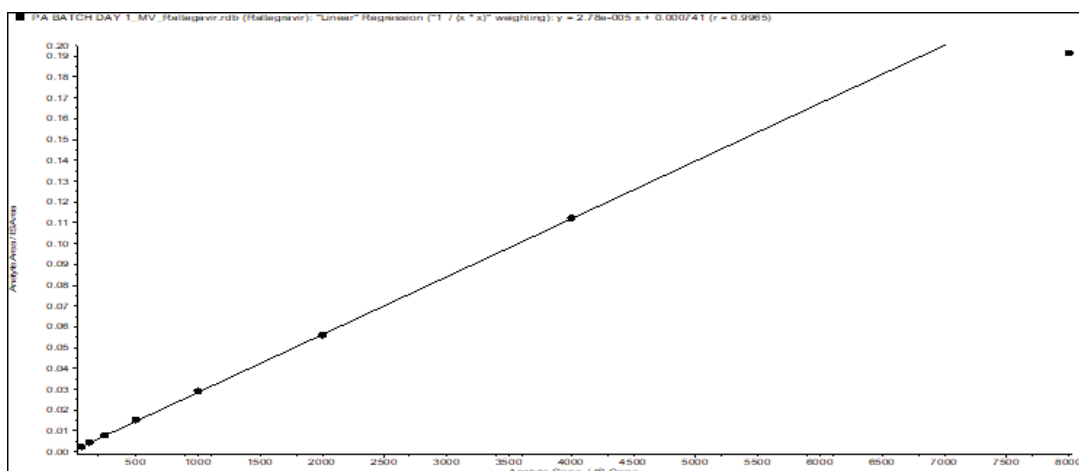


Fig. 4 – Plasma calibration curve of Raltegravir

the seven points calibration curve of Raltegravir. 85.91%-105.66% was the mean accuracy seen for Calibration concentration for Raltegravir. Hence, the developed method has linearity present over a range of concentration of 62.50 ng/ml to 8000 ng/ml for the analyte.

#### 4.5 Accuracy

The Quality Control samples, whose concentrations were back-calculated, lay within the 90.25% to 99.09% of accuracy range for Raltegravir for all five replicates, including LLOQ. Accuracy values fell within the USFDA guidelines for LLOQ within  $\pm 20\%$ , MQC, and LQC and HQC  $\pm 15\%$  as depicted in the results. Table 2 and Table 3 show the results of inter-day and intra-day accuracy studies, respectively.

Table 2 – Interday-accuracy (Between Run)

Quality control	Concentration (ng/ml)	Run	Mean found (ng/ml)	SD	CV (%)	Accuracy (%)
LLOQ	62.5	1	56.404	3.615	6.408	90.25
		187.5	61.934	8.440	13.627	99.09
		3000	60.630	3.754	6.192	97.01
LQC	187.5	1	186.108	15.298	8.220	99.26
		2	203.572	16.019	7.869	108.57
		3	200.062	9.304	4.651	106.70
MQC	3000	1	2816.998	241.091	8.558	93.90
		2	3351.148	191.318	5.709	111.70
		3	2887.606	941.962	11.842	96.25
HQC	6000	1	5451.146	327.926	6.061	90.85
		2	6592.004	713.777	10.828	109.87
		3	5255.280	735.836	14.002	87.59

Table 3 – Intra-day-accuracy (Within Run)

Quality control (ng/ml)	Concentration	Mean found	SD	CV (%)	Accuracy (%)
LLOQ	62.5	66.10	0.771	1.166	105.76
LQC	187.5	192.508	14.718	7.646	102.67
MQC	3000	2717.540	145.359	5.349	90.58
HQC	6000	5150.158	345.801	6.714	85.84

#### 4.6 Precision

For the Raltegravir, the inter-day CV% of the back-calculated concentrations, including that of the LLOQ lay within 4.651% to 14.002%. For intra-day,

the range was determined to be 1.166% to 7.646% for Quality Control samples prepared on three different days. Table 2 and Table 3 showcase the results of intra-day and inter-day experiments, respectively, which satisfies the establishment of repeatability of the method within the acceptance criteria.

#### 4.7 Extraction Recovery

The mean extraction recovery for Raltegravir at the Quality Control levels was 90.07% to 107.05%. For this drug analysis, the developed method of sample preparation is perfect. Hence, it shows high extraction efficiency for the analyte. Table 4 shows the result of the extraction recovery.

Table 4 – Extraction Recovery

Quality Control (ng/ml)	Diluent Sample			In Plasma Sample		
	LQC	MQC	HQC	LQC	MQC	HQC
Concentration	187.75	3000	6000	187.75	3000	6000
Mean found	208.28	3045.75	5085.00	187.59	2794.57	5443.45
% Recovery				90.07	91.75	107.05

#### 4.8 Matrix effect

Evaluation of the matrix effect was done by the analysis of three batches of Quality Control samples HQC, MQC, and LQC for the analyte.  $\pm 15\%$  was the average matrix effect value obtained for the analyte. Table 5 shows the result of the matrix effects of the analyte. Insignificant changes were seen.

Table 5 – Matrix effect (Analyte)

Quality Control (ng/ml)	Concentration	Mean found	SD	CV (%)	Mean found (ng/ml)	SD	CV (%)	% OF ME
LQC	187.75	193.13	9.51	4.92	210.41	12.92	6.14	92.02
MQC	3000	2934.73	132.76	4.52	3307.44	247.71	7.49	89.18
HQC	6000	5326.79	116.09	2.18	5472.44	791.31	14.46	98.81

#### 4.9 Stability

All tested stability conditions of the Raltegravir are found stable, including 24 hours on the benchtop, 24 hours in autosampler, three freeze-thaw cycles, 24 hours short term stability, and 12 days long term

Table 6 – Stability Studies

Stability	Quality control (ng/ml)	Concentration	Mean found	Accuracy (%)
Freshly Thawed	LQC	187.75	192.37	
	MQC	3000	2767.15	
	HQC	6000	5335.75	
Benchtop (24 Hours)	LQC	187.75	174.17	90.54
	MQC	3000	2944.48	106.41
	HQC	6000	5218.60	97.80
Autosampler (24 Hours)	LQC	187.75	200.68	104.32
	MQC	3000	3003.38	108.54
	HQC	6000	5760.36	107.96
Freeze-thaw (3 Cycles)	LQC	187.75	202.41	105.22
	MQC	3000	2729.97	98.66
	HQC	6000	5532.14	103.68
Short term (24 Hours)	LQC	187.75	108.73	93.95
	MQC	3000	2944.98	106.43
	HQC	6000	5486.54	102.83
Long term (12 Days)	LQC	187.75	192.00	99.89
	MQC	3000	9080.00	111.31
	HQC	6000	5480.00	102.70

stability. The samples accuracy of all the run at LQC, MQC and HQC levels was within  $\pm 15\%$  of the analyte. Table 6 shows the results of all the stability studies.

### 5. Application of LC-ESI-MS/MS method in comparative pharmacokinetic study in healthy human volunteers

Under fasting conditions with a single dose of administration, the comparative pharmacokinetic study was carried out on 24 healthy human volunteers. The volunteers were exposed to both test and reference preparations. Administration of the reference preparation, Isentress 400mg containing Raltegravir 400mg produced the maximum plasma concentration that is 4078.225 ng/ml ( $C_{max}$ ) at the time 1.583 hr. ( $t_{max}$ ). The test preparation of tablet formulation containing identical doses of the drug produced the  $C_{max}$  of 3956.881 ng/ml at the time 1.667 hr. ( $t_{max}$ ) for Raltegravir. The other comparative pharmacokinetic parameters are also shown in Table 7. Moreover, Table 8 shows 90% CI Calculation. Fig. 5 shows a representative MRM chromatogram of the volunteer plasma sample of Raltegravir and IS and Fig. 6 shows the Mean Plasma concentration-time profile of Raltegravir.

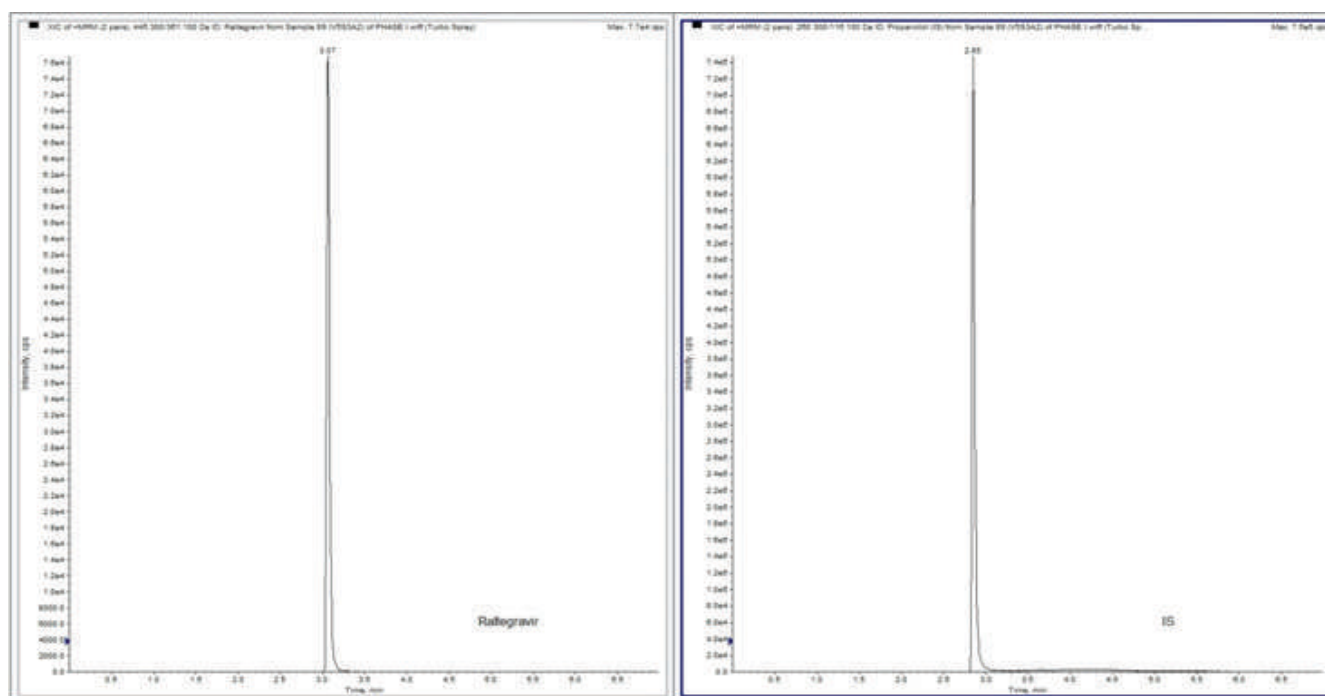


Fig. 5 – Representative MRM chromatogram of volunteer plasma sample of Raltegravir and IS.

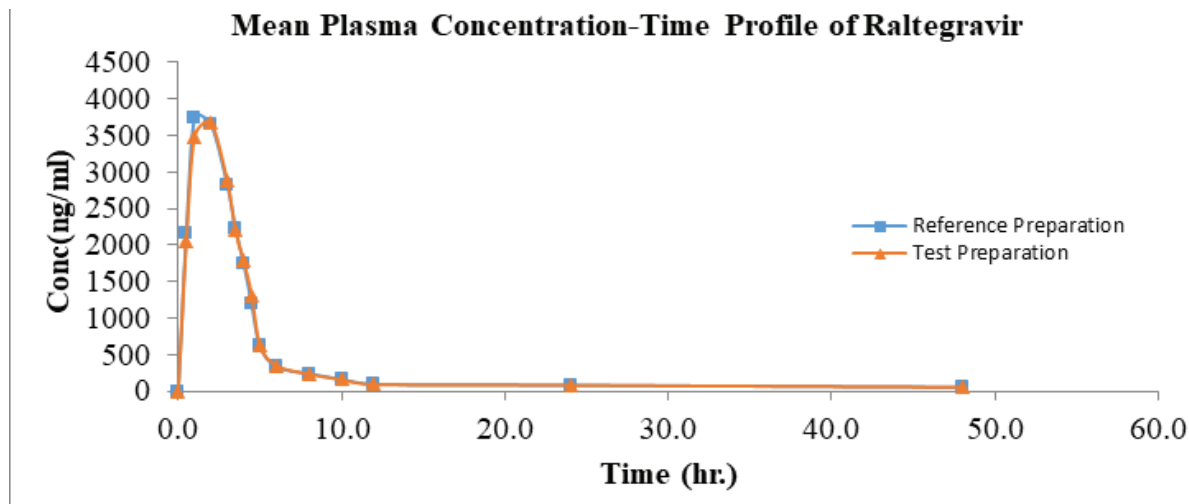


Fig. 6 – Mean Plasma concentration-time Profile of Raltegravir

Table 7 – Pharmacokinetic parameters in 24 volunteers with the test and reference preparation

Pharmacokinetic parameters	Reference Preparation (A1)	Test Preparation (A2)
$C_{max}$ (ng/ml)	Mean 4078.225 ± SD. 400.410	Mean 3956.881 ± SD. 509.903
$t_{max}$ (hr.)	Mean 1.583 ± SD. 0.584	Mean 1.667 ± SD. 0.482
$AUC_{0-t}$ (ng. hr./ml)	Mean 16762.439 ± SD. 1583.222	Mean 16585.291 ± SD. 1853.264
$AUC_{0-\infty}$ (ng. hr./ml)	Mean 17397.039 ± SD. 1632.358	Mean 17212.125 ± SD. 1876.924
$k_{el}$ (hr. <sup>-1</sup> )	Mean 0.088 ± SD. 0.010	Mean 0.088 ± SD. 0.008
$t_{1/2}$ (hr.)	Mean 7.974 ± SD. 0.775	Mean 7.948 ± SD. 0.600
Relative Bioavailability (%)	100 %	98.94%

Table 8 – 90% CI Calculation

	Untransformed	Ln Transformed
$C_{max}$	M = 0.967, 90% CI [0.90153, 1.03247]	M = 0.996, 90% CI [0.98794, 1.00406]
$AUC_{0-t}$	M = 0.988, 90% CI [0.93428, 1.04172]	M = 0.999, 90% CI [0.99363, 1.00437]
$AUC_{0-\infty}$	M = 0.988, 90% CI [0.93663, 1.03937]	M = 0.999, 90% CI [0.99363, 1.00437]
Relative Bioavailability	98.94%	

## 6. Conclusion

The bioanalytical method development for Raltegravir is highly sensitive, selective, and rugged. Moreover, found very simple and reproducible. And the validated LC-ESI-MS/MS method provided a reliable and rugged approach for the determination and quantitation of the drug Raltegravir in human plasma in the positive ionization mode. Previously Raltegravir was estimated by HPLC-UV in human plasma and the run time takes more than 10 minutes per sample. But in this, work only 7 minutes (per sample) was the run time. For this reason, this work was cost effective due to less solvent used, less current consumption, non-tedious and more productivity. The protein precipitation technique procedure afforded highly selective separation of the analyte from endogenous components enabling quantification of 62.50 ng/ml–8000 ng/ml on-column per sample injection employing 100  $\mu$ l plasma samples. The method was extensively validated for stability under different storage conditions and matrix effect. It was successfully applied in a clinical study. Throughout the pharmacokinetic study, there were no discomforts or adverse event were occur or reported after administration of the test and reference tablet formulation to the volunteers. Accounting to the relative bioavailability of test preparation was found to be 98.94%. The two formulations were considered bioequivalent because of the rate and extent of absorption within 80%–125% confidence interval. In this whole study, no SAE was found in any healthy human volunteers; therefore we may conclude that the test formulation was found to be safe.



## Acknowledgement

The authors are thankful to M/S, TAAB Biostudy Services, Kolkata-700032 and its entire team, for conducting this clinical study on healthy human volunteers and providing the necessary instrumental facilities.

## References

- 1 "HIV Antiretroviral Agents in Development" the body.com
- 2 Isentress (Raltegravir): US prescribing information. Whitehouse Station (NJ): Merck and Co, Inc. 2012.
- 3 T. Sudha, P. Shanmugasundram, Development and validation of RP-HPLC and HPTLC chromatographic methods of analysis for the quantitative estimation of raltegravir potassium in pharmaceutical dosage form. *Res. J. of Pharm. and Tech.*, 4(11), 1746-1750, 2011.
- 4 A. D'Avolio, L. Baietto, M. Siccardi, M. Sciandra, M. Simiele, V. Oddone, S. Bonora, G. Di Perri, An HPLC-PDA method for the simultaneous quantification of the HIV integrase inhibitor raltegravir, the new nonnucleoside reverse transcriptase inhibitor etravirine, and 11 other antiretroviral agents in the plasma of HIV-infected patients. *Therapeutic drug monitoring*, 30(6), 662-669, 2008.
- 5 J. F. Jourdil, M. Bartoli, F. Stanke-Labesque, Lack of specificity for the analysis of raltegravir using online sample clean-up liquid chromatography–electrospray tandem mass spectrometry. *J of Chromatography B*, 877(29), 3734-3738, 2009.
- 6 S. Notari, C. Tommasi, E. Nicastri, R. Bellagamba, M. Tempestilli, L. P. Pucillo, P. Narciso, P. Ascenzi, Simultaneous determination of maraviroc and raltegravir in human plasma by HPLC-UV. *IUBMB life*. 61(4), 470-475, 2009.
- 7 A. Gupta, S. Guttikar, P. A. Shah, G. Solanki, P. S. Shrivastav, M. Sanyal, Selective and rapid determination of raltegravir in human plasma by liquid chromatography–tandem mass spectrometry in the negative ionization mode. *J. of pharma. Analy.*, 5(2):101-109, 2015.
- 8 [extranet.who.int/pqweb/sites/default/files/documents/BE\\_raltegravir\\_January2021.pdf](http://extranet.who.int/pqweb/sites/default/files/documents/BE_raltegravir_January2021.pdf)
- 9 D. Halder, S. Dan, P. Sarkar, D. Das, U. H. Chandra, T. K. Pal, LC-MS/MS determination of 4-hydroxynimesulide, an active metabolite of nimesulide and application to bioequivalence study in Indian subjects. *Eu. J. of Mass Spec.*, 25(5):399-411, 2019.
- 10 R. Solanki, B. P. Nagori, M. K. Naval, J. Banerjee, Development and validation of simultaneous estimation method for amoxicillin trihydrate and tinidazole in tablet dosage form by rp-hplc. *Asi.J. of Pharmaceut. Ana.*, 3(2):66-71, 2013.
- 11 K. N. Kaushik, S. K. Banerjee, UV Spectrophotometric method development for the determination of domperidone in tablet formulation. *Asi. J. of Res. in Chem.* 2(4):432-433, 2009.
- 12 S. S. Patil, S. D. Barhate, A. S. Patil, A. V. Patil, H. K. Patil, P. A. Salunke, R. S. Wagh, Novel Mixed Hydrotropic Solubilisation technique for Analytical method development and validation of Acyclovir in bulk and tablet formulation by Spectrophotometry. *As. J. of Pharmaceut. Ana.* 9(1), 25-29, 2019.
- 13 M. Sumithra, P. Yuvanesh, A. Mistry, Analytical method development and validation of ambroxol hydrochloride by UV spectroscopy and forced degradation study and detection of stability. *Asi. J. of Res. in Chem.*, 9(7):794, 2016.
- 14 B. M. Ishaq, V. S. Rajan, S. A. Parameswari, N. Amruth, M. Madhu, C. M. Chetty. Analytical Method Development and Validation of Erlotinib by High Performance Liquid Chromatography. *Res. J. of Pharm. and Tech.*, 4(11):1787-1790, 2011.
- 15 US Department of Health and Human Services. Bioanalytical method validation, guidance for industry. <http://www.fda.gov/cder/guidance/4252fnl.htm>. 2001.
- 16 European Medicines Agency. Guideline on bioanalytical method validation. European Medicines Agency. 2011 Jul 21.
- 17 D. Das, D. Halder, A. Bose, T. K. Shaw, C. Saha, P. K. De, H. S. Maji, T. K. Pal. Determination of Metformin and Sitagliptin in healthy human volunteers blood plasma and its bioequivalence study under fasting condition. *Int. J. of Appl. Pharmaceut.*, 14(6), 42–50. 2022.
- 18 D. Das, D. Halder, A. Bose, C. Saha, H. S. Maji, T. K. Pal. Bioequivalence study of Azelnidipine 16mg tablet to evaluate pharmacokinetic profile of single dose in healthy, adult, human volunteers under fasting condition. *Int. J. of Appl. Pharmaceut.* 13(6), 154-159. 2021.
- 19 D. Das, D. Halder, A. Bose, H. S. Maji, T. K. Pal. Pharmacokinetic determination of Methylprednisolone in Indian healthy volunteers by LC-MS/MS. *J. of Med. Pharm. and Alli. Sci.* 10(3), 2740-2744. 2021.
- 20 D. Das, D. Halder, H. S. Maji, P. K. De, T. K. Pal. Special Emphasis on Bioanalytical method Development and Validation of an Anti-Hypertensive Drug Azelnidipine by LC-ESI-MS/MS in Healthy Human Volunteer's Blood Plasma" *Res. J. of Pharm. and Tech.*. 14(7), 3572-3578. 2021.



## Chemoselective Study of Substituted Benzyl Alcohol Oxidation by Morpholinium Fluorochromate in Non Aqueous Medium

Jitendra Ojha, Bhawana Arora, Pallavi Mishra\*

Department of Chemistry, J N V University, Jodhpur 342 001, India.

Morpholinium fluorochromate (MFC) is a mild oxidizing agent and we have used it for the specific oxidation of some monosubstituted benzyl alcohols in the dimethyl sulphoxide solution. Corresponding benzaldehydes were the products obtained after oxidation. The reaction was first order both in MFC and the substituted benzyl alcohols. All kinetic studies were done using non aqueous conditions. P-toluene sulphonic acid as catalyst was used for our reactions. KIE was confirmed by the oxidation of  $\alpha$ ,  $\alpha$ -dideuteriobenzyl alcohol ( $\text{PhCD}_2\text{OH}$ ). Different organic solvents were used to study the reaction kinetics. Multi-parametric equations were used to study solvent effect. Ortho, para and meta substituents effect were also studied on the oxidation rate, using Charlton's multiparametric equations. The value of  $\eta$  was obtained positive, clearly suggesting that rate-determination step involves an electro-positive reaction centre. Suitable mechanism has also been suggested.

**Keywords:** Benzyl alcohol, oxidation, morpholinium fluoro chromate, solvent analysis, kinetics, mechanism.

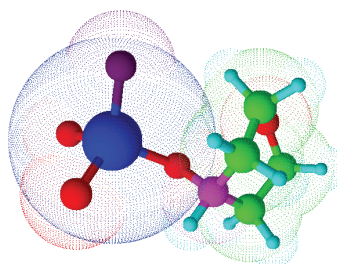
### Introduction

Halochromates have always been associated with the oxidation of different organic molecules in the process of organic synthesis. They are basically very mild and specific oxidizing reagents used for the study of reaction kinetics [1]. Morpholinium Fluorochromate (MFC) is also one such oxidizing agent, which is commonly used for the oxidation of different organic compounds [2]. We have chosen substituted benzyl alcohols as substrate. They are aromatic, transparent and water-soluble liquids which are polar and nontoxic in nature. Due to their water and alcohol solubility, they undergo selective oxidation in the presence of non protic solvent and forms corresponding benzaldehydes, which are commercially used in the food items for enhancing almond flavour, in the pharmaceuticals and in plastics as an additive. Thus, oxidation of mono substituted benzyl alcohols is very important process commercially.

In continuance of our previous work [3-6], in this article we report the oxidation kinetics of some mono substituted benzyl alcohols by MFC in which we have used DMSO as a solvent, resulting in the formation of corresponding benzaldehydes. This work has not been reported so far in the DMSO, which is

an aprotic solvent. We have also tried to correlate reactivity and structure in this reaction.

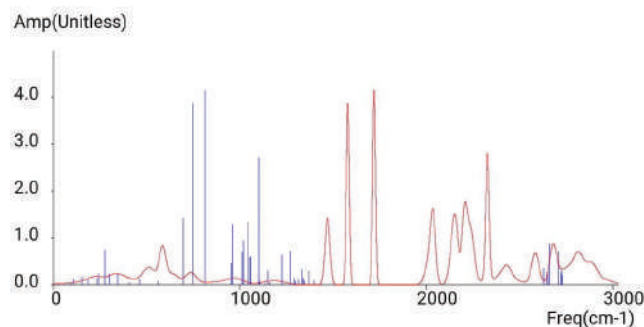
### Experimental Materials:



MFC 3D structure



MFC



MFC: IR Spectrum

We have prepared MFC by the method already reported [2] and we have used iodometric method

\*Corresponding author.  
Email: pallavianuk@gmail.com

to check its purity. The purification of alcohols was done by the method described earlier [7].  $\alpha$ ,  $\alpha$ -Dideuteriobenzyl alcohol ( $\text{PhCD}_2\text{OH}$ ) was also formed by the given method [8]. Its isotopic purity was found out by the NMR spectra, which was  $96 \pm 3\%$ . Para toluenesulphonic acid (TsOH) was used as  $\text{H}^+$  ions source. Solvent's purification was done by their usual reported methods [9].

### Product analysis:

We have done the product analysis under kinetic conditions. For this in a typical experiment, we have taken different substituted benzyl alcohols (5.4 g, 0.05mol) and MFC (3.10 g, 0.01mol). The solutions were made up to 50  $\text{cm}^3$  in DMSO and set aside in the dark for 15 hr to make sure the completion of the reaction. This is important to avoid auto oxidation. Then we treated the solution with saturated solution of DNP with HCl and kept it in the refrigerator overnight. Now we filtered off the precipitated DNP, dried and weighed it, recrystallized it by using ethanol, and weighed it again. The DNP yields before and after recrystallization were 2.64 g (92%) and 2.34 g (82%), respectively. The mixed m.p. of this DNP was found similar with the m.p. of the DNP of corresponding benzaldehyde. Oxidation state of Cr in the entirely reduced reaction mixtures was determined iodometrically and was found to be  $3.90 \pm 0.16$ .

### Kinetic measurement:

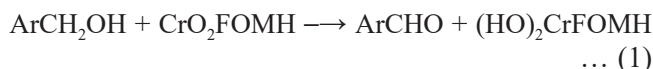
We have maintained a large excess ( $\times 15$ ) of the Benzyl alcohols over MFC to attain the pseudo-first order conditions. We have used DMSO as solvent and followed their actions, at constant temperatures ( $\pm 0.1$  K), by observing the gradual reduction in the MFC concentration spectrophotometrically at 356 nm. No considerable absorption was shown by other reactant or product at 356 nm. Linear plots of  $\log [\text{MFC}]$  versus time for up to 80% of the reaction ( $r = 0.990 - 0.998$ ) indicated pseudo-first order rate constant,  $k_{\text{obs}}$ . The rate constants were reproducible with in  $\pm 3\%$ . The second order rate constant was obtained by the relation:  $k_2 = k_{\text{obs}}/[\text{alcohol}]$ . No PTS was used in the reactions where effect of  $\text{H}^+$  was not studied.

### Results and Discussions

We have obtained rates and all other experimental data for all the given substituted benzyl alcohols. As the results are similar, we have reproduced only representative data here.

### Stoichiometry:

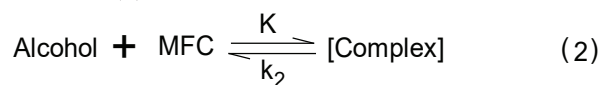
Corresponding benzaldehydes were formed by the substituted benzyl alcohols oxidation by MFC. Products analysis and the stoichiometric determinations point toward the following overall reaction (1). Here H of ( $-\text{CH}_2$ ) is different for different benzyl alcohols.



Thus, there is a two electron change in this reaction by MFC. It is also in conformance with the earlier studies with MFC [3-6]. Both PFC [10] and PCC [11] also work on the same line and are reduced to the chromium (IV) species, which can be shown by deciding the oxidation state of the chromium.

### Rate laws:

The reactions show first order kinetics w.r.t. the MFC. A typical kinetic run is represented in Fig. 1. Moreover  $k_{\text{obs}}$  (pseudo-first order rate constant) is not dependent on the initial concentration of MFC. Table 1 clearly shows that as the concentration of the alcohols increases, the rate of reaction also increases. But it is nonlinear. A graph between  $1/k_{\text{obs}}$  and  $1/[\text{Alcohol}]$  was straight line ( $r > 0.996$ ) with an intercept on the rate-ordinate (Fig. 2), which shows that Michaelis-Menten type of kinetics is involved w.r.t. the alcohols. This leads the following overall mechanism (2) and (3) and rate law (4).



$$\text{Rate} = k_2 K [\text{Alcohol}] [\text{MFC}] / (1 + K [\text{Alcohol}]) \quad (4)$$

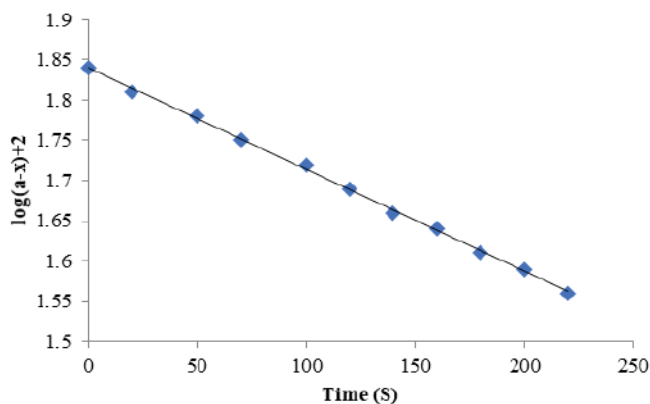


Fig. 1 – The Benzyl alcohol oxidation by MFC:  
A typical kinetic run

The dependence of rate of reaction on the reductant concentration was calculated at various given temperatures. The double reciprocal plots helped in evaluating the values of  $K$  and  $k_2$ . The calculation of the formation constants for the complex formation (thermodynamic parameters) and the dissociation constant of the complex's decomposition (activation parameters) were done from the values of  $K$  and  $k_2$ , respectively at given temperatures (Tables 3 and 4).

### Tests for free radicals:

The benzyl alcohol oxidation by MFC, in nitrogen atmosphere failed to induce the acrylonitrile polymerization. Further, an addition of a radical scavenger, acrylonitrile, had no effect on the rate (Table 1).

Table 1 – Rate constants for the benzyl alcohol oxidation by MFC at 308 K

$10^3[\text{MFC}]$ ( $\text{molL}^{-1}$ )	[Alcohol] ( $\text{molL}^{-1}$ )	[TsOH] ( $\text{molL}^{-1}$ )	$10^4 k_{\text{obs}}$ ( $\text{s}^{-1}$ )
1.0	0.1	1.0	12.5
1.0	0.2	1.0	17.2
1.0	0.3	1.0	22.0
1.0	0.5	1.0	24.6
1.0	0.8	1.0	25.9
1.0	1.0	1.0	26.8
1.0	0.8	1.0	28.4
1.0	0.8	1.0	30.1
2.0	0.8	1.0	22.2
4.0	0.8	1.0	23.8
6.0	0.8	1.0	22.9
8.0	0.8	1.0	22.5
1.0	1.0	1.0	21.1*

\*Contained 0.001 mol L<sup>-1</sup> acrylonitrile

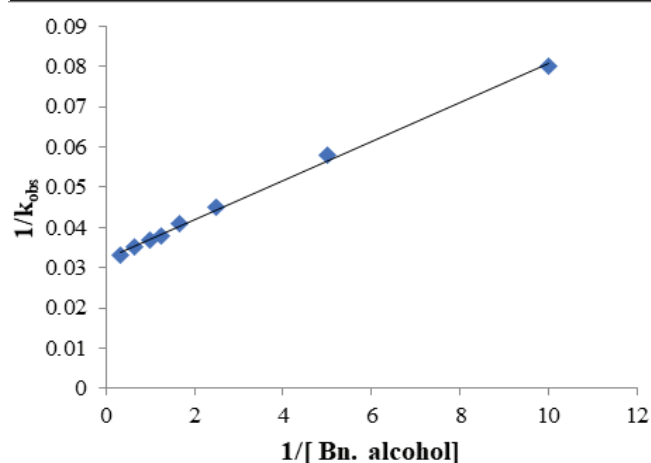


Fig. 2 – The benzyl alcohol oxidation by MFC:  
A double reciprocal plot

### Effect of acidity:

The hydrogen ions were used to catalyze the reaction. Dependence of the hydrogen-ion has been shown in the form of  $k_{\text{obs}} = a + b[\text{H}^+]$  (Table 2).

Table 2 – Dependence of rate of reaction on hydrogen-ion concentration

[Bn. Alcohol] 0.10 mol L <sup>-1</sup>	[MFC] 0.001 mol L <sup>-1</sup>	Temperature 308 K				
[TsOH]/mol L <sup>-1</sup>	0.10	0.20	0.40	0.60	0.80	1.00
$10^4 k_{\text{obs}}/\text{s}^{-1}$	14.3	16.1	18.6	21.8	26.6	27.5

Table 3 – Rate constants and activation parameters of oxidation of substituted bn. alcohols by MFC

Subst.	$10^4 k_2$ ( $\text{L mol}^{-1} \text{s}^{-1}$ )				$\Delta H^*$ $\text{kJ mol}^{-1}$	$-\Delta S^*$ $\text{J mol}^{-1} \text{K}^{-1}$	$\Delta G^*$ $\text{kJ mol}^{-1}$
	288 K	298 K	308 K	318 K			
H	6.64	13.4	28.8	59.4	53.3±1.0	45±3	66.5±0.9
p-Me	12.6	26.5	58.9	102	51.4±1.3	46±4	64.8±1.1
p-OMe	25.4	50.6	103	207	50.8±0.8	42±2	63.2±0.6
p-Cl	4.67	8.58	18.0	38.8	51.4±2.1	55±6	67.5±1.6
p-Br	4.62	8.40	17.9	37.2	50.8±1.9	57±6	67.5±1.5
p-F	6.06	11.8	26.5	56.0	54.3±1.6	42±5	66.7±1.3
p-NO <sub>2</sub>	1.18	2.54	5.10	9.98	51.6±0.1	65±1	70.7±1.2
p-CO <sub>2</sub> Me	1.91	3.87	7.90	14.9	49.8±0.4	67±1	69.6±0.3
p-CF <sub>3</sub>	1.64	3.26	6.46	12.9	49.7±0.8	69±2	70.0±0.6
p-CN	1.41	2.88	5.83	11.1	49.9±0.3	69±1	70.3±0.2
p-SMe	14.7	30.9	61.8	112	49.2±0.5	52±1	64.5±0.4
p-NHAc	12.4	25.8	54.0	106	52.1±0.4	44±1	64.9±0.3
p-NMe <sub>2</sub>	119	237	469	842	47.4±0.4	41±1	59.5±0.3
m-Me	10.6	21.9	47.1	88.4	51.7±0.6	46±2	65.3±0.5
m-OMe	10.2	20.1	43.5	85.8	51.9±1.0	46±3	65.5±0.8
m-F	3.75	6.95	13.9	26.8	47.6±1.1	69±3	68.1±0.9
m-Cl	3.20	6.41	12.7	24.9	49.5±0.5	64±2	68.4±0.4
m-NO <sub>2</sub>	1.26	2.55	5.06	10.2	50.4±0.7	68±2	70.6±0.6
m-CF <sub>3</sub>	1.64	3.23	6.46	12.9	49.8±0.8	68±2	70.0±0.7
m-CO <sub>2</sub> Me	1.91	4.26	7.77	15.6	50.0±1.0	66±3	69.5±0.8
m-Br	3.15	6.32	12.6	24.0	49.1±0.3	65±1	68.4±0.3
m-NHAc	7.23	13.8	29.1	60.6	51.6±1.5	50±5	66.4±1.2
m-CN	1.19	2.91	5.76	10.5	52.5±1.6	61±5	70.5±1.3
m-SMe	7.86	15.6	32.7	65.1	51.4±0.9	50±2	66.1±0.7
o-Me	44.4	97.3	182	354	49.7±0.7	41±2	61.8±0.6
o-OMe	37.2	76.8	155	290	49.7±0.2	43±1	62.3±0.2
o-NO <sub>2</sub>	1.35	2.66	5.34	10.8	50.2±0.9	69±3	70.5±0.7
o-CO <sub>2</sub> Me	5.61	10.3	21.9	43.5	49.9±1.6	58±5	67.1±1.2
o-F	7.50	14.7	30.9	62.4	51.5±1.1	50±3	66.2±0.8
o-Cl	11.1	22.8	47.1	93.9	51.7±0.5	46±2	65.2±0.4
o-Br	14.7	28.2	58.9	110	49.0±0.9	53±2	64.6±0.7
o-I	22.8	45.3	93.0	173	49.2±0.5	48±2	63.5±0.4
o-CN	2.00	4.62	8.31	16.5	50.2±1.3	65±4	69.4±1.0
o-NHAc	57.0	110	221	407	47.7±0.6	46±2	61.3±0.4
o-SMe	54.3	107	209	389	47.5±0.3	47±1	61.4±0.2
o-CF <sub>3</sub>	8.84	19.2	39.9	78.6	52.9±0.1	43±4	65.7±0.9
α,α'-BA	1.90	3.82	7.64	15.2	50.2±0.6	66±2	69.6±0.5
$k_H/k_D$	3.49	3.50	3.77	3.91			

The values of  $a$  and  $b$  for benzyl alcohol are  $8.95 \pm 0.64 \times 10^{-4} \text{ s}^{-1}$  and  $15.3 \pm 1.05 \times 10^{-4} \text{ mol}^{-1}\text{L s}^{-1}$ , respectively ( $r^2 = 0.9814$ ).

### Kinetic isotope effect:

The cleavage of  $\alpha\text{-C-H}$  bond in the rate-determination step is a very important step in establishing the reaction mechanism course. For this we have studied the oxidation of  $\alpha$ ,  $\alpha$ -di-deuterio benzyl alcohol and found out that indeed bond cleavage is taking place in the rate determining step. The presence of significant primary K. I. E. has also been shown by our results (Table 3).

### Effect of solvents:

Effect of different organic solvents on the oxidation of substituted benzyl alcohols was studied. As MFC reacts with primary and secondary alcohols, the selection of solvents was restricted by the solubility of MFC and its reaction with primary and secondary alcohols. There was no reaction with other solvents chosen by us. As oxidation process showed similar kinetics in all the solvents, we have shown representative data for benzyl alcohol. The values of  $k_2$  are given in Table 5.

A linear correlation ( $r^2=0.9270$ ) was observed between the activation enthalpies and entropies of oxidation of 33 substituted benzyl alcohols, indicating that a compensation effect is taking place [12]. The isokinetic relationship was established by Exner's [13] plot between  $\log k_2$  at 288 K and at 318 K, which was found linear ( $r^2 = 0.9978$ ) (Fig. 3). The isokinetic temperature's value calculated from the Exner's plot

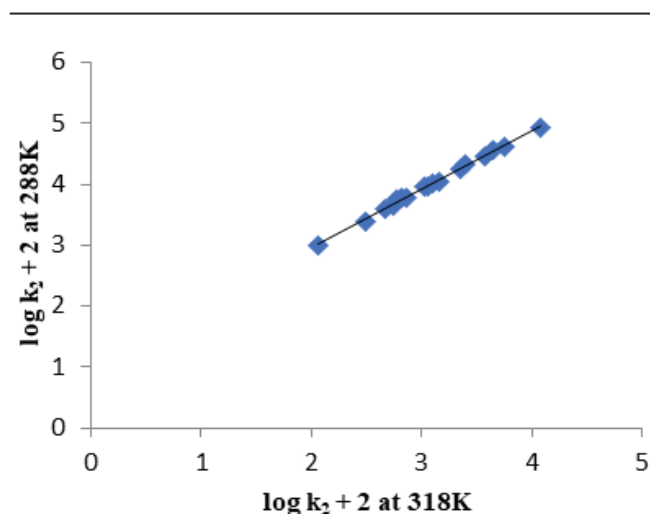


Fig. 3 – Exner's isokinetic relationship in the benzyl alcohols oxidation by MFC

was  $662 \pm 34 \text{ K}$ . The linear isokinetic correlation suggested that in our study oxidation of all the mono substituted Benzylalcohols are taking place by same mechanistic pathway and the changes in the rate of reaction are taking place because of changes in the entropy and enthalpy of activation.

Table 4 – Formation constants for the formation of MFC-Bn. alcohol complex and thermodynamic parameters

Subst.	$10^4 k (\text{dm}^3 \text{ mol}^{-1})$				$-\Delta H^*$ $\text{kJ mol}^{-1}$	$-\Delta S^*$ $\text{J mol}^{-1} \text{ K}^{-1}$	$-\Delta G^*$ $\text{kJ mol}^{-1}$
	288 K	298 K	308 K	318 K			
H	7.95	7.30	6.67	5.95	11.0±0.4	14±1	7.0±0.3
p-Me	7.13	6.53	5.85	5.24	10.4±0.3	11±1	7.1±0.2
p-Ome	6.82	6.20	5.53	4.95	10.7±0.3	13±1	6.9±0.2
p-Cl	6.90	6.25	5.69	5.00	10.5±0.4	12±1	7.0±0.3
p-Br	6.68	6.03	5.40	4.81	10.8±0.2	14±1	6.9±0.2
p-F	6.41	6.79	5.17	4.55	11.2±0.3	15±1	6.8±0.3
p-NO <sub>2</sub>	6.60	5.85	5.21	4.61	11.6±0.1	16±1	6.9±0.1
p-COOMe	7.00	6.35	5.78	5.13	10.3±0.3	11±1	7.1±0.2
p-CF <sub>3</sub>	6.59	5.96	5.35	4.70	11.0±0.4	14±1	6.9±0.3
p-CN	7.09	6.45	5.85	5.24	10.1±0.2	11±1	7.1±0.2
p-SMe	6.87	6.23	5.60	4.95	10.8±0.3	13±1	7.0±0.3
p-NHAc	7.18	6.53	5.90	5.25	10.4±0.3	11±1	7.1±0.2
p-NMe <sub>2</sub>	7.22	6.57	5.96	5.33	10.2±0.2	11±1	7.1±0.2
m-Me	7.23	6.61	5.96	5.33	10.2±0.3	11±1	7.2±0.2
m-OMe	6.90	6.26	5.65	5.03	10.5±0.3	12±1	7.0±0.2
m-F	7.15	6.50	5.86	5.26	10.3±0.2	11±1	7.1±0.2
m-Cl	6.85	6.23	5.60	4.97	10.6±0.3	13±1	7.0±0.2
m-NO <sub>2</sub>	6.50	5.86	5.26	4.60	11.2±0.4	15±1	6.9±0.3
m-CF <sub>3</sub>	7.04	6.45	5.77	5.17	10.4±0.3	12±1	7.1±0.2
m-CO <sub>2</sub> Me	6.54	5.90	5.30	4.67	10.9±0.3	14±1	6.9±0.2
m-Br	6.77	6.14	5.54	4.90	10.6±0.3	13±1	6.9±0.2
m-NHAc	7.21	6.55	5.92	5.35	10.1±0.1	10±1	7.1±0.1
m-CN	7.30	6.68	6.03	5.42	10.1±0.2	10±1	7.2±0.2
m-SMe	7.10	6.48	5.82	5.25	10.2±0.2	11±1	7.1±0.2
o-Me	7.00	6.37	5.75	5.15	10.3±0.2	11±1	7.1±0.2
o-Ome	6.97	6.35	5.73	5.06	10.6±0.4	12±1	7.1±0.3
o-NO <sub>2</sub>	6.86	6.25	5.61	4.96	10.7±0.4	13±1	7.0±0.3
o-COOMe	7.24	6.63	6.00	5.33	10.2±0.4	11±1	7.2±0.3
o-F	7.18	6.57	5.91	5.33	10.1±0.2	10±1	7.1±0.2
o-Cl	6.68	6.03	5.44	4.80	10.8±0.3	14±1	6.9±0.2
o-Br	6.73	6.11	5.48	4.85	10.8±0.3	13±1	6.9±0.3
o-I	7.16	6.55	5.91	5.29	10.2±0.3	11±1	7.1±0.2
o-CN	6.54	5.90	5.30	4.67	10.9±0.3	14±1	6.9±0.2
o-NHAc	6.49	5.86	5.25	4.60	11.2±0.4	15±1	6.9±0.3
o-SMe	6.98	6.30	5.64	5.03	10.8±0.2	13±1	7.0±0.2
o-CF <sub>3</sub>	6.68	6.03	5.43	4.80	10.8±0.3	14±1	6.9±0.2
$\alpha,\alpha'$ -BA	7.04	6.45	5.80	5.22	10.1±0.3	11±1	7.1±0.2

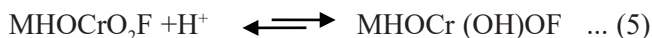


Table 5 – Solvent effect on the benzyl alcohol oxidation by MFC at 298 K

Solvents	K (L <sup>-1</sup> mol <sup>-1</sup> )	10 <sup>4</sup> k <sub>2</sub> (s <sup>-1</sup> )	Solvents	K (L <sup>-1</sup> mol <sup>-1</sup> )	10 <sup>4</sup> k <sub>2</sub> (s <sup>-1</sup> )
Chloroform	7.66	44.9	Toluene	7.85	18.9
1,2-Dichloroethane	8.61	52.7	Acetophenone	7.43	59.0
Dichloromethane	7.68	43.4	THF	7.22	29.2
DMSO	7.53	128	t-butyl alcohol	7.47	22.5
Acetone	7.65	47.3	1,4-Dioxane	7.56	25.8
DMF	7.66	74.1	1,2-Dimethoxyethane	6.81	19.3
Butanone	6.47	33.4	CS <sub>2</sub>	7.69	15.2
Nitrobenzene	6.24	58.9	Acetic acid	7.21	17.4
Benzene	7.96	14.0	Ethyl acetate	6.62	24.5
Cyclohexane	6.92	2.20			

### Correlation analysis of reactivity:

A protonated Cr (VI) species formation has been postulated earlier in the reactions of the halochromates, which are structurally similar [3-6].



The rate constants,  $k_2$ , of various solvents used by us were interrelated in terms of L. S. E. R. (linear solvation energy relationship) (equation 6) of Kamlet et al [14].

$$\log k_2 = A_0 + p\pi^* + b\beta + a\alpha \quad \dots(6)$$

In Eq. (6)  $\pi^*$  represents the solvent polarity,  $\beta$  represents the hydrogen bond acceptor basicity's and  $\alpha$  represents the hydrogen bond donor acidity.  $A_0$  is the intercept term. The results of correlation analysis of the solvents are shown in terms of Eq. 6 (Kamlet equation). The results were not correct as per Exner's criterion [13]. As shown in the equation 7  $r^2$  values were in the range of .081-. 087. Which are not correct.

$$\log k_2 = -3.86 + 1.74 (\pm 0.20) \pi^* + 0.18 (\pm 0.18) \beta + 0.11 (\pm 0.16) \alpha \quad \dots(7)$$

$$R^2 = 0.8709; \text{sd} = 0.18; n = 18; \psi = 0.39$$

$$\log k_2 = -3.89 + 1.78 (\pm 0.19) \pi^* + 0.14 (\pm 0.15) \beta \quad \dots(8)$$

$$R^2 = 0.8665; \text{sd} = 0.18; n = 18; \psi = 0.39$$

$$\log k_2 = -3.86 + 1.82 (\pm 0.18) \pi^* \quad \dots(9)$$

$$r^2 = 0.8892; \text{sd} = 0.18; n = 18; \psi = 0.39$$

$$\log k_2 = -2.86 + 0.45 (\pm 0.38) \beta \quad \dots(10)$$

$$r^2 = 0.0817; \text{sd} = 0.46; n = 18; \psi = 0.99$$

Here  $n$  is the number of data points and  $\psi$  is Exner's statistical parameter [15]. The results were not correct as per Exner's criterion [13].  $R^2$  values were in the

range of .081-. 087 As shown in the equation 7-10. Thus, above Kamlet's [19] tri -parametric equation was discarded. Then Swain's equation was used to analyze the data of the solvent effect [16] which gives the cation- and anion-solvating conception of the solvents, it is represented by equation 8.

$$\log k_2 = a A + b B + C \quad \dots(11)$$

Here A shows is the solvents anion-solvating power and B shows the solvents cation-solvating power. C is an intercept and (A + B) is used to differentiate the solvent polarity. The rates in different solvents were given in terms of equation (11), separately with A and B and with (A + B).

$$\log k_2 = 0.74 + (\pm 0.05) A + 1.80 (\pm 0.04) B - 3.87 \quad \dots(12)$$

$$R^2 = 0.9940; \text{sd} = 0.04; n = 19; \psi = 0.08$$

$$\log k_2 = 0.49 (\pm 0.59) A - 2.85 \quad \dots(13)$$

$$r^2 = 0.0350; \text{sd} = 0.48; n = 19; \psi = 1.01$$

$$\log k_2 = 1.76 (\pm 0.13) B - 3.85 \quad \dots(14)$$

$$r^2 = 0.9111; \text{sd} = 0.15; n = 19; \psi = 0.31$$

$$\log k_2 = 1.46 \pm 0.14 (A + B) - 3.90 \quad \dots (15)$$

$$r^2 = 0.8609; \text{sd} = 0.18; n = 19; \psi = 0.38$$

The oxidation rates of benzyl alcohols in various solvents have an admirable correlation in Swain's equation (12) with the cation-solvating power, which plays a main role. Actually, cation-solvating power accounts for *ca.* 99% of the data. The solvent polarity indicated by (A + B), also accounted for *ca.* 87% of the data. On the other hand, when a graph between  $\log$  (rate) against the inverse of the comparative permittivity was plotted it was not linear ( $r^2 = 0.5391$ ,  $\text{sd} = 0.32$ ,  $\psi = 0.92$ ). So, Swain's equation was also ruled out. Hammett equation [17] or with dual substituent-parameter equations [18,19] were also ruled out due to ortho substitution. Finally, Chartons [20] triparametric LDR equation for quantitative description of structural effects on the chemical reactivities were used. LDR equation (16) has been applied for the rate constants,  $k_2$  in this work.

$$\log k_2 = L \sigma_1 + D \sigma_d + R \sigma_e + h \quad \dots (16)$$

Here,  $\sigma_1$  is a localized (field and/or inductive) effect parameter,  $\sigma_d$  is the intrinsic delocalized electrical effect parameter and  $\sigma_e$  represents the sensitivity of the substituent towards the changes in the active centre. The  $m$  and  $p$  substituent parameters are correlated by equation (17).

$$\sigma_D = \eta \sigma_e + \sigma_d \quad \dots(17)$$

Here  $\eta$  shows the electronic demand of the reaction site and it is given by  $\eta = R/D$ , and  $\sigma_D$  represents the delocalized electrical parameter of the diparametric LD equation. For *ortho*-substituted compounds, it is necessary to account for the possibility of steric effects and Charton [20], therefore, modified the LDR equation to generate the LDRS equation (18).

$$\log k_2 = L \sigma_1 + D \sigma_d + R \sigma_c + S v + h \quad \dots (18)$$

where  $v$  is the familiar Charlton's steric parameter based on Vander Waals radii [21].

The oxidation rates of *ortho*, *meta* and *para* monosubstituted benzyl alcohols showed an exceptional correlation in terms of LDR/LDRS equations (Table 4). Standard deviation (sd), the coefficient of multiple determination ( $R^2$ ), and Exner's [19] parameter,  $\psi$ , have been used by us for our analysis.

The assessment of the L and D values for the substituted benzyl alcohols showed that the *para*-substituted benzyl alcohols oxidation is more responsive towards the delocalization effect than to the localized effect. Whereas *meta* and *ortho* substituents were dependent on the field effect. A decrease in the reaction constants with the increasing temperature indicates that selectivity is decreased with the increasing temperature.

The negative value of deterioration coefficients, L, D and R, suggested an electron-deficient carbon centre in the activated complex in the rate-determining step. The positive value of  $\eta$  suggested that electron-donating substituent stabilizes cationic species. The positive value of S indicated that the reaction steric acceleration takes place by an *ortho*-substituent.

To test the importance of localized, delocalized and steric effects in the *ortho* substituted benzyl alcohols, multiple regression analyses were carried out with (i)  $\sigma_1$ ,  $\sigma_d$  and  $\sigma_c$  (ii)  $\sigma_d$ ,  $\sigma_c$  and  $v$  and (iii)  $\sigma_1$ ,  $\sigma_c$  and  $v$ . The absence of significant correlations showed that all the four substituent constants are significant.

$$\log k_2 = -1.55 (\pm 0.42) \sigma_1 - 1.60 (\pm 0.34) \sigma_d - 3.48 (\pm 1.93) \sigma_c - 2.54 \dots (19)$$

$$R^2 = 0.8252; \text{sd} = 0.29; n = 12; \psi = 0.48$$

$$\log k_2 = -1.69 (\pm 0.46) \sigma_d - 1.82 (\pm 2.84) \sigma_c + 0.87 (\pm 0.52) v - 3.48 \dots (20)$$

$$R^2 = 0.6679; \text{sd} = 0.40; n = 12; \psi = 0.66$$

$$\log k_2 = -2.02 (\pm 0.65) \sigma_1 - 0.45 (\pm 3.12) \sigma_c + 1.29 (\pm 0.58) v - 2.63 \dots (21)$$

$$R^2 = 0.5986; \text{sd} = 0.72; n = 12; \psi = 0.72$$

When *para*- and *meta*-substituted benzyl alcohols oxidation was subjected to the multiple regression analysis, it clearly indicated that field effects (both localized and delocalized) are very important. There was no major collinearity between a range of substituent constants for the 3 series. The percent involvement [26] of the delocalized effect, PD, is given by equation (22-24).

$$P_D = (|D| \times 100) / (|L| + |D|) \quad \dots (22)$$

Similarly, the percent contribution of the steric parameter [25] to the total effect of the substituent,  $P_S$ , was determined by using equation (23).

$$P_S = (|S| \times 100) / (|L| + |D| + |S|) \quad \dots (23)$$

The values of  $P_D$  and  $P_S$  are also recorded in Table 5. The value of  $P_D$  for the *para*-substituted benzyl alcoholsoxidation is *ca.* 52% while the subsequent values for the *meta*- and *ortho*-substituted alcohols are *ca.* 40% and 45% respectively. This shows that the balance of localization and delocalization effects is different for differently substituted benzyl alcohols. The extent of the  $P_S$  value shows that the steric effect is considerable in this reaction.

Table 6 – Temperature dependence for reaction constants for the substituted benzyl alcoholsoxidation by MFC

T/K	-L	-D	-R	S	$\eta$	$R^2$	sd	$\Psi$	$P_D$	$P_S$
Para – Substituted										
288	1.78	1.97	1.55	-	0.77	0.9997	0.008	0.02	52.4	-
298	1.69	1.87	1.42	-	0.74	0.9998	0.007	0.01	52.4	-
308	1.60	1.79	1.30	-	0.71	0.9998	0.009	0.01	52.7	-
318	1.50	1.70	1.22	-	0.70	0.9998	0.006	0.01	53.0	-
Meta – Substituted										
288	1.96	1.34	1.18	-	0.86	0.9998	0.006	0.02	40.5	-
298	1.87	1.24	1.07	-	0.85	0.9999	0.006	0.01	39.8	-
308	1.78	1.15	0.99	-	0.84	0.9998	0.003	0.02	39.2	-
318	1.70	1.05	0.92	-	0.86	0.9999	0.004	0.01	38.2	-
Ortho– Substituted										
288	1.88	1.61	1.25	1.26	0.76	0.9999	0.008	0.01	46.0	26.4
298	1.77	1.51	1.22	1.14	0.79	0.9998	0.003	0.02	45.9	25.7
308	1.68	1.41	1.12	1.06	0.78	0.9999	0.003	0.01	45.5	25.5
318	1.60	1.32	1.09	0.96	0.81	0.9999	0.007	0.01	45.1	24.7



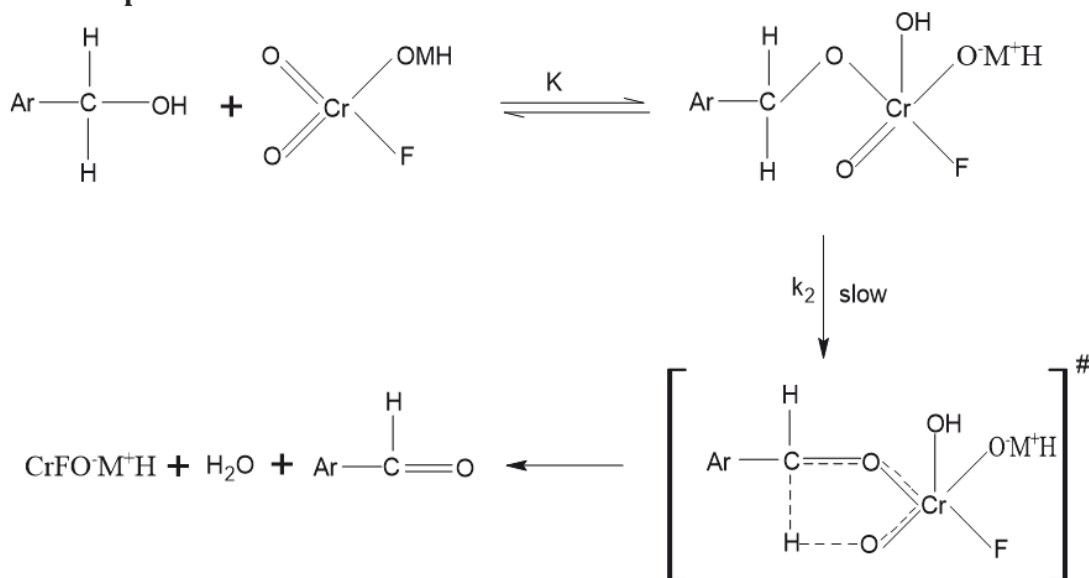
Entropy (S) values were found to be positive which clearly indicated that the reaction is accelerated by the steric effect. This may be due the generation of high ground states energy by the sterically crowded alcohols.

### MECHANISM

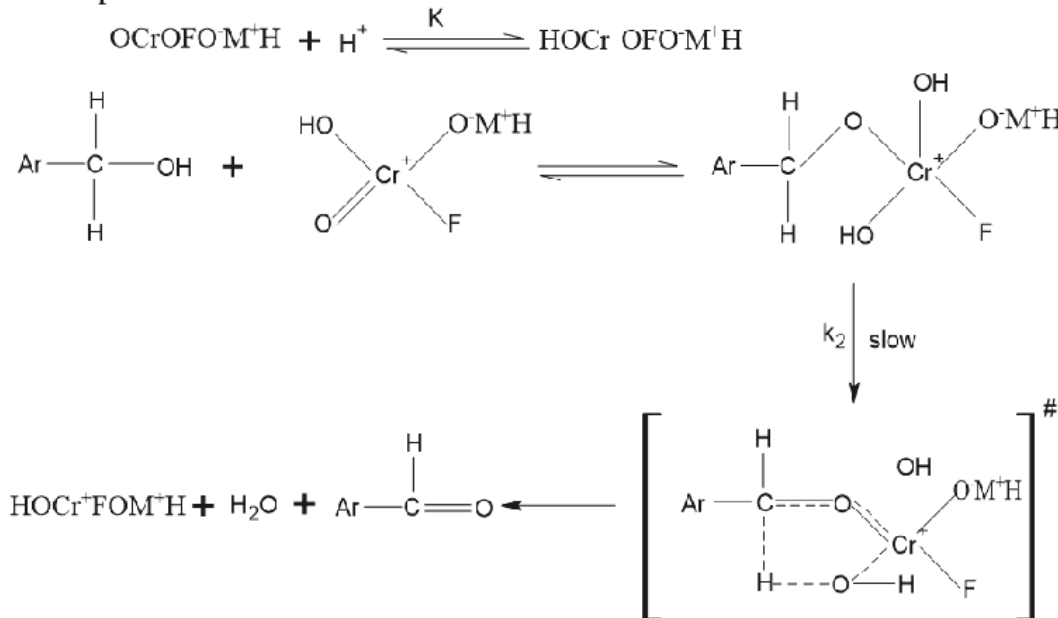
A hydrogen extraction mechanism leading to the formation of the free radicals is not likely in sight of the failure to stimulate polymerization of acrylonitrile and no effect of the radical scavenger on the reaction rate. The existence of substantial kinetic isotope effect

confirms the cleavage of  $\alpha$ -C-H bond in the step of rate-determination. The negative value of localization and delocalization electrical effects that is of L, D and R clearly indicates are action centre which is electron deficient in the step of rate-determination. The positive value of  $\eta$  is further supported it, which indicates that the substituents are stabilizing the cationic or electron-deficient reactive site. On the above basis, a mechanism is proposed in which a transfer of hydride-ion is suggested in the rate-determination step. Kwart and Nickle [22-24] have shown that dependence of kinetic

#### Acid-independent Path - Scheme - 1



#### Acid-dependent Path - Scheme - 2



isotopic effects on the temperature has been shown to be useful in determining whether hydrogen loss occurs by concerted cycle process or by an acyclic one. Alcoholoxidation by Cr (VI), involves 6 electrons and, being a Huckel-type system, we propose that the ester intermediate can be accredited to the transition state with the planar, cyclic and symmetrical structure. As a result, the whole mechanism involves the chromate ester formation in a fast first step and then in the slow rate determining step the ester decomposition takes place via a cyclic concerted symmetrical transition state leading to the product. The proposed mechanism is also supported by observed negative value of entropy of activation. [25] (**Scheme 1 and 2**).

### Acknowledgement

Laboratory facilities and chemicals needed for the conduct of this work were provided by the department of chemistry JNVU, Jodhpur, India, and we are grateful to them.

### Conflict of Interest

There is no conflict of interest involved.

### References

- E. J. Corey and W. J. Suggs, PCC-Oxidation of primary and secondary alcohols to carbonyl compounds by PCC- An efficient reagent for the, *Tetrahedron Letters*, 16, 2647, 1975.
- F. S. Guziec and F. A. Luzio, Alcohols oxidation by using 2, 2'-BPCC, *Synthesis*, 09, 691, 1980.
- M. N. Bhattacharjee, M. K. Choudhuri, H. S. Dasgupta, N. Roy and D. T. Khathing, Use of PFC as an efficient oxidant for organic substrates, *Synthesis*, 07, 588, 1982.
- K. Balasubramanian and V.Prathiba, Oxidation of alcohols by QDC-A new reagent, *Ind. J. Chem.*, 25(B), 326, 1986.
- A.Pandurangan, V. Murugesan and M. Palanichamy, QBC: A new, efficient and selective oxidant used for the oxidation of alcohols in anhydrous acetic acid, *J. Ind. Chem. Soc.*, 72(7), 479, 1995.
- S. Z. Sayyed-Alangi, H. Sajjadi-Ghotbabadi, M. T. Baei and S. Naderi, Selective oxidation of aryl alcohols by MFC (VI) using silica gel, *Eur. J. Adv. Chem. Res.*, 8(2), 815, 2011.
- V. Purohit and P. Mishra, Kinetics and mechanism of oxidation of secondary alcohols by morpholinium fluorochromate, *Eur. Chem. Bull.*, 5(8), 324, 2016.
- V. Purohit and P. Mishra, Oxidation of substituted benzaldehydes by morpholinium fluorochromate and their structure reactivity correlation, *Int. J. Inn. Res. Rev.*, 5(4), 29, 2017.
- V. Purohit and P. Mishra, Different  $\alpha$ -hydroxy acids oxidation by morpholinium fluorochromate, *Inn. Sci. and Soc. Tech., Cibtech*, 6(1), 27, 2018.
- B. Arora, J. Ojha and P. Mishra, Oxidation of diols by morpholinium fluorochromate: A kinetic and mechanistic study, *J. Adv. Sci. Res.*, 12(1), 57, 2021.
- K. K. Banerji, Kinetic study of the oxidation of organic sulphides by pyridinium fluorochromate, *J. Chem. Soc., Perkin trans.2*, 12, 2065, 1988.
- J. F. Bunnet, G. T. Devisand H. Tanida, Elimination reactions of benzyldimethylcarbinylchloride, *J. Am. Chem. Soc.*, 84, 1606, 1962.
- D. D. Perrin, W. L. Armarego, and D. R. Perrin, Purification of Organic Compounds, *Oxford, Pergamon Press*, 1966.
- M. N. Bhattacharjee, M. K. Choudhuri and S. Purakayastha, PFC oxidation of alcohols and identification of reduced chromium species along with evidence for oxygen transfer., *Tetrahedron*, 43(22), 5389, 1987.
- H. C. Brown, C. G. Rao and S. U. Kulkarni, Oxidation of primary alcohols by pyridinium chlorochromate its stoichiometry and evidence for two electron change, *J. Org. Chem.*, 44(15), 2809, 1979.
- L. Liu and Q. X. Guo, Isokinetic relationship, iso-equilibrium relationship and enthalpy-entropy compensation, *Chem. Rev.*, 101(3), 673, 2001.
- O. Exner, On the enthalpy-entropy relationships, *Collect. Czech. Chem. Commun.*, 29(5), 1094, 1964.
- M. J. Kamlet, J. L. M. Abboud, M. H. Abraham and R. W. Taft, LSER, *J. Org. Chem.*, 48(17), 2877, 1983.
- O. Exner, Additive physical properties. I. General relationships and problems of statistical nature, *Collect. Czech. Chem. Commun.*, 31, 3222, 1966.
- C. G. Swain, M. S. Swain, A. L. Powell and S. Alumni, Solvent effects on chemical reactivity. Evaluation of anion and cation salvation powers, *J. Am. Chem. Soc.*, 105(3), 502, 1983.
- C. D. Johnson, The Hammett Equation, *Cambridge Univ. Press*, 78, 1973.
- W. A. Pevelich and R. W. Taft, The evaluation of inductive and steric effects on reactivity. The methoxide ion catalysed rates of methanol hydrolysis of I-menthyl esters in methanol, *J. Am. Chem. Soc.*, 96, 9113, 1974.
- C. G. Swain, S. H. Unger, N. R. Rosenquest and M. S. Swain, Effect of various substituent on the chemical reactivity. Improved evaluation of field and resonance components, *J. Am. Chem. Soc.*, 105(3), 492, 1983.
- M. Charton and B. Charton, Structural effects on radical reactions, Part I. Homolytic aromatic substitution, *Bull. la Soc. Chim. de France*, 199, 1988.
- M. Charton, Involvement of steric effects in the hydrolysis of amides and related compounds, *J. Org. Chem.*, 40(4), 407, 1975.
- H. Kwart and J. H. Nickel, Chromium (VI) oxidation of alcohols, *J. Am. Chem. Soc.*, 95(10), 3394, 1973.
- H. Kwart and M. C. Latimer, Kinetic deuterium isotopic criterion for concertedness, *J. Am. Chem. Soc.*, 93(15), 3770, 1971.
- H. Kwart and J. Slutsky, Structure of transition state in the thermal  $\beta$ -cis-elimination of esters, *J. Chem. Soc., Chem. Commun.*, 21, 1182, 1972.
- E. S. Gould, Mechanism & Structure in Organic Chemistry, Holt, Rinehart and Winston, New York, 1964.

# Optimization of Homomorphic Encryption Scheme for Wireless Sensor Networks using PSO Algorithm

Sangeeta Rani<sup>1</sup>, Dinesh Kumar<sup>2</sup> & Vikram Singh<sup>3</sup>

<sup>1</sup>Research Scholar, sangeetathakral24@gmail.com,

<sup>2</sup>Associate Professor

Department of Computer Science & Engineering, University College of Engineering & Technology,  
Guru Kashi University, Talwandi Sabo, Bathinda, Punjab, India.

<sup>3</sup>Professor, Department of Computer Science & Engineering, Chaudhary Devi Lal University,  
Sirsa, India, vikramsinghkuk@yahoo.com.

A wireless sensor network (WSN) is a kind of distributed design that can be accessed through dissimilar forms of security intrusions. An encoding method recognized as a homomorphic encoding (HE) is adapted to encode the entities which assist in acquiring the data from the base station. The key organization and key allocation are the major issues oftenly occurring in the HE method. These problems lead to alleviating the efficiency of the homomorphic encryption algorithm (HEA). The input must be generated in the encoding process. Thus, this study makes the utilization of particle swarm optimization (PSO) to achieve this. The PSO algorithms have the influence of nature-based meta-heuristic techniques. These techniques employ the common activities of birds and fishes as a motivation to construct a technical technique. On the basis of the supremacy of computations, the algorithmic approaches generated from the pattern of particles are exploited to modify the outcomes. As the particles move around the searching area, a pattern of arithmetical terminology is deployed to carry out the spontaneity. The permanent number key is produced to perform the encoding, using optimized PSO. The homomorphic algorithm planned on the basis of PSO is implemented on MATLAB. The results reveal that the introduced method proves is efficient for resource usage and finishing time. This approach is more adaptable with regard to completion time and resource usage in comparison with the existing approach.

**Keywords:** Wireless sensor networks, encryption, computation time, particle swarm optimization, homomorphic encryption.

## 1. Introduction

During the past decade, the advent of WSN into the networking sector has attracted the attention of both the educational and industrial sectors. In the current scenario, WSNs are continuously expanding their range and future advancements in technology will lead to more sensor applications in our daily routine as well as for a large number of different and exciting application environments. The basic transmission character of wireless communication allows broadcasts to be received by any user within the coverage area, allowing the attacker to launch various types of passive attacks (like eavesdropping, traffic analysis and surveillance, etc.) or active attacks (such as jamming, spoofing, modification, replaying and denial-of-service (DoS) attack etc.) [1]. There has been widespread research interest in protecting radio broadcasts. Classically, standard encryption schemes are applied to secure data. These schemes believe in the high complexity of the algorithm which means the

time taken by eavesdroppers to crash cryptographic systems is far greater than the legitimacy of the information, consequently, there is definite backward secrecy. Classic encryption schemes face a number of vulnerabilities. Consider for example public-key cryptography. First, it is contingent upon the computational rigour of some mathematical challenges, e.g., discrete logarithms. Due to the rapid proliferation of hardware technology, it is not possible to hold this computational security nature in the times to come. Moreover, it needs a core management set-up which must also be secured. This approach is, therefore, less desirable for most WSN and ad-hoc network applications, as the computational ability of sensor nodes is limited whereas centralized control of ad-hoc networks is absent [2].

### 1.1 Key Management in WSN

Key management is a crucial instrument for ensuring the security of network services and WSN

applications. Key management refers to a set of operations and mechanisms that support the key establishment and help maintain current keying relationships between legitimate parties in accordance with a security plan. Since WSNs have limitations on the computational power and memory capacity of sensor nodes, security schemes developed for wired and adhoc networks are inappropriate for WSNs. Key management in WSNs aims to fix the issue of generating, distributing, and maintaining those secret keys. Therefore, solutions for trustable delivery and management of these keys are important to secure WSNs [3]. Because of their significance, key management schemes for WSNs have attracted much attention from the research community and several key management schemes for WSNs have been put forward.

Based on the capacity of sensor nodes to update cryptographic keys during their operation (rekeying), these schemes generally have two categories: static and dynamic. The static key management schemes apply the principle of key pre-distribution, and the key remains fixed for the entire service span of the network. However, since a cryptographic key is adopted for a longer period of time, the chances of its attack increase considerably. The dynamic key management schemes, on the other hand, refresh cryptographic keys during the service time of the network. Dynamic key management is considered a leading key management approach in sensor networks. Dynamic key management is a group of procedures used for rekeying periodically or on-demand as per the network requirement. Dynamic key management schemes dramatically increase the network's service span and flexibility due to the revoking of compromised nodes' keys during rekeying operations [4].

### 1.1.1 Key Management Steps

The key management process consists of two steps: key generation and key distribution which are explained as follow:

i. **Key generation:** The key generation step is related to the generation of keys. Based on the type of key being deployed in the WSN, keys may be generated once or many times throughout the service span of the WSN. The real-time strategy implemented so far in this research domain has been to produce different one-time keys like session [5], network-wise, master and group-wise keys contingent upon the topology and application prerequisite of the WSN. While this contributes to a reduction in computation cost for

WSNs, it can increase storage on nodes based on the key distribution approach.

ii. **Key distribution:** The keys should be made accessible to nodes without letting other people see the keys. Conventionally, keys are shared between endpoints of communication, either directly or indirectly through reliable mediators (e.g., key distribution centres). The keys can be distributed to sensors before the network deployment or can be reallocated to nodes when requested as activated by keying episodes [6].

### 1.1.2 Key Generation Process

A key generation model for a WSN is illustrated in Fig. 1, where Alice and Bob wish to generate a secure cryptographic key and Eve, an eavesdropper present  $d$  cm away from Alice overhears all broadcasts.

Alice, Bob and Eve can find interrelated observations and respectively [7]. Alice and Bob interchange a message over the public channel, which Eve can also hear. For any and sufficiently large, IF there exist and satisfying the following key generation system comprising equation (1) to (4).

Then in equation (3) is the obtainable key rate, where is shared information and is the key's alphabet [8]. Equation (1) reflects that Alice and Bob can generate the same key with a high probability. Equation (2) denotes the message interchange via public channel without leaking information to Eve, thereby ensuring the security of the key generated. Equation (4) guarantees the uniform distribution of the key, which is required for cryptographic applications. The highest realizable key rate is regarded as key capacity and specified as:

The core generation depends on three factors, namely, temporal variation, channel reciprocity, and spatial decorrelation [9]. The motion of the transmitter, receiver or any element in the set-up is the main reason for temporal variation causing variation in the reflection, refraction and scattering of the channel paths. Channel reciprocity infers that the multipath and fading, i.e., the same carrier frequency, at both ends of the same link is the same, which provides a base to Alice and Bob for generating the same key. Spatial decorrelation indicates that any listener present at a distance greater than half-wavelength from either user undergo unrelated multipath fading, also measured by the cross-correlation between valid users and listener's signals. This feature is important to secure key generation frameworks from eavesdropping and other attacks.

## 1.2 Key Management Schemes

The major dynamic key management schemes proposed so far for WSNs have been discussed below:

### 1.2.1 EBS-based key update scheme

The Exclusion Basis System (EBS) is a combinative design of the group key management issue in wireless sensor networks. EBS-based schemes assign keys to each node out of a pool of size  $n$  (where  $n$  denotes the number of sensor nodes in the network). Rekeying is activated either occasionally or after the capturing of single or multiple nodes [10] (or suspected to be captured). During the rekeying operation, replacement keys are generated, encrypted with all the keys unknown to the captured nodes and finally distributed to other nodes that collectively know the keys. A popular distributed key management scheme based on EBS is Scalable, Hierarchical, Efficient, Location-aware and Lightweight (SHELL). In SHELL, sensor nodes are congregated into clusters where  $n$  indicates the number of nodes in a cluster) and rekeying takes place inside these clusters. The network considered in SHELL includes a command node, cluster heads (CHs), gateways and sensor nodes. The command node is assumed to have plenty of resources and is not compromising. In SHELL, the gateway determines the number of administrative keys required for the cluster post bootstrapping. Subsequently, it sends a node list as well as the EBS table of key groupings to the command node. The command node specifies multiple gateways for each cluster to produce administrative keys. Post generation, the key generation gateways encrypt and propagates these keys to the cluster head, which then decrypts these messages and sends their contents to the fellow nodes of its cluster.

### 1.2.2 Polynomial secret-sharing-based rekeying scheme

Polynomial secret-sharing-based rekeying scheme (PCGR) is a pre-distribution and local collaboration-based group rekeying that deals with the issue of compromised nodes. PCGR schemes randomly assign sensor nodes to many groups and nodes in a group hold a unique key [11]. The two most popular PCGR schemes are Basic PCGR (B-PCGR) and Cascading PCGR (C-PCGR). B-PCGR scheme needs single-hop neighbours to cooperatively conserve the key polynomials of their group. However, if a node and a specific threshold number of its single-hop neighbours (denotes a parameter selected by  $t$ ) are compromised, the group key polynomial appears. C-PCGR, in

which a node's shares are allotted among its multi-hop neighbours came into existence to tackle the above limitation of B-PCGR and is more flexible against node compromise. In C-PCGR, the e-polynomial shares of a sensor node are dispersed to its multi-hop neighbours, meanwhile, the e-polynomial shares are distributed/collected in a comprehensive manner. PCGR can successfully identify fake shares induced by an opponent using a polynomial-based signature and authentication.

### 1.2.3 Deterministic sequence-number-based scheme

Energy-efficient distributed deterministic key management scheme (EDDK) is a prominent deterministic sequence-number-based approach to safely generate and maintain the pairwise keys and the local cluster key. It assumes that every node  $A$ , prior to placement, is filled with a network-wide pseudorandom function and a network-wide initial key. In addition, node  $A$  has a local cluster key exchanged with all its neighbours [12]. The initial key is employed to calculate the node's individual key, from which a discrete encryption key and a Message Authentication Code (MAC key) are obtained. In EDDK, each node requires to save the keys pairwise and local cluster keys as well as to have its own public and private keys. Moreover, this is also essential for each node to store a neighbour table to preserve keys (including pairwise keys and local cluster keys) and sequence numbers. The EDDK has three phases: key installation, data transfer, and key maintenance. There are three stages in EDDK scheme: key establishment, data transfer, and key maintenance. The final phase involves key update, compromised key cancellation, novel node joining and mobile node joining. In EDDK, the presence of the node's ID and sequence number fields in the neighbouring table fails the replay attacks on the receiver node. Sybil attacks and node replication attacks will also fail as the attacker does not have all the information (sequence numbers and pairing keys) needed to authenticate messages. Nevertheless, since a sensor node must generate pairwise keys with all its neighbours and maintain a neighbour table, EDDK can't be applied to dense networks where each sensor node has multiple neighbours.

## 2. Literature Review

The review of research literature reviewed for the present endeavour has been trifurcated into three subsections, namely, key generation techniques for



security, key management techniques for security, and key distribution techniques for security.

## 2.1 Key generation techniques for the security in WSN

Kemedi Moara-Nkwe, et al. (2018) suggested a new Physical Layer Secure Key Generation (PL-SKG) technique and its deployment was done on real nodes which assisted two parties in generating and refreshing the pair-wise keys [12]. A new technique of generating keys was put forward in which the power and simplicity of traditional error-correcting codes and also the diversity of frequency channels present on 802.15.4 compliant nodes were included for generating the keys from received signal strength (RSS) readings. The suggested had provided a higher key agreement and the key, whose generation was done using it, was able to de-correlate with distance in a fast manner. The key reconciliation rate obtained from the suggested technique was calculated 100% and it offered forward and backward security effectively.

Jaruwan Mesit, et al. (2018) introduced a lightweight and secure technique to perform the node-to-node key agreement in unsecured WSNs [13]. This technique was planned on the basis of symmetric cryptography protocol. A communication number was obtained from the registration server in the principal nodes for communicating with the key server. Thereafter, the key server was utilized for generating a session key which allowed the principal nodes to establish secure communication among one another.

Two principal nodes became capable of acquiring the session key which provided less computation and security using cryptography techniques and exchanging the message with the trusted agents. Various components were considered for analysing the introduced technique. The results demonstrated that the introduced technique kept the network secure, authentic, integrated and confidential.

Vipin Kumar, et al. (2021) developed a dynamic key management method for the clustered sensor network which assisted in inserting a novel node in the network later on in WSN [14]. A cluster head was utilized to generate the key in a dynamic way and distribute it in a secure way to communication parties. Several attacks such as replay attacks and node capture attacks were launched to compute the resistance of the developed method. The energy consumed while generating and refreshing the keys was considered in the simulation. The results obtained in analysing the security indicated that the developed method was resilient against the node capture attack.

Ravi Babu Gudivada, et al. (2018) projected a secure communication method recognised as KeyGenSC based on generating a key for mitigating the frequency of key renewals and a Symmetric Key-based Diffie-Hellman (SKDH) method was implemented for diminishing the energy utilized while renewing the key [15]. Cooja simulator was utilized to stimulate the projected method. The simulation outcomes exhibited that the projected method assisted in mitigating the energy usage in comparison with the standard technique.

Table 1 – Key generation techniques for the security in WSN

Author	Year	Technique Used	Findings	Limitations
Kemedi Moara-Nkwe, et al.	2018	Physical layer secure key generation (PL-SKG) scheme	The key reconciliation rate obtained from the suggested technique was calculated 100% and it offered forward and backward security effectively.	This technique was not able to generate and refresh the key in full key recovery protocols.
Jaruwan Mesit, et al.	2018	A lightweight and secure technique	The results demonstrated that the introduced technique kept the network secure, authentic, integrated and confidential.	The issue related to the centralized servers was found in the introduced technique.
Vipin Kumar, et al.	2021	A dynamic key management method	The results obtained in analyzing the security indicated that the developed method was resilient against the node capture attack.	The developed method was not applicable in all kind of networks.
Ravi Babu Gudivada, et al.	2018	KeyGenSC	The simulation outcomes exhibited that the projected method assisted in mitigating the energy usage in comparison with the standard technique.	The attacks were not eliminated using this method.
Harshit Kr. Agarwal, et al.	2019	Optimized Light Weight Secure Clustering protocol (OLWS)	The outcomes depicted the applicability of the established technique to deal with the energy consumption issues and enhance security level.	The established technique had deployed 160-bit hash value for authentication which was considered as the higher value.



Harshit Kr. Agarwal, et al. (2019) established an innovative technique known as Optimized Light Weight Secure (OLWS) clustering protocol for WSN for maximizing the security at lower overhead [16]. The identity of the node was utilized to generate and compute the key for hashing in a dynamic manner. This results in mitigating the complexity of managing the key. The established technique was implemented for detecting the attacker and recognizing the adversary node at cluster head only. NS<sub>2</sub> was employed to perform the simulations. The outcomes depicted the applicability of the established technique to mitigate energy consumption woes and enhance the security level.

## 2.2 Key management techniques for the security in WSN

Monjul Saikia, et al. (2017) designed a novel routing algorithm known as Secure Energy-Aware Multipath Routing with Key Management (SEAM-KM) in WSN [17]. A sink node was employed as the central control block for all kinds of computation such as selecting the shortest path, generating the routing table, updating the routing table and distributing the pairwise keys among the sensor nodes and sink. This algorithm was useful for maximizing the duration of sensor nodes. Hence, the designed algorithm was

adaptable to attain security among sensor nodes and also enhance the resistance of the network for dealing with some particular attacks.

Harith Fakhrey, et al. (2018) formulated a new location-dependent key management protocol for multiple sinks (LKMP-MS) planned on the basis of a cell reporters method [18]. This protocol was utilized to attain a report about any event in which 3 security levels were comprised. The base station adopted this report. Moreover, a new algorithm was established for deploying the required revocation for compromised nodes and cells so that the possible consequences that occurred due to these entities were addressed. The formulated protocol was quantified on Contiki and MATLAB. The results revealed that the formulated protocol yielded a higher security level for the network.

Sayali Tembhrune, et al. (2020) recommended a CL-EKM (Certificateless efficient key management) approach to establish communication in specific WSNs securely [19]. The key alerts and administration were executed by qualifying the communication during the joining and leaving of a node from the party. The recommended approach was efficient to deal with the cloning, and mime assaults and kept the information confidential and reliable. The analysis proved the applicability of the recommended approach in asset-

Table 2 – Key management techniques for the security in WSN

Author	Year	Technique Used	Findings	Limitations
Monjul Saikia, et al.	2017	Secure Energy-Aware Multipath Routing with Key Management (SEAM-KM)	The designed algorithm was adaptable to attain security among sensor nodes and also enhance the resistance of the network for dealing with some particular attacks.	The storage capacity of this algorithm was not enough and it had not tackled all kinds of attacks.
Harith Fakhrey, et al.	2018	Location-dependent key management protocol for multiple sinks (LKMP-MS)	The results revealed that the formulated protocol yielded a higher security level for the network.	The real-time cooperation among all base stations was not reliable and had a negative impact on the security of those cells which had fewer cell reporters.
Sayali Tembhrune, et al.	2020	Certificateless efficient key management (CL-EKM) approach	The analysis proved the applicability of the recommended approach in asset-powered WSNs and this approach was capable of protecting the network against a variety of attacks.	The recommended approach was not resilient against some specific active and passive attacks.
Abhishek Srivastava, et al.	2018	Novel shape model based on Localized Geometric Voronoi Hexagon (LGVH) algorithm	The results validated that the investigated model was efficient and secure in real-time applications in comparison with the traditional techniques concerning diverse metrics.	The investigated model was not scalable in real-time applications.
Mattia Griotti, et al.	2020	A new key management protocol	The experimental results depicted that the introduced protocol assisted in lessening the time used to establish a key up to 35%.	The performance of this protocol was decreased in the case of larger networks.

powered WSNs and this approach was capable of protecting the network against a variety of attacks.

Abhishek Srivastava, et al. (2018) investigated a new shape model on the basis of the Localized Geometric Voronoi Hexagon (LGVH) algorithm and the secure communication was established with the help of key management techniques [20]. The consecutive process, of establishing, updating and revoking the key, resisted the network against the insider attackers. The information related to the location of sensor nodes was obtained from the investigated model for predicting the coverage area for the dynamic environment. The customizable WSN simulator tool was extended on the basis of NS<sub>2</sub> simulator to provide a comprehensive coverage area. The results validated that the investigated model was efficient and secure in real-time applications in comparison with the traditional techniques concerning diverse metrics.

Mattia Griotti, et al. (2020) introduced a novel key management protocol [21]. The nodes were authenticated while establishing the key using a transitory symmetric key. Asymmetric cryptography was employed to establish the pair-wise keys. The introduced protocol was effective to diminish the computational effort of the public key cryptosystem and maximizing the security of the network in contrast to the existing techniques. The experimental

results depicted that the introduced protocol assisted in lessening the time used to establish a key up to 35%.

### 2.3 Key distribution techniques for the security in WSN

Iman Gholizdeh, et al. (2019) suggested an Efficient Key Distribution Mechanism (EKDM) whose extraction was done from the symmetric polynomial technique [22]. The analysis outcomes demonstrated that the suggested mechanism had robustness for dealing with the compromise attack in comparison with the other techniques. A more effective technique was utilized by CHs (cluster heads) for mitigating the amount of overhead. In addition, the suggested mechanism was useful for inserting the node and refreshing the key. Hence, this mechanism was highly flexible for determining the suitable security level and mitigating energy usage woes.

K. Naveen Kumar, et al. (2017) presented a framework for mitigating the threats that occurred because of the physical attacks [23]. A secure and effectual Chip-based Symmetric and Asymmetric Key Distribution (CSAKD) method was incorporated in this framework on the basis of additional commodity hardware Trusted Platform Module (TPM). The results confirmed that the presented framework had

Table 3 – Key distribution techniques for the security in WSN

Author	Year	Technique Used	Findings	Limitations
Iman Gholizdeh, et al.	2019	Efficient Key Distribution Mechanism (EKDM)	The suggested mechanism was useful for inserting the node and refreshing the key.	The memory utilization was found slightly higher in contrast to other protocols
K. Naveen Kumar, et al.	2017	Chip-based symmetric and asymmetric key distribution (CSAKD) technique	The presented framework had the potential for meeting the demands of security in WSNs due to which the network became confidential, integrated, authentic, secure and resilient against attacks.	This technique had not performed well on large scale networks.
K. Naveen Kumar, et al.	2017	Secure, less intensive and effective asymmetric key distribution (AKD) method	The established mechanism had provided resistance against physical attacks, key connectivity and refreshed the data.	This mechanism required additional economical costs for the hardware.
Priyanka Ahlawat, et al.	2018	An efficient adversarial model	The outcomes revealed the resiliency of the intended system for tackling node capture attacks and this system was efficient to maximize the security of WSN.	The neighbour influence factor was not computed for dissimilar kinds of cells in this system.
Selva Reegan A., et al.	2017	Polynomial and Multivariate Mapping-Based Triple-Key (PMMTK) distribution technique	The designed technique provided security, higher duration of the network, superior PDR (packet delivery ratio), least delay and the average number of key establishment.	This technique was unable to provide complete security in some scenarios.

the potential for meeting the demands of security in WSNs due to which the network became confidential, integrated, secure, authentic and resilient against attacks.

K. Naveen Kumar, et al. (2017) established a mechanism with the objective of mitigating the attacks [24]. A novel secure, less intensive and effective Asymmetric Key Distribution (AKD) method was implemented on the basis of the additional commodity hardware Trusted Platform Module (TPM). The genuine and malicious nodes as well as the tamper-resistant ability of a node were recognized using the established mechanism. The established mechanism had provided resistance against physical attacks, key connectivity and refreshed the data.

Priyanka Ahlawat, et al. (2018) intended an effective adversarial system for the cellular model of WSN in order to mitigate the effect of the node capture attack [25]. This system was constructed on the basis of BS (base station) in a cell and neighbour influence factor. The estimated compromise probability of every cell was deployed to evaluate the stage of pre-distributing the hash chain key. This led to locating the key pool of cells having susceptibility to attacks at the end of the hash chain. Moreover, the intended system assisted in diminishing their keying overhead. The outcomes revealed the resiliency of the intended system for tackling the node capture attacks and this system was efficient to maximize the security of WSN.

Selva Reegan A., et al. (2017) designed Polynomial and Multivariate Mapping-Based Triple-Key (PMMTK) distribution technique to compute the individual key of the nodes and common triple-key [26]. This technique was focused on maintaining the security of the data packet for which communication was established among the nodes. A triple-key was generated by computing the key combinations at an individual level. The designed technique provided security, higher duration of the network, superior packet delivery ratio, least delay and the average number of key establishment.

### 3. PSO-based Homomorphic Encryption Scheme for WSN

There are various encoding techniques available to ensure the security of WSN. To achieve this, a completely Homomorphic technique is effective and reliable. Unlike Full Disk Encryption (FDE), this technique offers higher privacy and protection. This technique has faced diverse issues such as storing the

key, organizing the key, controlling the admission and maintaining the information. Over the last few decades, a number of schemes are suggested to deal with these issues related to organizing the key and allocating the key. These methods have susceptibility against these intrusions. The third-party investigation system may be faced failure when the third party is compromised and a malicious state has occurred. Thus, the user focuses on developing an effective system with the objective of allocating and organizing the key. An efficient key organizing system can be generated using the PSO-based homomorphic encoding technique. Particle swarm optimization algorithms are developed under influence of nature. These algorithms make the deployment of common activities of birds and fishes as a basis of constructing a technical method. The supremacy of computations is considered for the modification of outcomes using the algorithmic approaches that are developed from the pattern of particles. As the particles move in the searching region, a pattern of arithmetical terminology is exploited to perform spontaneity. For the swarm, the moves of each particle are suggested to the effective locality. It is also determined whether the arbitrary apprehensions are present or not. Some variants, in which various up-gradation policies are deployed, are lacking.

In this, the aiming operation of the particle swarm optimization algorithm is discussed efficiently. To achieve this, the present iteration is compared with the traditional one with regard to the swarm value. The aiming operation is recognized considering the swarm value having the greatest iteration. Equation 3 is expressed to define the vibrant aiming function. The variation in its value is found subsequent to every iteration as:

$V_i$  in equation (6) denotes the speed of elements, the is the maximum value amid the existing choices and the *rand* illustrates the random value.  $x$  value is utilized to implement each attribute available on a website.  $c$  value is used to define the entire characteristics of the website.  $p$  represents the best value whose recognition is done from every particle and  $g$  depicts an optimal value whose recognition is done from every iteration. After the finalization of the target function and quality compromise, the acquired value is inserted in the equation as:

In equation (7),  $p$  denotes the position vector. PSO is adopted as it can remove the multi aiming optimization issues. The PSO algorithms consist of some vibrant aiming functions. These functions assist in improving the efficiency of the system with regard to the finest

computed value. The PSO algorithm deploys the input data to perform the encoding process and generates an advanced value that can be employed to accomplish the encoding.

### 3.1 Proposed Encryption Scheme

Input: Original plain message ( $M$ )

Output: Intermediate cypher message ( $C$ ) and final encrypted message ( $C'$ )

#### I. Key Generation Logic:

1. Input  $M$
2. Invoke the PSO with  $M$  as the initial swarm population for the calculation of the first local and global best positions ( $pBest$  and  $gBest$ )
3. Update the position and velocity of the swarm and iterate step 2 with updated swarm parameters until the best position and velocity of the swarm is obtained by using the formulae:
  - (i)  $v = v + c_1 * rand * (pBest - p) + c_2 * rand * (gBest - p)$
  - (ii)  $p = p + v$
 where  $p$  is the particle position,  $v$  is the particle velocity,  $c_1$  and  $c_2$  are weight constants that determine the values of  $pBest$  and  $gBest$ , respectively.

#### II. Encryption Logic:

Use  $p$  as the encryption key in the encryption function.

$Enc(M, p) \rightarrow C$  where  $M$ ,  $C$ , and  $p$  are plain message, intermediate cypher message, and encryption key respectively in the encryption function  $Enc$ .

#### III. Evaluation Logic:

Here an evaluation function  $Eval$  is applied to  $C$ :  $Eval(F, C) \rightarrow C'$  where  $F$  and  $C'$  are arithmetic/ Boolean circuit and the final cipher text, respectively.

#### IV. Decryption Logic:

A decryption function  $Decr$  translates the cypher message  $C'$  to yield the plain message  $M$  and takes  $C'$  and the secret key  $p$  as its input:  $Decr(C', p) \rightarrow M$ .

## 4. Result and Discussion

In the present research, the experimentation part has been performed using MATLAB. Images have been used as input to the encryption scheme. The information has been encoded and decoded using the balanced encoding algorithm, whereas a PSO-based optimized homomorphic encryption scheme was implemented to produce an advanced key. This key is helpful to perform the encoding of information with the help of a homomorphic system. The introduced

method is quantified on the basis of two metrics namely execution time and resource usage. Xnon operating system was deployed on each basic system. 5GB RAM is included in every fundamental system and a total of seven fundamental machines were simulated. Overall eighty 256x256 images have been encrypted using three encryption schemes, namely, homomorphic encryption scheme (HES), enhanced homomorphic encryption scheme (EHES), and optimized homomorphic encryption scheme (the proposed scheme), to compare their relative performance, shown in fig. 2 and fig. 3..

Fig. 2. Encryption time (sec)

Fig. 2 illustrates the comparison of the introduced approach with the traditional approach with regard to the execution time. The traditional approach is a kind of homomorphic encoding, on the other hand, the projected algorithm is an enhancement of the homomorphic encoding system.

Fig. 3 represents that the existing system is compared with the introduced order to determine the resource usage. The investigation reveals that the introduced system provides lower resource exploitation.

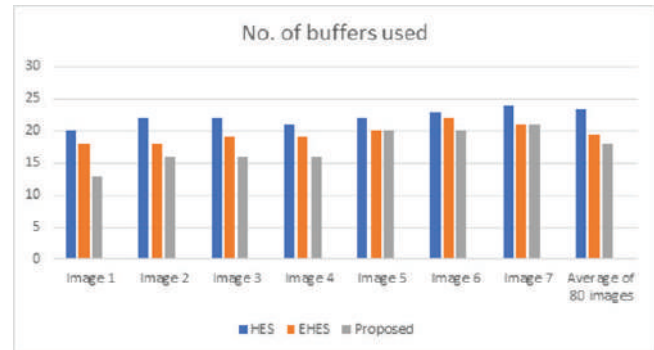


Fig. 3 – Resource usage (no. of buffers used)

## 5. Conclusion

The homomorphic encoding system is utilized to encode the WSN information. The major concerns related to this system are to allocate the key and organize the key. The key is produced to carry out the encoding using PSO, an enhanced algorithm. This key is deployed for input in the homomorphic encoding algorithm in order to create the encoded data. The projected system is implemented on MATLAB. The resource employment and execution time are considered for analyzing the outcomes. This exhibits that the projected algorithm provides lower resource usage and execution time in contrast to the existing algorithm. The future work would emphasize



improving this system to ensure that the information is reliable in WSN surroundings.

## References

- 1 K. Moara-Nkwe, Q. Shi, G. M. Lee and M. H. Eiza, "A Novel Physical Layer Secure Key Generation and Refreshment Scheme for Wireless Sensor Networks," in *IEEE Access*, vol. 6, pp. 11374-11387.
- 2 L. Li, Z. Yafei, D. Xiaoyi and S. Guozhen, "Research on secure communication scheme of clustered WSN based on dynamic key," 2016 *IEEE Information Technology, Networking, Electronic and Automation Control Conference*, 2016, pp. 833-837.
- 3 M. F. Moghadam, M. Nikooghadam, M. A. B. A. Jabban, M. Alishahi, L. Mortazavi and A. Mohajerzadeh, "An Efficient Authentication and Key Agreement Scheme Based on ECDH for Wireless Sensor Network," in *IEEE Access*, vol. 8, pp. 73182-73192, 2020.
- 4 S. S. Abd El Dayem, M. R. M. Rizk and M. A. Mokhtar, "An efficient authentication protocol and key establishment in dynamic WSN," 2016 6th *International Conference on Information Communication and Management (ICICM)*, 2016, pp. 178-182.
- 5 F. Gandino, B. Montrucchio, and M. Rebaudengo, "Key Management for Static Wireless Sensor Networks with Node Adding", 2014 *IEEE Transactions on Industrial Informatics*, vol. 10, no. 2.
- 6 M. A. Mughal, P. Shi, A. Ullah, K. Mahmood, M. Abid and X. Luo, "Logical Tree Based Secure Rekeying Management for Smart Devices Groups in IoT Enabled WSN," in *IEEE Access*, vol. 7, pp. 76699-76711, 2019.
- 7 T. T. Chakavarika, B. K. Chaurasia and S. K. Gupta, "Improved energy efficient key management scheme in wireless sensor networks," 2016 *International Conference on Communication and Signal Processing (ICCSP)*, 2016, pp. 2135-2140.
- 8 P. Porambage, P. Kumar, C. Schmitt, A. Gurtov and M. Ylianttila, "Certificate-Based Pairwise Key Establishment Protocol for Wireless Sensor Networks," 2013 *IEEE 16th International Conference on Computational Science and Engineering*, 2013, pp. 667-674.
- 9 P. Jilna, P. P. Deepthi and U. K. Jayaraj, "Optimized hardware design and implementation of EC based key management scheme for WSN," 2015 10th *International Conference for Internet Technology and Secured Transactions (ICITST)*, 2015, pp. 164-169.
- 10 C. Xiong, S. Li, L. Liu and R. Li, "Key Pre-Distribution Scheme for WSN Based on Hash Function," 2018 15th *International Computer Conference on Wavelet Active Media Technology and Information Processing (ICCWAMTIP)*, 2018, pp. 241-246.
- 11 S. Roy and M. J. Nene, "A key management scheme for Wireless Sensor Network using received signal strength indicator," 2016 *Online International Conference on Green Engineering and Technologies (IC-GET)*, 2016, pp. 1-7.
- 12 Kemedi Moara-Nkwe, Qi Shi, Gyu Myoung Lee, Mahmoud Hashem Eiza, "A Novel Physical Layer Secure Key Generation and Refreshment Scheme for Wireless Sensor Networks", 2018, *IEEE Access*.
- 13 Jaruwat Mesit, Matthias R. Brust, Pascal Bouvry, "Lightweight Key Agreement for Wireless Sensor Networks", 2018, *IEEE International Conference on Software Quality, Reliability and Security Companion (QRS-C)*.
- 14 Vipin Kumar, Navneet Malik, "Dynamic Key Management Scheme for Clustered Sensor Networks with Node Addition Support", 2021, 2nd *International Conference on Intelligent Engineering and Management (ICIEM)*.
- 15 Ravi Babu Gudivada, R. C. Hansdah, "Energy Efficient Secure Communication in Wireless Sensor Networks", 2018, *IEEE 32nd International Conference on Advanced Information Networking and Applications (AINA)*.
- 16 Harshit Kr. Agarwal, Meenakshi Tripathi, "OLWS: Optimized Light Weight Secure Clustering protocol for Wireless Sensor Networks", 2019, 4th *International Conference on Information Systems and Computer Networks (ISCON)*.
- 17 Monjul Saikia, Uddipta Kaishyap Das, Md. Anwar Hussain, "Secure energy aware multi-path routing with key management in wireless sensor network", 2017, 4th *International Conference on Signal Processing and Integrated Networks (SPIN)*.
- 18 Harith Fakhrey, Martin Johnston, Federico Angelini, Rajesh Tiwari, "The Optimum Design of Location-Dependent Key Management Protocol for a Multiple Sink WSN Using a Random Selected Cell Reporter", 2018, *IEEE Sensors Journal*.
- 19 Sayali Tembhurne, Rajesh Babu, "Implementation of Key Management Strategy to Reduce Attackers Impact on Data Aggregation", 2020, 5th *International Conference on Communication and Electronics Systems (ICCES)*.
- 20 Abhishek Srivastava, Sudhanshu Tripathi, Shweta Dwivedi, Prinu C. Philip, "Shape-Area Model-based Key Management in Wireless Sensor Network", 2018, *Recent Advances on Engineering, Technology and Computational Sciences (RAETCS)*.
- 21 Mattia Griotti, Filippo Gandino, Maurizio Rebaudengo, "Transitory Master Key Transport Layer Security for WSNs", 2020, *IEEE Access*.
- 22 Iman Gholizadeh, Esmail Amiri, Reza Javidan, "An Efficient Key Distribution Mechanism for Large Scale Hierarchical Wireless Sensor Networks", 2019, 27th *Iranian Conference on Electrical Engineering (ICEE)*.
- 23 K. Naveen Kumar, Manisha J. Nene, "Chip-Based symmetric and asymmetric key generation in hierarchical wireless sensors networks", 2017, *International Conference on Inventive Systems and Control (ICISC)*.
- 24 [K. Naveen Kumar, Manisha J. Nene, "Chip-based asymmetric key generation in hierarchical wireless sensors networks", 2017, 2nd *International Conference for Convergence in Technology (I2CT)*.
- 25 Priyanka Ahlawat, Mayank Dave, "An attack model based highly secure key management scheme for wireless sensor networks", 2018, *Procedia Computer Science*.
- 26 Selva Reegan A., Baburaj E., "Polynomial and multivariate mapping-based triple-key approach for secure key distribution in wireless sensor networks", 2017, *Computers & Electrical Engineering*.

## Sesimic Damage Estimation of Unidirectional Setback type of 3D Irregular Buildings

Hemil M. Chauhan\*<sup>1</sup> and Kaushal B. Parikh<sup>2</sup>

<sup>1</sup>Gujarat Technological University, Ahmedabad, Gujarat, India

<sup>2</sup>Applied Mechanics Department, G.E.C. Dahod, Gujarat, India

In this study, a new methodology is proposed to estimate the seismic damage in terms of absorbed energy and degrading stiffness on vertical irregular buildings using pushover analysis. For damage evaluation, parametric study such as change in heights, plan dimensions, and different types of monotonic loads are used. Pushover curve does not indicate any damage state at any point of the curve, so suggested two methods have provided acceptable and accurate findings for assessing the damages at any point of the pushover curve. On different performance points on pushover curves, two damage indices are validated with existing deformation and strength based damage indices. The results of each case's drift are well within the permitted limits of the existing standards. The results of damage index indicated that new approaches for calculating damage to irregular buildings are easy to use and reliable after performing pushover analysis.

**Keywords:** pushover analysis, energy based damage index, stiffness based damage index, vertical irregular building

### Introduction

Seismic engineering has evolved significantly during the past two decades, as a consequence of the worldwide earthquake resistant design is adopted. According to existing data, irregularities in building configuration cause severe damage against seismic loads [1]. Damage indices were proposed to estimate seismic damage to RC structures or its elements. Seismic damage estimation is needed for achieving the appropriate degree of performance of the building. The most common cause of structural damage is loss of strength, stiffness, or ductility [2]. Engineers may allow for some structural damage in an earthquake disaster, thus nonlinear analysis affects structural design. Few researchers have developed a damage estimation index at different performance levels. Seismic damage indices can be derived using energy, stiffness, strength, ductility, and deformation, among other parameters [3]. M. Zameeruddin [4] had developed several damage indices for RC buildings, including energy, stiffness, strength, and ductility-based EDPs (Engineering demand parameters), Habibi A. [1] had developed damage index based on drift, Cinitha A. [5] had developed softening damage index based on time period and elastic-plastic damage index based on spectrum displacement and acceleration.

A. Vimala [6] and Pritam H. [3] has been suggested ductility, dissipated energy, and stiffness based damage indices. Earlier studies employing pushover analysis and damage indices used 2D frames, which cannot accurately estimate torsion in a building [7]. 3D modelling and analysis of the building may provide accurate nonlinear results. A few studies had assessed the seismic performance of irregular buildings and found inadequacies in the seismic code. The structure's vertical irregularity demands considerable stiffness to control torsional deformation. Vertical irregularities in a building cause vertical load distribution discontinuities and significant amount of torsion effect [7-8]. It was proven that pushover analysis can accurately determine failure mode and create base shear versus displacement curves under monotonic loads [9].

The main objective of this study is to estimate seismic damage for realistic 3D vertical irregular reinforced concrete (RC) buildings utilizing performance-based seismic design approach that includes advanced analytical tools. The limitations of the previous research is addressed and by proposing damage indices that allow for pushover analyses for assessing the cumulative effects of deterioration of stiffness and energy dissipated after each incremental displacement. Two distinct damage indices are obtained by applying pushover analysis techniques to the setback types of vertical irregular buildings on

\*Corresponding author.  
Email: hemilcivil@gmail.com



various performance levels on the pushover curve. In this work, nonlinear static analysis is conducted, one damage index (DI) is based on absorbed energy and the other is based on stiffness degradation.

**Seismic damage index**

Damages to irregular RC buildings are primarily concerned with element failure, which resulted into significant deformation and concrete becoming nonlinear [10-11]. The calculation of damage index of irregular buildings is highly important due to any unexpected response of the building against lateral loads. The key criteria include strength, stiffness, ductility, lateral displacement (drift), torsion, and other EDPs that are used to characterize the failure process [12]. Several researchers had worked on damage assessment, including Ghobarah A. [13], had worked on stiffness-based damage estimation but had not included torsion effects in their study. However, the cumulative effect of cyclic loading has been introduced using nonlinear dynamic analysis, which was based on plastic deformation and dissipated hysteretic energy [9]. Researchers Roufaiel and Meyer [14] had worked on DI based on displacement, but the cumulative effects of hysteresis cycles was not taken into account in their proposed calculation, it is difficult to ascertain seismic damage precisely. A. Mwafy [15] had worked, comparative study using nonlinear dynamic and static approach on 2D regular and irregular frames. S. Jeong [16] had taken into account torsional and geometrical plan irregularities, however the applicability in high-rise buildings was not fully clarified. Damage estimations based on stiffness, ductility and dissipated energy were investigated by S. Diaz [17] for hysteretic cycles, and however torsion and bidirectional moment effects were not included in the study. M. Zameeruddin [18] has proposed new empirical method for estimating stiffness-based damage index that took into account the cumulative effect of degrading stiffness while employing nonlinear static analysis in regular frames and ignored torsion effects. While the performance evaluation of building load pattern selection is expected to be more important than the actual determination of target displacement [19-20].

Modified stiffness based damage index and energy based damage index are developed and implemented in this study on a wide range of irregular 3D buildings where substantial torsion is created due to vertical irregularities. In pushover analysis incremental lateral displacement is applied until the target displacement is

not reached of particular joint. Each incremental step causes the building's stiffness to deteriorate, as well as the increase amount of inelastic energy absorbed by the structure. Although pushover analysis is an efficient approach that produces a good appropriate

Table 1 – Summary of Damage Indices

DIs	Details of DIs	Proposed formula
A) Local DI		
P. Rajeev, K. (2014) Wijesundara [22]	Based on the amount of energy dissipated on concentrically braced steel frame.	$DI = \frac{E_{Diss.energy}}{E_{Capacity energy}}$
Park and Ang (1985) [23]	Based on linear combination of maximum plastic displacement and dissipated energy.	$DI = \frac{d_m}{d_u} + \beta_e \frac{\int dE}{F_y d_u}$
Powell & Allahabadi (1988) [12]	Based on plastic deformations and ductility	$DI = \frac{U_{max} - U_y}{U_{mon} - U_y}$
Julian Carrillo, (2015) [24]	Based on degradation stiffness of the member	$DI = 1 - \frac{K}{K_0}$
B) Global DI		
Roufaiel and Mayer (1987) [14]	Deformation based DI	$DI = \frac{d_m - d_y}{d_u - d_y}$
Di Pasquale & Cakmak (1990) [25]	1) Max. softening DI	$DI = 1 - \frac{T_{initial}}{T_{final}}$
	2) Plastic based	$DI = 1 - \left[ \frac{T_{initial}}{T_{final}} \right]^2$
	3) Final softening	$DI = 1 - \left[ \frac{T_{final}}{T_{maxi}} \right]^2$
Ghobarah A. et al (1999) [13]	Based on stiffness of the structure before and after an earthquake	$DI = 1 - \frac{K_{final}}{K_{initial}}$
A. Cinitha et al (2015) [5]	1) Strain hardening	$DI = \frac{\sqrt{S_d} - \sqrt{S_{do}}}{\sqrt{S_a} - \sqrt{S_{ao}}}$ $\frac{\sqrt{S_{du}} - \sqrt{S_{do}}}{\sqrt{S_{au}} - \sqrt{S_{ao}}}$
	2) Perfectly elasto-plastic curve	$DI = \frac{\sqrt{S_d} - \sqrt{S_{do}}}{\sqrt{S_{du}} - \sqrt{S_{do}}}$

result for creating a pushover curve, however it does not provide any structural damage identification. A damage occurrence including distinct variants of these EDPs is referred to as a damage index. Several investigations were done, as indicated in table 1 to compute the damage index.

The new DI assessment has number of advantages, which are listed below. (i) The DI is suitable to estimate including variation of stiffness of structure and absorbed energy related with first hysteretic cycle (ii) it is simple and requires minimum computations time (iii) it excludes nonlinear dynamic time history analysis, which is complex, time-consuming, and requires large amount of ground motion data. Proposed DI methods are describe below.

**Energy based damage index (EBDI)**

Nonlinear analysis has input energy in the form of seismic loads and output energy that resists the earthquake load as shown in equation (1) [21]. The inelastic energy in equation (1) is represented the

damage caused by persistent plastic rotations in beams and columns. The entire energy absorbed by the structure is determined using nonlinear static analysis at many critical locations (performance levels) on the pushover curve. In equation (2), DI is the ratio of absorbed inelastic energy at intended performance level to total absorbed inelastic energy from the pushover curve.

$E_i$ (input energy) = $E_c + E_d$	(1)
------------------------------------	-----

Where,

$E_c$  (elastic strain energy) =  $E_k$  (kinetic) +  $E_s$  (strain), &  
 $E_d$  (dissipated energy) =  $E_h$  (hysteretic) +  $E_c$  (damping)

An inverted triangle as per IS 1893, mode type (parabolic curve) and acceleration types of monotonic loads are applied to generate pushover curves. The area beneath the curve represents the structure's energy absorption. This area computation technique integrates cumulative cyclic loading effects, eliminating the need for non-linear dynamic analysis. The ability of structural components to dissipate energy via

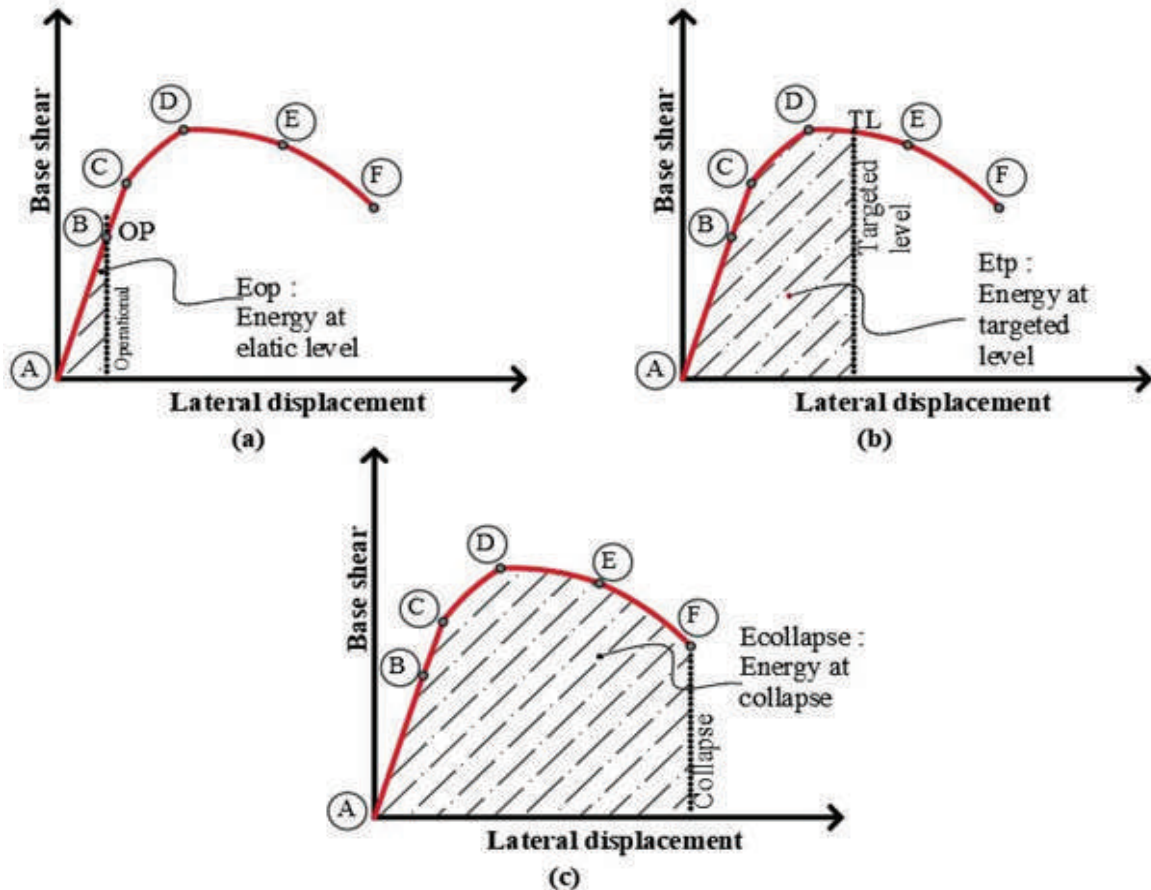


Fig. 1 (a), (b) & (c) various absorbed energy on critical points of pushover curve

hysteretic action is known as its energy absorption capacity [12]. In pushover analysis, the first hysteretic cycle was established by computing the area under the pushover curve using monotonic loading, in which a maximum amount of various energies were absorbed through lateral load. Performance level at operational is defined as the area under the pushover curve up to the first yielding point (Figure 1a). Energy absorption by a structure up to a specific performance point is called energy at targeted performance point.

$\text{Damage index } (D_{i_{\text{Energy}}}) = \frac{E_{t.p} - E_{op.}}{E_{co.} - E_{op.}} \quad (2)$
--

$\text{Energy @ t.p} = \int_0^{S_d(t.p)} (ax^n + bx^{n-1} + C) dx \quad (3)$
--

Where,

$E(t.p)$  targeted point = energy at targeted performance level

$E_{op.}$  = energy at operational level, &

$E_{co.}$  = energy at collapse level

Figure 1c is depicted the structure's total nonlinear energy capacity ( $E_{collapse}$ ). (Until the curve collapses.) Figure 2 is shown its polynomial equation for calculations energies at different levels of the curve. On the pushover curve, equation (2) computes energy-based damage index, whereas equation (3) computes absorbed energy at different point on curve.

**Stiffness based damage index (SBDI)**

The structure's stiffness decreases with each step when performing pushover analysis, and it depends on several variables. Powell & Allahabadi (1988) [12] had been performed the nonlinear dynamic analysis and proposed stiffness-based damage index. In 1999, Ghobarah et al [13] had been proposed new empirical technique based on pushover and nonlinear time history analysis. However, M. Zameeruddin [18] had been modified the approach and addressed the cumulative effects of stiffness degradation parameter using pushover analysis, and proposed empirical formula to compute stiffness based DI but it is mostly applied for regular frames. In this research, a new methodology was used to assess the cumulative effects of each incremental step in deteriorating stiffness. The stiffness based damage index is calculated using the initial slope at the pushover curve's critical points. The applied monotonic lateral load and displacement are directly and inversely proportional to the structure's stiffness respectively. Stiffness is determined by the initial slope at each performance level. It is proposed equation (4) to calculate a stiffness based damage index on the pushover curve. As illustrated in figure 3, the stiffness based damage index is computed at different performance levels of the curve.

$DI_k @ t.p = 1 - \frac{\sum V}{\sum K * d} \quad (4)$
--

Where,  $DI_k$ , targeted point = stiffness based damage index at targeted level

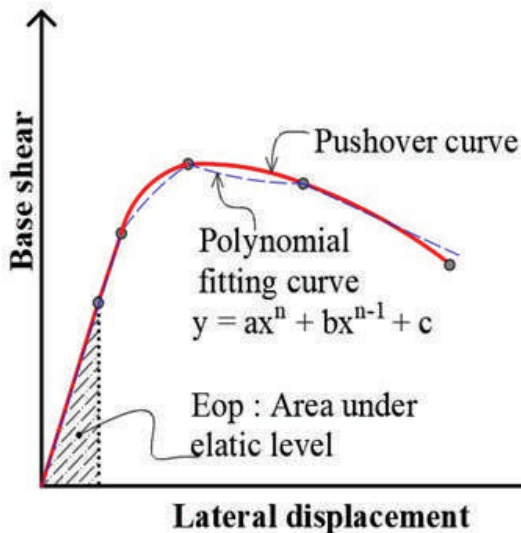


Fig. 2 – Standard pushover curve with fitting curve

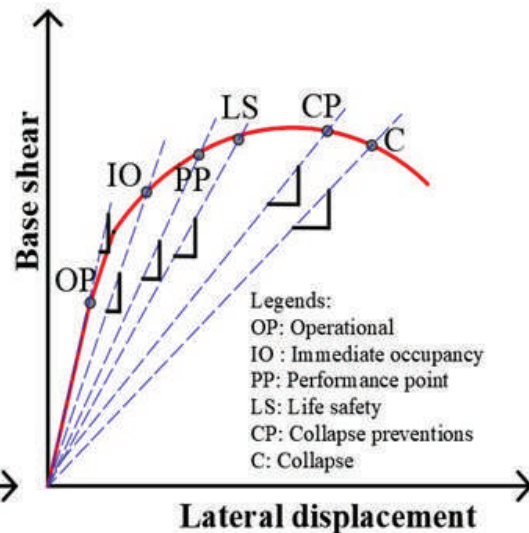


Fig. 3 – stiffness on performance level

$$\sum V = V_1 + V_2 + V_3 + \dots + V_n \text{ (summation of base shear at targeted level)}$$

$$\sum K = K_1 + K_2 + K_3 + \dots + K_n \text{ (summation of stiffness at targeted level)}$$

Where, 1, 2, 3, n are the incremental lateral steps  
 d = corresponding displacement at targeted level

**Building example**

The proposed DIs are applied on 4, 6, and 9 storey unidirectional setback type of irregular buildings. The bay dimensions are taken 5 m in each direction, and foundation and remaining floor heights are assumed 2 m and 4 m respectively. Figure 4 is shown building plans and elevations for 4, 6, and 9-storey buildings with plan aspect ratios (AR) of 0.5, 0.75, and 1.00. Three building heights indicates short, medium, and long natural time periods. There are three monotonic loadings and three plan aspect ratios of 0.5 (20m x 10m), 0.75 (20m x 15m), and 1.00 (20m x 20 m). S4 0.5 UD X indicates 4 storey with plan aspect ratio 0.5 using user defined plastic hinges and X represents horizontal direction. For 4 and 6 storey outer sizes of columns are taken 300 x 600 mm and 9 storey buildings they are considered 300 x 750 mm.

For buildings square columns and beams are assumed 600 x 600 mm and 230 x 450 mm respectively. Yield strength of reinforcement and characteristics

strength of concrete are taken 415 MPa and 25 MPa respectively. The slab load 3.75 kN/m<sup>2</sup> and 1 kN/m<sup>2</sup> floor finish are taken. The masonry walls loads are 230 mm thick on the outside and 115 mm thick on the inside are assumed. The live load on all slabs is considered 2 kN/m<sup>2</sup>. IS 1893 is used to calculate seismic load, and zone factor 0.16, importance factor 1, response reduction factor 5, and medium soil strata are taken for analysis.

**Nonlinear modelling**

Buildings are designed using IS 456 and IS 1893 codes, followed by linear static and dynamic analysis. IS 1893 suggests decreasing structural elements' moment of inertia, thus present work is incorporated strong columns and weak beams approach. RC beams and columns with lumped plasticity were modelled in SAP 2000. User-defined plastic hinges are applied to both ends of columns and beams at a distance 5% of beam's length. Table 2 is shown the plastic rotation capacity approval requirements and modelling parameters for immediate occupancy, life safety, and collapse prevention. Plastic hinges are given flexure hinges in the M<sub>3</sub> moment for beams and columns, and P-M<sub>2</sub>-M<sub>3</sub> for columns. The pushover curve is determined at 4% lateral drift of the building. Acceptance requirements for beam and column hinges are assumed as per FEMA-356 [29] and ATC-40 [30].

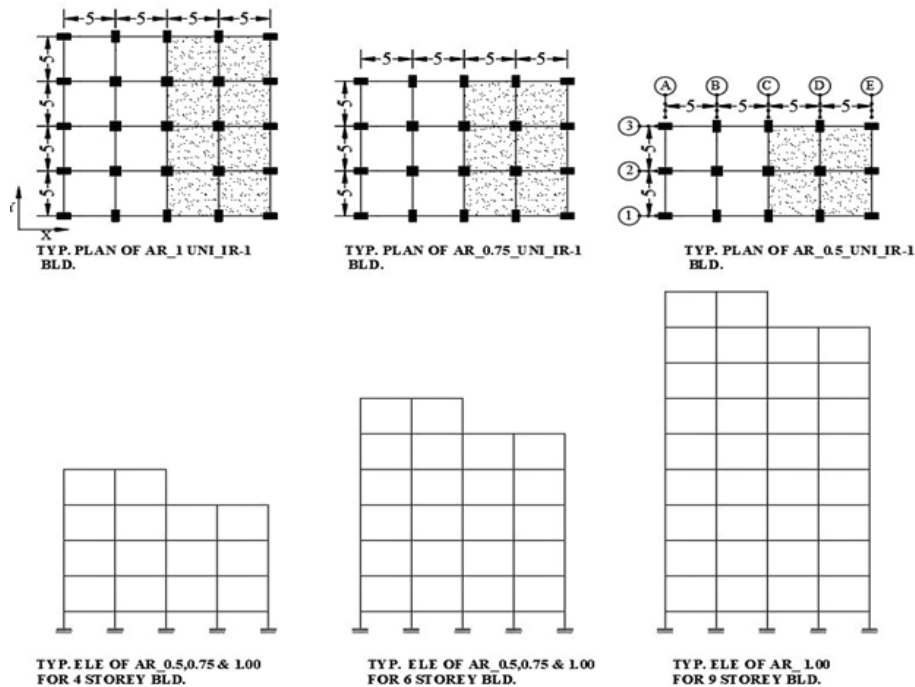


Fig. 4 – Plans and elevations



Table 2 – Plastic rotation limits and acceptance criteria [29-30]

Plastic rotation angle (radians)				
Acceptance criteria for RC beams				
Component type				
IO	Primary		Secondary	
	LS	CP	LS	CP
0.003	0.010	0.015	0.018	0.025
Acceptance criteria for RC columns				
IO	LS	CP	LS	CP
0.003	0.012	0.015	0.018	0.025

**Results and discussion**

The setback kind of vertical irregularity is shown unexpected outcomes due to torsional forces, which are moments or twisting stresses acting on the structure along its vertical axis while performing nonlinear analysis. The structural components of the buildings, such as the columns and beams, are susceptible to experience extra stresses and deformations as a result of these torsional forces. The torsion effect in setback type of reinforced concrete buildings can have significant implications on the structural response and stability of the building. It can result in uneven distribution of lateral loads, such as earthquake loads, leading to irregularities in bending moments, shears, and rotations in the structural components.

Standard 54 pushover curves are developed using a wide range of setback types of buildings and are used to estimate damage at different performance levels of the curve. Sample result of pushover analysis for S4\_AR\_0.5\_UD\_Accl- X dir.\_ case is shown in table 3. For an energy-based seismic index, pushover curves are used to calculate different inelastic energies at various performance levels of the curve; additionally, each incremental step (lateral loading) reducing the stiffness of the building is critically evaluated, and cumulative effects are taken into account to compute a stiffness-based seismic index.

Proposed damage indices are validated with existing Powell and Allahabadi’s [12] and Zameeruddin and K. Sanghale [18] deformation based and strength based damage indices respectively. For the example S4 AR 0.5 X, Fig. 5 depicts a pushover curve with a fitting curve of six-degree polynomial equation. Every incremental step resulted in a progressive loss

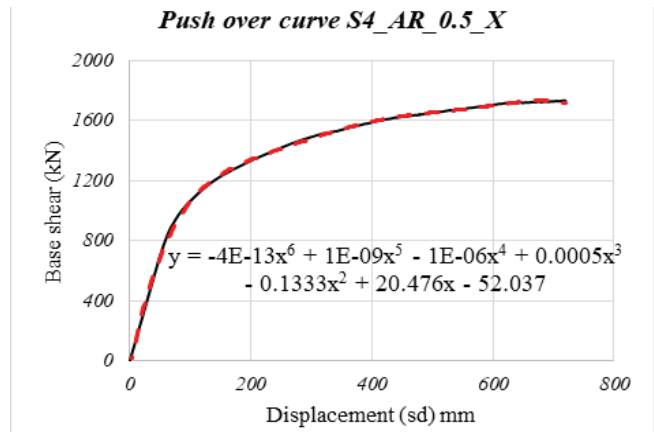


Fig. 5 – Typ. pushover curve with fitting curve and polynomial equation

in stiffness, causing damage to the predefined plastic hinges. Figure 6 is shown, the stiffness of the structure degrades at various performance levels as the drift of the building increases. Sample calculation results of energy based damage index and stiffness based damage index are shown in table 4 and 5 respectively.

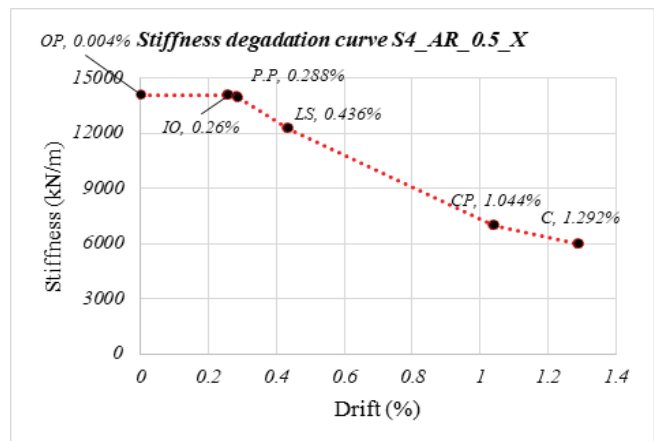


Fig. 6 – Stiffness degradation curve

Out of all examples, 4 storey building with aspect ratio 0.5 case is shown in figure 7 and 8. It has represented drift versus energy and stiffness based damage index, respectively. Total 18 graphs of drift versus energy based DI and 18 graphs of drift versus stiffness based DI have developed to review the overall response of variety of buildings. For all three load scenarios, the drift limit at the performance point in a 4-storey building with an aspect ratio (AR) of 0.5 is about 0.285 % to 0.376 % and 0.331 % to 0.454 % in the x and y directions, respectively. In x and y directions, the energy based DI range was 0% to 4.82 % and 0% to 7.80 %, respectively. Drift is almost the same in aspect ratios (AR) 0.75 and 1.00 as in 0.5



AR, however the energy based DI ranges have been adjusted to 1.93 % to 5.16 % and 0 % to 3.95 % in the x direction and 4.04 % to 8.30 % and 0 % to 4.66 % in y direction, respectively.

For all three load scenarios, the drift limit at performance point in a 6-storey building with an aspect ratio (AR) of 0.5 is found to be 0.296 % to 0.398 % and 0.336 % to 0.475 % in the x and y directions, respectively. In the x and y directions, the energy based DI range is 0 % to 9.19 % and 0 % to 14.98 %, respectively.

The drift is virtually the same in aspect ratio (AR) 0.75 and 1.00 as it is in 0.5 AR, but the energy based DI range for AR 0.75 and 1.00 has been adjusted to 0 % to 5.68 % and 5.34 % to 27.33 % in the x direction and 0 % to 8 % to 7.06 % to 27.87 % in the y direction, respectively.

The drift limit at performance point for all three load cases are illustrated in 9 storey buildings with all aspect ratios, just as it is in a 6-story building. However, with 0.5 AR, the energy based DI range is modified to 12.05 % to 35.92 % and 13.17 % to 33.60

Table 3 – Pushover result for S4\_AR\_0.5\_UD\_Acceleration- X dir.\_ case

Step no.	Disp. (mm)	Base Shear (kN)	A-B	B-IO	IO-LS	LS-CP	CP-C	C-D	D-E	Beyond-E
0	0	0	308	0	0	0	0	0	0	0
1	0.720	10.124	308	0	0	0	0	0	0	0
65	46.80	658.084	307	1	0	0	0	0	0	0
109	78.48	959.858	267	39	2	0	0	0	0	0
261	187.92	1309.10	200	30	77	1	0	0	0	0
323	232.56	1389.94	195	12	63	37	0	0	1	0
530	381.60	1571.62	193	8	20	4	0	0	82	1

Table 4 – EBDI calculation for S4\_AR\_0.5\_UD\_Acceleration load- X dir.\_ case

Step No.	Dis. (mm)	Base Shear (kN)	Per. level	Region	Drift (%)	Area under curve (kN-m)	EBDI (%)	Remarks
0	0	0	-	-	0.000	-	-	Total 308 hinges
1	0.72	10.12	OP	A-B	0.004	-0.037	0.00	First step of Elastic range
64	46.08	647.9	OP	A-B	0.256	-2.376	0.00	Last step of Elastic range
65	46.80	658.0	IO	B-IO	0.260	-2.413	0.40	First hinge formation
72	51.87	722.4	P.P	IO- LS	0.288	-2.639	2.87	P.P @ IO-LS
109	78.48	959.8	LS	IO- LS	0.436	-4.021	17.93	Hinge @ IO-LS
261	187.9	1309	CP	LS- CP	1.044	-9.418	76.77	Hinge @ LS-CP
323	232.5	1389	C	CP-C-D-E	1.292	-11.55	100	Hinge @ D-E

Table 5 – SBDI calculation for S4\_AR\_0.5\_UD\_Acceleration load- X dir.\_ case

Step no.	Drift (%)	Stiffness (kN)	Cumulative-base shear, $\sum K_c \times d_c$ (kN)	Sum. Of base shear, $\sum V$ (kN)	Ratio of col.5/col.4 (%)	SBDI (%)	Remarks
1	0.004	14061.1	10.124	10.124	1.00	0.00	First step
65	0.260	14061.6	42775.41	21716.76	50.77	49.23	First hinge
72	0.288	13935.3	52640.57	26583.31	50.67	49.33	P.P @ IO-LS
109	0.436	12230.6	117713.40	58406.34	49.62	50.38	Hinge @ IO-LS
261	1.044	6966.28	541622.70	235964.1	43.57	56.43	Hinge @ LS-CP
323	1.292	5976.72	763074.19	319764.8	41.90	58.10	Hinge @ D-E

% in the x and y directions, respectively. In the case of aspect ratio (AR) 0.75 and 1.00, the energy based DI range is adjusted to 0 % to 13.66 % and 0 % to 12.89 % in the x direction, and 0 % to 18.10 % and 0 % to 15.34 % in the y direction, respectively.

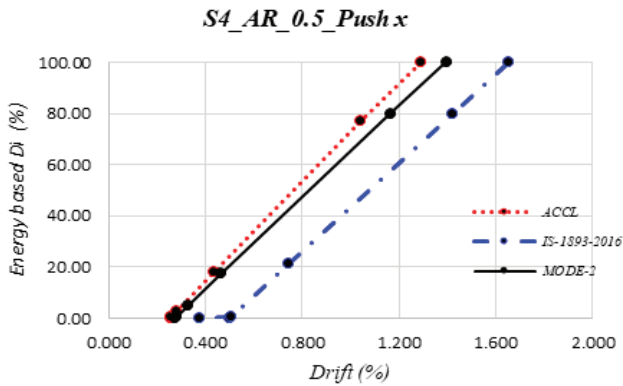


Fig. 7 – Relationship between energy based damage values and drift

Table 6 – Damage indices at performance levels on curve of S4\_AR\_0.5\_X\_Acceleration

Per. level	S <sub>d</sub> (mm)	Drift (%)	Di <sub>E</sub> (%)	Di <sub>K</sub> (%)	Di <sub>P&amp;A</sub> (1988) (%)	Di <sub>Z&amp;K</sub> (2017) (%)
OP	46.080	0.256	0.00	0.00	0.00	0.00
IO	46.800	0.260	0.40	49.23	0.39	46.96
P.P	51.236	0.285	2.87	49.33	2.76	51.62
LS	78.480	0.436	17.93	50.38	17.37	68.83
CP	187.920	1.044	76.77	56.43	76.07	94.14
C	232.560	1.292	100.00	58.10	100.00	100.00

Di<sub>E</sub> = EBDI, Di<sub>K</sub> = SBDI,  
 Di<sub>P&A</sub> = Powell & Allahabadi's deformation based DI [12]  
 Di<sub>Z&K</sub> = Zameeruddin & K. Sanghle's strength based DI [18]

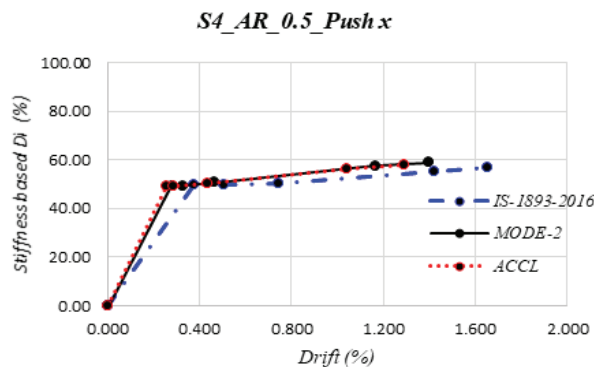


Fig. 8 – Relationship between stiffness based damage values and drift

Table 7 – damage indices at performance point for 4 storey building

Sr. No.	Storey_AR_UD_Dir.	loading type	S <sub>d</sub> (mm)	Drift (%)	Di <sub>E</sub> (%)	Di <sub>K</sub> (%)	Di <sub>D</sub> (P&A 1988) (%)	Di <sub>V</sub> (Z&K 2017) (%)
1	S4_0.5_	Accl.	51.24	0.285	2.87	49.33	2.76	51.62
2	UD_X	IS-1893	67.70	0.376	0.00	49.47	0.00	49.29
3		Mode-2	59.07	0.328	4.82	49.46	4.66	57.77
4	S4_0.5_	Accl.	59.53	0.331	5.73	49.44	4.44	51.26
5	UD_Y	IS-1893	81.79	0.454	0.00	49.56	0.00	45.62
6		Mode-1	76.70	0.426	7.80	49.69	7.57	52.92
7	S4_0.75_	Accl.	51.31	0.285	1.93	49.31	1.86	50.31
8	UD_X	IS-1893	63.98	0.355	5.16	49.55	4.99	61.81
9		Mode-2	58.94	0.327	4.00	49.44	3.88	57.17
10	S4_0.75_	Accl.	57.67	0.320	4.04	49.41	3.92	50.86
11	UD_Y	IS-1893	74.63	0.415	8.30	49.69	8.09	61.07
12		Mode-1	73.63	0.409	6.11	49.58	5.92	50.43
13	S4_1.00_	Accl.	51.39	0.286	1.93	49.31	1.86	50.87
14	UD_X	IS-1893	67.26	0.374	0.00	49.46	0.00	49.91
15		Mode-2	58.88	0.327	3.95	49.44	3.82	58.18
16	S4_1.00_	Accl.	56.31	0.313	3.44	49.39	3.34	51.43
17	UD_Y	IS-1893	75.82	0.421	0.00	49.52	0.00	47.36
18		Mode-1	70.82	0.393	4.66	49.52	4.51	49.40

The drift range for any load pattern did not vary much with building's height, although lateral drift is increased at life safety level in aspect ratio 0.5 in the y direction. In compared to IS 1893 and mode type load patterns, all three structures show larger drift in all aspect ratios. Table 6 shows various damage indices derived for S4 0.5 UD X building example. In any case, DI is assumed to be 100%, which indicates the building is no longer useful. In all cases, the performance point is well within the life safety level drift limit. As shown in table 7, the performance point is reached when the stiffness damage index reaches approximately 50%. As a result, the building experienced more damage as building's stiffness deteriorated.

**Conclusion**

There have been several attempts to estimate seismic damage indices, but the majority of them were based on regular or irregular 2D frames that did not show correct behavior against torsion effects due to vertical irregularity. In order to perform nonlinear analysis, precisely analyses the torsional effects, and provide suitable design solutions for ensuring the structural integrity and stability of setback type buildings, computer-aided analysis and

design techniques are frequently utilized. The torsion effect must be taken into account when designing such buildings in order for estimating their safe and effective performance throughout their service life. It is observed that while nonlinear analysis in particular, short buildings with setbacks, induced a susceptible response and hence demanding more attention for designing to achieve life safety performance level. In past the majority of them collapse under design earthquake. The current analysis is performed on 3D vertical irregular buildings that indicates torsion caused the unexpected nonlinear response, and that torsion makes the structure vulnerable, based on this study the following conclusions can be made.

3D vertical irregular buildings are being analyzed and produces reliable findings, and it has been proved that both recommended approaches can properly estimate the damage to 3D irregular buildings. Both damage indices can be used to calculate damages at any point along the pushover curve. It is considerably more appropriate and efficient to estimate the damages for existing and proposed irregular buildings at any point along the curve. It is suggested that damage at the point of performance be assessed using all three monotonic load pattern types. The main factors influencing absorbed energy and stiffness degradation were load patterns. The proposed damage indices calculate the damage value at the targeted performance levels, which incorporates the contribution of all nonlinear responses at each incremental step of the pushover, addressing the cumulative effects of degrading stiffness that were previously unaccounted for by the existing damage estimations. The pushover curve results are shown in all cases show that the drift is well within permitted limits according to existing standards.

### Compliance with ethical standards

Conflict of interest: On behalf of all authors, the corresponding author states that there is no conflict of interest.

### Acknowledgments

The research described in this paper was not financially supported by any organization.

### References

- Habibi A., Asadi, K., Development of Drift-Based Damage Index for Reinforced Concrete Moment Resisting Frames with Setback, *International Journal of Civil Engineering*, vol.15, 487–498, 2017.
- Pritam H., Arun S. & Satyabrata C., Damage Assessment of Reinforced Concrete Buildings Considering Irregularities, *International Journal of Engineering, Transaction - A*, vol. 32, No.10, 1388-1394, 2019.
- Pritam H., Arjun S. & Satyabrata C., Damage assessment of reinforced concrete-framed building considering multiple demand parameters in Indian codal provisions, *Iranian Journal of Science and Technology, Transactions of Civil Engineering*, vol. 44, 121-139, 2020.
- M. Zameeruddin, and Sangle K., Damage assessment of reinforced concrete moment resisting frames using performance-based seismic evaluation procedure, *Journal of King Saud University - Engineering Sciences*, vol. 33, No. 4, 227-239, 2020.
- Cinitha A, Umesha P.K., Nagesh R. I. and N. Lakshmanan, Performance-based seismic evaluation of RC framed building, *J. Inst. Eng. India Ser. A.*, vol. 96 No. 4, 285-294, 2015.
- A. Vimala and R. Pradeep Kumar, Expended energy based damage assessment of RC bare frame using nonlinear pushover analysis, *Urban Safety of Mega Cities in Asia (Conference) 2014*.
- Pleswara R. K., Balaji. K.V. G. D, Gopal Raju S. S. S.V, and Srinivasa Rao S., Nonlinear pushover analysis for performance based engineering design - A review, *International Journal for Research in Applied Science & Engineering Technology (IJRASET)*, vol. 5 No. 3, 1293-1300, 2017.
- Serkan Etili, and Esra Mete Guneyisi., Seismic performance evaluation of regular and irregular composite moment resisting frames, *Latin American Journal of Solids and Structures*, vol. 17, No. 7, 2020.
- Milind V. M., Pushover Analysis of structures with plan irregularity, *IOSR Journal of Mechanical and Civil Engineering (IOSR-JMCE)*, vol.12, No. 4, 46-55, 2015.
- P. Giannakouras, and C.Zeris, Seismic performance of irregular RC frames designed according to the DDBD approach, *Engineering Structures*, vol. 182, 427-445, 2019.
- A. J. Kappos, Seismic damage indices for RC buildings: evaluation of concepts and procedures, *Construction research communication limited*, 78-87, 1997.
- Powell G.H. & Allahabadi R., Seismic damage prediction by deterministic methods: concepts and procedures, *Earthquake engineering and structural dynamics*, vol. 16, 719-734, 1988.
- Ahmed Ghobarah, H. Abou-Elfath, and A. Biddah, Response-based damage assessment of structures, *Earthquake engineering & structural dynamics*, vol. 28, 79-104, 1999.
- Magdy S. L.Roufaiel and Christian Meyer, Reliability of concrete frames damaged by earthquakes, *Journal of structural engineering*, vol. 113, No. 3, 445-457, 1987.
- A. M. Mwafy, A.S. Elnashai, Static pushover versus dynamic collapse analysis of RC buildings, *Engineering structures*, vol. 23, 407–424, 2001.
- Seong- Hoon Jeong1 and A. S. Elnashai, New Three-Dimensional Damage Index for RC Buildings with planar Irregularities, *Journal of structural engineering*, Vol. 132, No. 9, 1482-1490, 2006.
- S.A. Diaz, L.G. Pujades, A.H. Barbat, Y.F. Vargas, D.A. Hidalgo-Leiva, Energy damage index based on capacity and response spectra, *Engineering structures*, vol. 152, 424–436, 2017.

18. M. Zameeruddin, and Sangle K., Seismic Damage Assessment of Reinforced Concrete Structure using Non-linear Static Analyses, *Korean Society of Civil Engineers - Journal of Civil Engineering*, vol. 2, No. 4, 1319-1330, 2017.
19. Prajapati S. K. and Amin J. A., Seismic assessment of RC frame building designed using gross and cracked section as per Indian standards, *Asian Journal of Civil Engineering*, vol. 20, 821-836, 2019.
20. M. Seifi, J. Noorzaei, M. S. Jaafar and E. Yazdan Pz nah, Nonlinear static pushover analysis in earthquake engineering: state of development, *ICCBT (Conference)*, No. 6, 69-80, 2008.
21. Prahlad Prasad, "Performance based seismic design of steel frame building using energy balance criterion", Ph.D. Thesis, Indian Institute of Technology, Roorkee, 2010.
22. P. Rajeev, K.K. Wijesundara, Energy-based damage index for concentrically braced steel structure using continuous wavelet transform, *Journal of Constructional Steel Research*, vol. 103, 241-250, 2014.
23. Young-Ji Park and Alfredo H.-S. Ang, Mechanistic seismic damage model for reinforced concrete, *Journal of structural engineering*, Vol. 3, No. 4, 722-739, 1985.
24. Julian Carrillo, Damage index based on stiffness degradation of low-rise RC walls," *Earthquake Engineering Structural dynamics*, vol. 44, 831-848, 2014.
25. Edmondo DiPasquale, Jiann-Wen Ju, Attila Askar, and Ahmet S. Qakmak, Relation between global damage indices and local stiffness degradation, *Journal of Structural Engineering*, Vol. 116, No. 5, 1440-1456, 1990.
26. IS: 1893-Part 1 (2016) Criteria for earthquake resistant design of structures, part-1 general provisions and building sixth revision. Bureau of Indian Standards, New Delhi.
27. Bureau of Indian Standard (BIS) (2000) IS456: Indian Standard Plain and Reinforced Concrete, Code of Practice. Bureau of Indian Standards.
28. SAP (2000) Integrated software for structural analysis and design. Computer and Structures, California.
29. FEMA (2000) FEMA - Federal Emergency Management Agency. Pre-standard and commentary for the seismic rehabilitation of buildings, Washington.
30. ATC 40 (1996) - Seismic evaluation and retrofit of existing concrete building. Applied Technical Council, Redwood City (CA).

# Investigation of Impact of Different Conventional and Unconventional Geometries of Tall Building on Wind Flow and Drag Force Using CFD

Kamlesh A. Mehta<sup>1\*</sup> and Rd. Jigar Sevalia<sup>2</sup>

<sup>1</sup>Gujarat Technological University, Ahmedabad, Gujarat, India,

<sup>2</sup>Faculty of Civil Engineering Department, Sarvajani College of Engineering & Technology,  
Surat, Gujarat, 395001, India

The shape of the structure has a strong influence on the wind impacts. The vast majority of tall structures are symmetrical, rectangular, or square in shape. Changing the shape of the building from conventional to unconventional/aerodynamic in order to enhance the behaviour of structures when subjected to wind. The current work used numerical simulations to determine wind-induced drag forces and force coefficients for a variety of unconventional or aerodynamically modified tall building models at 0° wind incidence angle. Numerical analysis of the flow field around conventional and unconventional tall building models is performed using the  $k - \omega$  (SST) and  $k - \epsilon$  (Realizable) turbulence modelling techniques. The results show that the force coefficient is significantly lowered irrespective of the direction of the wind or the degree to which the corner changes from a sharp edge to a smooth curvature surface. Tall buildings with unconventional or aerodynamic designs are proven to be more efficient in reducing loads than tall buildings with conventional shapes.

**Keywords:** Wind Flow, Force coefficient, Computational Fluid Dynamic (CFD), Unconventional Shape, Conventional Shape.

## Introduction:

Urbanization, accommodates the rising demand for commercial and residential space, is a main factor of a country's socioeconomic growth. Many cities in established and developing countries, such as Japan, China, Malaysia, and India, are moving toward the development constructions of tall structures. Tall structures in metropolitan areas, on the other hand, have an impact on the surrounding wind flow pattern. Conventional forms like squares and rectangles have been extensively employed in most nations because of their simplicity, and ease of construction. The unconventional or aerodynamic shape, on the other hand, is always attractive and eye-catching to the observer. The construction of unconventional or aerodynamic shaped tall structures is always a difficult task for architects and designers. In compared to conventional or traditional tall structures, the wind load in this kind of construction is much different. Tall circular, elliptical, octagonal, and square shape buildings with smooth round corners looks attractive.

Hence, in tall buildings structural safety is more critical than a dead load or fixed load. Wind loads are a serious hazard for tall buildings due to their height and slenderness. The building's design and height are very sensitive to horizontal wind loads.

A building's wind resistance is reduced and the wind patterns around it is altered when its shape is modified from conventional to unconventional (i.e. aerodynamic shape). Studies on unconventional tall buildings have concentrated on just one or two aerodynamic alterations on conventional plan shaped tall structures because of the complexity of wind flow in these structures. There have been several studies into the different configurations of "L" and "T" shape tall structures [1], triangular plan form tall buildings [2], and tapering buildings [4,20, 21, 22], as well as the adjustment of corners in constructions [6, 8, 13].

Through the use of an experimental wind tunnel test, Amin and Ahuja [1] estimated the impacts of wind on two rectangle-shaped interfering buildings that were situated in close vicinity to each other and performed as a "L" and "T" plan shaped building, respectively. Banda et al. [2] investigated the aerodynamic characteristics

---

\*Corresponding author.  
Email: mehta\_kamlesh1@gtu.edu.in



of numerous aerodynamic changes in triangle plan shaped tall structures in a wind tunnel. A. Baskaran and T. Stathopoulos [3] used the control volume approach to discretize wind around a block-shaped building in 3-D complex flow circumstances. Deng et al. [4] discovered that a taper-shaped tall structure with chamfered corners and ventilation apertures at the corners is more effective in decreasing wind-induced reactions than a square building. Gomes et al. [6] used a wind tunnel test to characterise the pressure distribution on irregular plan shape structures in the L and U shapes. Li et al. [8] analysed a standard square form model and compared it to chamfered, recessed, and rounded corner models in order to demonstrate how the corners of a traditional square structure effect on wind load reduction. Mathews and Meyer [9] explored two different building geometries in two dimensions for the purpose of numerical modelling of wind loads. Sevalia et al. [11] investigated the wind flow over rectangular bluff bodies and the impact of alternative geometric plan shapes of tall structures on force coefficient, such as square, hexagon, and octagon. Tso et al. [13] investigated chamfered corner recessed models with different aspect ratios in building models and discovered that recessed corners had a considerable influence in lowering both cross-wind and along-wind moments. Verma et al. [14] studied wind angle affects the wind load distribution on square-shaped tall buildings. Kim et al. [20] studied three aeroelastic tapered tall building models with taper ratios of varying 15, 10, and 5% in a wind tunnel that simulated the suburban environment. Tanaka et al. [21] investigated the aerodynamic response of tall structures due to wind and flow characteristics in wind tunnel tests and computational fluid dynamics (CFD) simulation, with the setback model being one of them. Xiu[22] investigated super tall building aerodynamic optimization and its efficacy assessment in terms of tapering, twisting, and stepping, with the goal of minimizing the conflict between the optimization scheme and other design considerations.

In order to estimate the behaviour of wind interaction with structures, the CFD module is utilised than a wind tunnel. CFD can be used to enhance understanding of wind flow over a structure. When wind tunnels are not feasible, CFD numerical simulations might give a great deal of information on physical factors like as pressure, drag force, and so on, across the entire computational domain.

This study focused on the pressure and force coefficients, as well as flow patterns around

conventional and unconventional shape of tall structures, as prescribe by Indian standard Code 875 (Part – 3), 2015. The structures have considered the same plan area and height. For wind incidence angle  $0^\circ$ , the models are investigated using CFD simulation. The change in form of the building from a sharp edge to a rounded edge causes an incredible change in force coefficient, which also affects the wind flow patterns in the wake zone of the tall structure. This study also attempted to address the change in force coefficient, which contributes in the better design of tall building shapes. The drag force value obtained by numerical simulation was used to compute the value of force coefficient on different shapes of conventional and unconventional shaped buildings, and the results were compared to the Indian standard code of practice IS: 875(Part - 3), 2015.

### Theoretical Background

CFD is a part of fluid mechanics that generates a virtual wind tunnel simulation and a data structure to solve fluid flows problem. CFD is a highly useful technology and a great alternative to using a wind tunnel. In CFD, there are several methods available for forecasting the wind effect.

Turbulence models based on large eddy simulation, Reynolds-average Navier Stokes and direct numerical simulation methods [16, 17]. They are hardly used and undesirable for rural wind calculations and wind low investigations because of their high processing costs and difficulties in modification [18, 19]. Furthermore, Janseen W.D. at el. [19] proposed that LES is suitable for wind flow computation, whereas simulations from multiple wind directions are frequently used for pedestrian-level wind flow study [14, 17]. As a result, because transient analysis has a large processing cost, RANS stable analysis is used to calculate wind flow [18, 19]. In CFD software, there are various ways for predicting wind flow and its properties. The turbulence was simulated using two numerical models, namely  $k - \omega$  (SST) and  $k - \epsilon$  (Realizable). The governing equations for the rate of dissipation of fluid flow  $\epsilon$  and the turbulence kinetic energy  $k$ ,  $k - \epsilon$  (Realizable) model are based on transport equations. Equation – 1 represents the transport equation.

$$\frac{\partial}{\partial t}(\rho k) + \frac{\partial}{\partial x_i}(\rho k u_i) = \frac{\partial}{\partial x_i} \left[ \left( \mu + \frac{\mu_t}{\sigma_k} \right) \frac{\partial k}{\partial x_j} \right] + G_k + G_b - \rho \epsilon - Y_m + S_k(1)$$

Where,

Turbulence's kinetic energy is determined by mean velocity gradients and is represented as  $G_k$ . Turbulence's

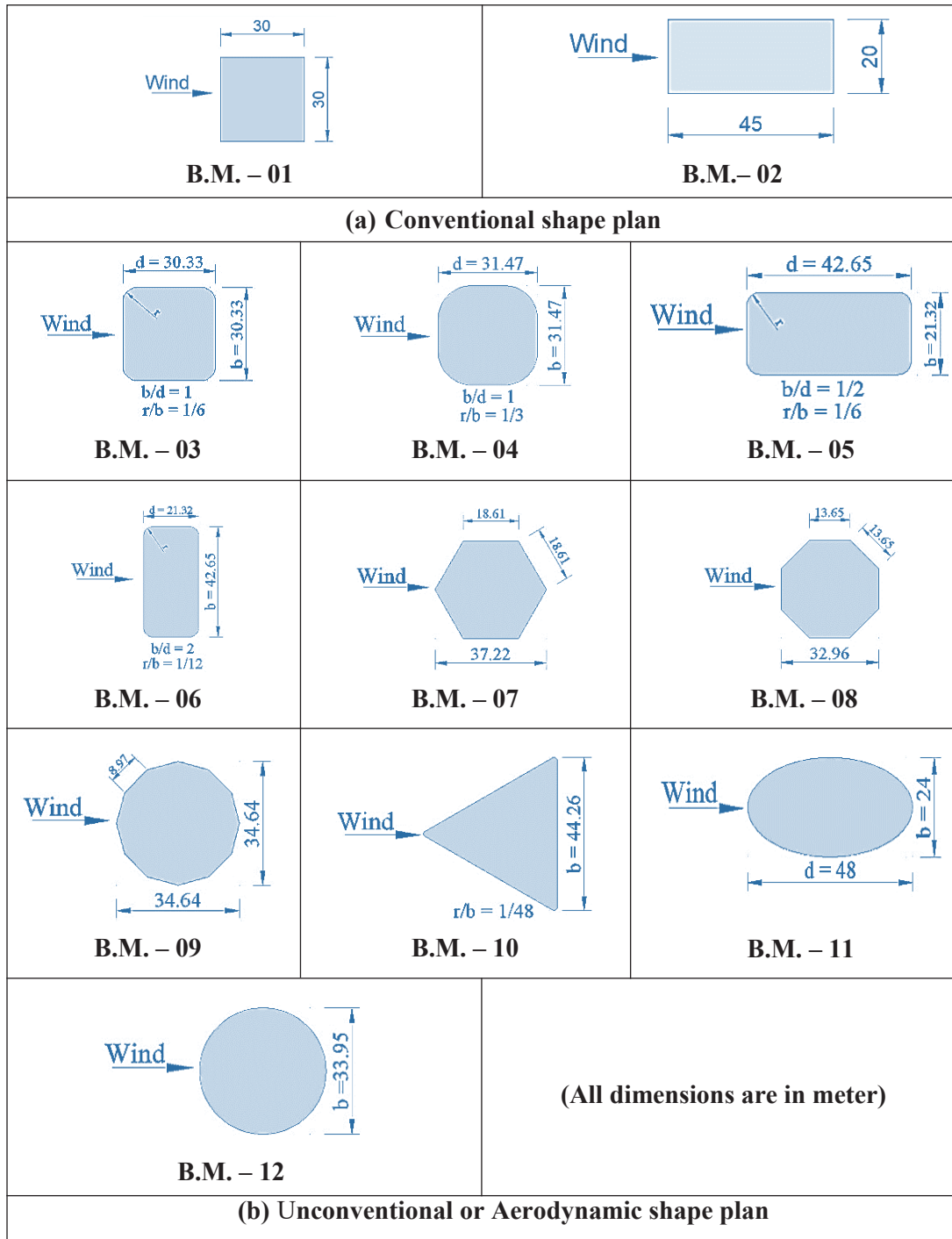


Fig. 1 – Plan of tall buildings.

kinetic energy caused to buoyancy is indicated by  $G_b$  and represents the proportion of variable dilatation to total dissipation in compressible turbulence  $Y_m$ .  $C_2 - \epsilon = 1.9$ , Prandtl number  $\partial k = 1$ , and Prandtl number  $\sigma_\epsilon = 1.2$  are the constants in  $k - \epsilon$  models. Air has a density of  $1.225 \text{ kg/m}^3$ . Back-flow turbulence

was assessed to be 5% intense. Equations-2 and 3 of the  $k - \omega$  (SST) model include a component of derivation of damped cross-diffusion.

$$\frac{\partial}{\partial t}(\rho k) + \frac{\partial}{\partial x_i}(\rho k u_i) = \frac{\partial}{\partial x_i} \left[ \Gamma_k \frac{\partial k}{\partial x_j} \right] + G_k - Y_k + S_k \quad (2)$$

and

$$\frac{\partial}{\partial t}(\rho\omega) + \frac{\partial}{\partial x_i}(\rho\omega u_i) = \frac{\partial}{\partial x_i} \left[ \Gamma_\omega \frac{\partial \omega}{\partial x_j} \right] + G_\omega - Y_\omega + D_\omega + S_\omega \quad (3)$$

Where,  $G_k$  is kinetic energy of turbulence, generated as a result of mean velocity gradients,  $G_\omega$  stands for Generation of  $\omega$ .  $\Gamma_k, \Gamma_\omega$  represents effective diffusivity of  $k$  and  $\omega$  respectively, similarly,  $Y_k, Y_\omega$  represents turbulence dissipates  $k$  and  $\omega$  respectively. Finally,  $D_\omega$  represents cross diffusion and  $S_\omega$  represents source terms.

**Description of Building Models (B.M.):**

Table 1 and Figure – 1 provides details of tall building models. As shown in figure, B.M. – 01 and B.M. – 02 for conventional or traditional shape tall buildings and B.M. – 03 to B.M. – 12 are unconventional or aerodynamic shape tall buildings plan utilised for numerical modelling and had the same plan area. CFD software is used for numerical simulation of wind incidence angle of  $0^\circ$ .

**Methodology:**

A CFD simulation of a bluff body in both a conventional and an unconventional or aerodynamic shape was performed. Domains are the areas of fluid flow in Fluent. Fluid domains define a fluid flow zone.

**Table 1** – Identification of tall building model's conventional and unconventional/aerodynamic shapes.

Identification of the Building Model (B.M.)	Geometrical Configuration
<b>Conventional shape plan</b>	
B.M. – 01	Square with sharpe corner
B.M. – 02	Rectangular with sharpe corner
<b>Unconventional or Aerodynamic shape plan</b>	
B.M. – 03	Square with curve corner $(r/b) = (1/6)$
B.M. – 04	Square with curve corner $(r/b) = (1/3)$
B.M. – 05	Rectangular with curve corner $(r/b) = (1/6)$
B.M. – 06	Rectangular with curve corner $(r/b) = (1/12)$ , corner Vertical orientation
B.M. – 07	Hexagon with sharpe edges corners
B.M. – 08	Octagon with sharpe corner
B.M. – 09	12-Side polygon with sharpe edge corner
B.M. – 10	Triangular sharp edge corner $(r/b) = (1/48)$
B.M. – 11	Elliptical
B.M. – 12	Circular

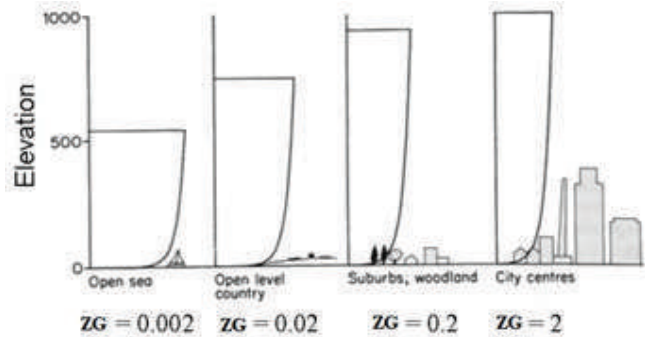


Fig. 2 – Relationship between the height on the earth's surface and prevailing wind speed.

**Basic Wind Speed:**

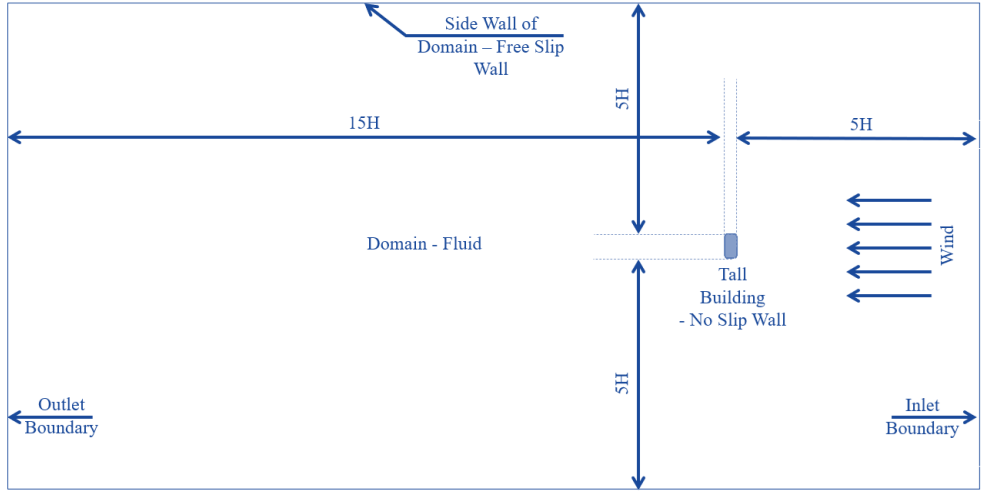
In order to compute design loads on structures, all meteorological stations measure fundamental wind speeds at a height of 10 metres. The design wind speed is calculated by multiplying the fundamental wind speed by factors including probability, roughness of terrain, height, topography, and cyclonic zone importance available in the code of practice [7].

In general, the prevailing wind velocity decreases with height until it is considered smooth and achieves its gradient velocity. Figure – 2 shows the relationship between height above the earth's surface and prevailing wind speed.

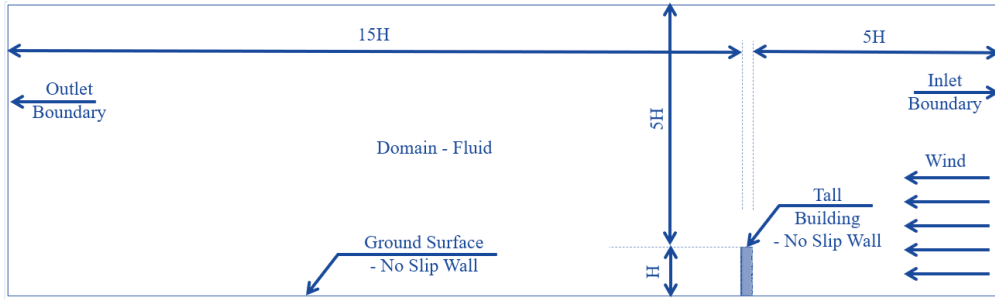
**Boundary Condition:**

The numerical examination for all models was carried out using CFD simulation with the same boundary condition. A tall structure with a conventional or regular shape plan form and an unconventional or aerodynamic shape plan form has the same plan dimension and height, which are replicated in the same domain to verify the research with Indian standard code 875 (Part-3), 2015. To allow for proper flow development, the inlet, lateral, and top walls should be placed 5H (H = Height of building) from the building model, and the outflow boundary should be placed 15H (H = Height of building) behind the building model, as recommended by Franke J. et al. [5] and Revuz et al. [10] as shown in Figure – 3.

The flow direction must be parallel to the boundary surface normal determined at each element face on the inlet boundary to satisfy the direction restriction. The velocity of the fluid at the wall boundary is set to zero for no slip walls (no wall velocity), therefore the velocity boundary condition becomes  $U_{wall} = 0$ . The velocity component parallel to the wall has a finite value for a free slip wall, but the velocity component



(a) 2 - Dimensional plan



(b) 2 - Dimensional elevation

Fig. 3 – Details of domain for numerical simulation under ANSYS - Fluent.

normal to the wall and the wall shear stress are both zero:  $U_{wall} = 0, sw = 0$ . The following power law equation (Equation – 4) is used to determine the velocity profile of the atmospheric boundary layer in the CFD.

$$U_z = U_G \left( \frac{z}{z_G} \right)^\alpha \tag{4}$$

Where,  $z_G$  represents the gradient height, which is assumed to be 10 metres above mean ground level. For terrain category - II,  $U_G$  was 44 m/s mean wind velocity at gradient height.  $\alpha$  is the coefficient of ground surface friction.

According to Jawad S. Touma [12], boundary layer wind flow from the inflow is generated using a power law and  $\alpha$  is parameter that varies with roughness of ground is 0.14 for terrain category – II. As shown in Figure – 4, velocity profiles generated in FLUENT module of CFD ANSYS 2019 R.3. Building walls are

no slip condition but sidewall, building top and top of the domain is free slip condition have considered for numerical simulation.

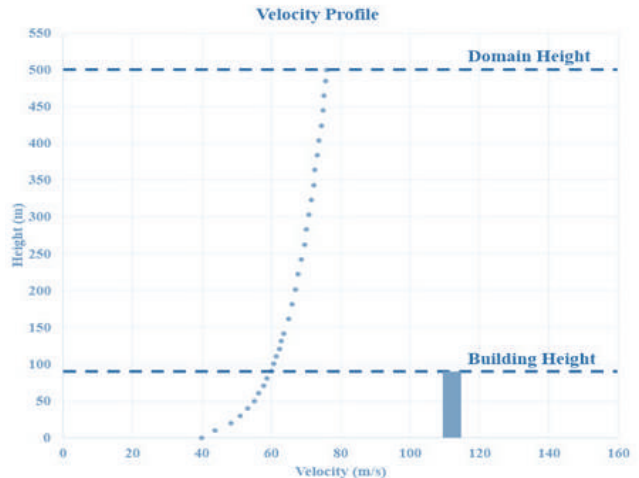


Fig. 4 – Velocity profile.

**Force Coefficient**

Force coefficients are non-dimensional like pressure coefficients. Wind flows never stop when they strike an object, but they may traverse it. The interaction of an object with the wind generates an aerodynamic drag force on a surface as shown in Equation – 5.

$$C_F = \frac{F_D}{\left(\frac{1}{2}\rho AV^2\right)} \tag{5}$$

Here,  $C_F$  represents the force coefficient,  $F_D$  represents the total aerodynamic drag force,  $\rho$  is the density of air [1.225 kg/m<sup>3</sup>],  $A$  is the projected frontal area of tall building, and  $V$  represents the wind velocity at the top of the building.

**Computational Meshing**

Numerical simulating under CFD involves the segmentation of the domain into smaller elements and non-overlapping subdomains, in order to solve the flow physics within the domain that has been established. This greatly helps in the creation of cells in terms of meshing, or elements, within the domain that has been established. When it comes to CFD solutions, the number of meshing cells inside the domain has a considerable influence on the accuracy of the solution. As shown in Figure – 5 for all the models in the simulation tetrahedral meshing is utilised, which was quite efficient. Finer meshing is used around the building and inlet boundary meshing, with a minimum curvature size of elements of 5 m for smooth wind flow transmission and a maximum curvature size of elements of 80 m for the entire domain.

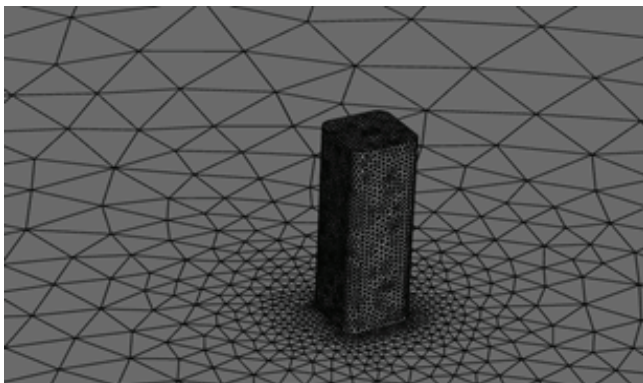


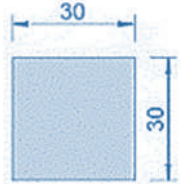

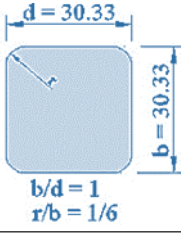
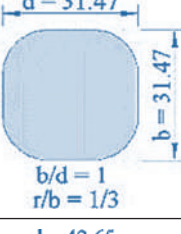
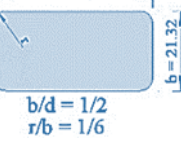
Fig. 5 – Tetrahedral meshing patterns

**Results and Discussion**




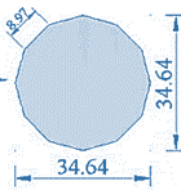
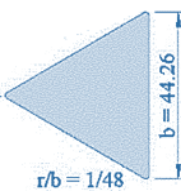
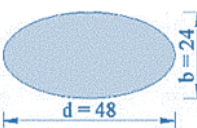

This section will address all the conventional tall building models as well as all of the unconventional or aerodynamic tall building models (B.M.), which were all subjected to numerical simulations. It is

assumed that the wind incidence direction is equal to 0°. As shown in Table 2 and Figure – 6, the estimated wind force coefficients for various tall building shapes using both the  $k - \omega$  (SST) and  $k - \epsilon$  (Realizable) model approaches, which were compared to the Indian standard code 875 (Part-3) in 2015 at a wind incidence angle of 0°, were found to be within acceptable ranges. For the numerical simulation, the height/breath ratio of all the models established as specified by Indian standard code of practice IS: 875(Part 3), 2015 [7].

Table 2 – Force coefficient comparison of different tall building models (B.M.).

Building models (B.M.)	Geometry of B.M.	Force coefficient		
		$k - \epsilon$ (Realizable)	$k - \omega$ (SST)	IS:875 (Part-3), 2015
<b>Conventional shape plan</b>				
B.M.-01		1.132	1.134	1.35
B.M.-02		1.039	1.041	1.00
<b>Unconventional or Aerodynamic shape plan</b>				
B.M.-03		0.445	0.438	0.50
B.M.-4		0.485	0.484	0.40
B.M.-05		0.467	0.466	0.50



B.M.- 6		1.002	1.006	1.07
B.M.- 7		1.132	1.131	1.25
B.M.-8		1.059	1.057	1.15
B.M.- 9		0.915	0.915	0.70
B.M.- 10		0.776	0.756	0.78
B.M.- 11		0.159	0.157	0.20
B.M.- 12		0.461	0.457	0.50

At half the building's height, Figure – 7 shows the flow field around a tall building with conventional and unconventional shape models in horizontal planes. CFD unsteady flow study using the ANSYS/Fluent

software was used to get the wind flow. A power law velocity profile was entered using the user-expression function provided in ANSYS/Fluent to perform all simulations, which were conducted using the  $k - \omega$  (SST) and  $k - \epsilon$  (Realizable) turbulence models, respectively.

Structures such as buildings have substantial effects on the flow conditions in their surroundings. It is first necessary to explain how flows around square and rectangular tall buildings are formed in order to better understand the effects that sharp-edged corners have on these structures. Conventional shapes such as square and rectangular tall buildings are relatively common, and they are particularly sensitive to vortex shedding during high wind events, which can cause them to collapse. As soon as the wind reaches the structure, it starts to diverge; some of it travels around the structure, while the remaining passes over the top of the structure. Due to the building's sharp corners, flow separation occurs, resulting in high-speed corner flow and shear layer separation. This caused the corner flows to merge with the main flow. Recirculating flow occurs at the building's leeward surface as a result of an under-pressure zone, which increases the value of the force coefficient for B.M. – 01 (square shape) and 02 (rectangular shape) to 1.134 and 1.041, respectively. Changes in the cross-section of the building, such as a B.M. – 03 (square with  $r/b = 1/6$ ), a B.M. – 04 (square with  $r/b = 1/3$ ), or a B.M. – 05 (horizontal rectangular shape with  $r/b = 1/3$ ), improve wind flow around the building corners by reducing the area of the high wind speed zone near the building corners due to reduced deviation of separated flow, as showed in Figure – 7. The wake width of the B.M. – 03, B.M. – 04, and B.M. – 05 models is decreased, resulting in an increase in negative pressure (less negative) on the leeward side of the tall building model and a decrease in the wind induced force coefficient for B.M. - 03 (square with  $r/b = 1/6$ ), 04 (square with  $r/b = 1/3$ ), and 05 (horizontal rectangular shape with  $r/b = 1/3$ ) to 0.445, 0.485, and 0.467, respectively.

Increased use of sharp-edged corners in B.M. – 07 (Hexagon with sharpe corners edges), B.M. – 08 (Octagon with sharpe corner), and B.M. – 09 (12-Side polygon with sharpe edge corner) results in a greater reduction in wind pressure coefficient. The cross-sections of B.M. – 08 (Octagonal with sharp edge corner) and B.M. – 09 (12-sided polygon with shape corner) exhibit a high degree of corner. Increased in corner sections promote shear layer reattachment, wake shortening, and a rise in leeward pressure (less

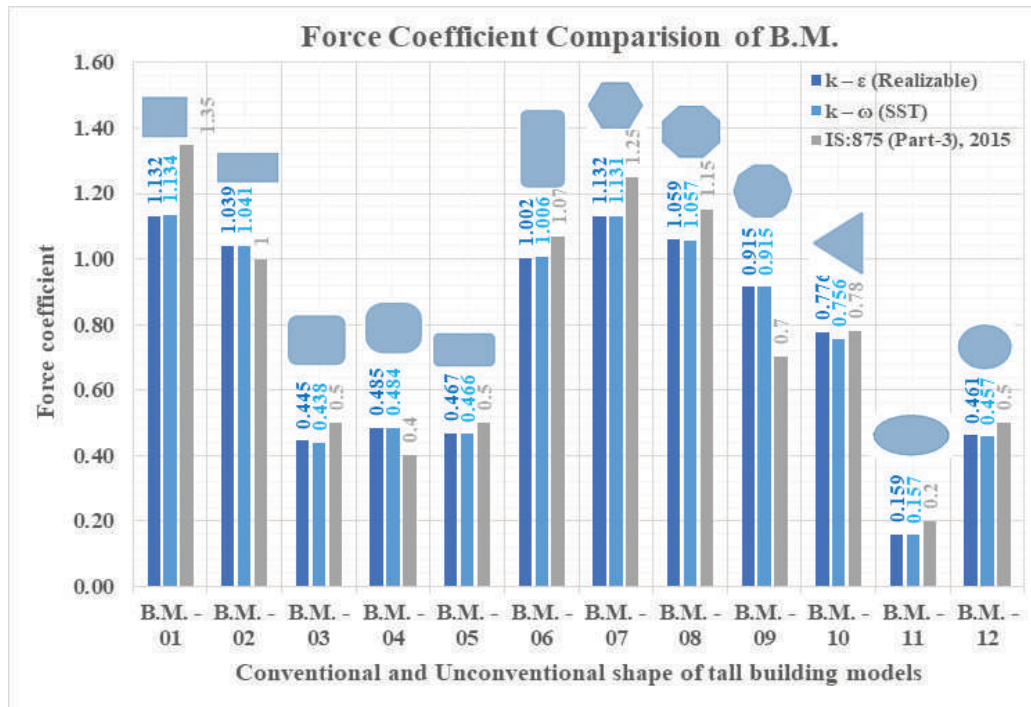


Fig. 6 – Force coefficient comparison of building models (B.M.).

negative), hence reducing body force coefficient to 1.059, and 0.915 respectively.

The two-incline sides of the B.M. – 10 (triangular sharp edge corner with  $r/b = 1/48$ ) have been considered towards the wind ward side and blunt side at leeward side. This results to change in a wind flow patterns due to increase in shear layer separation from the corner of the inclined face of tall building at leeward side, as illustrated in Figure – 7. The wake width of the B.M. – 10 is increased with increase in length of the blunt side, resulting in an increase in negative pressure on the leeward side of the tall building compared with B.M. – 06 (Rectangular with curve corner (1/12), Vertical orientation), and decreases in the wind induced force coefficient to 0.776 and 1.006.

The wake width of B.M. – 11 (elliptical), and B.M. – 12 (circular) models is reduced, resulting in an increase in negative pressure (less negative) on the leeward side of the building model and a reduction in wind generated drag force to 0.159 and 0.461 respectively.

### Conclusion:

The current findings shown that at wind incidence angles of  $0^\circ$ , various unconventional or aerodynamic geometries of tall buildings may generate significantly

different drag forces than a conventionally shaped building. However, it is meant to be utilised critically in the future when designing tall buildings. The findings from both turbulence models have been presented in a way that is typically similar to the Indian Standard Code of Practice IS:875 (Part-3), 2015, with variances ranging from 5% to 25%.

The study's main findings are summarized as follows:

- Modifications to structural or aerodynamic layout may reduce wind-induced loads on taller buildings.
- Wind flow around a tall structure is influenced by aerodynamic changes to the geometry of the building, whether large or small.
- Minor modifications to square and rectangular corner rounding (with a smaller or larger radius), increased corner edges (hexagon, octagon, 12-sided polygon), smooth curvature surface (elliptical, round), and other shapes improve shear layer reattachment and reduce wake width on the leeward side of the tall building, thereby lowering drag force and force coefficients.
- Due to the round corners and smoothness are more effective at reducing both force coefficient and drag force than sharp-edged corners, particularly for traditional designs such as square and rectangular shapes.



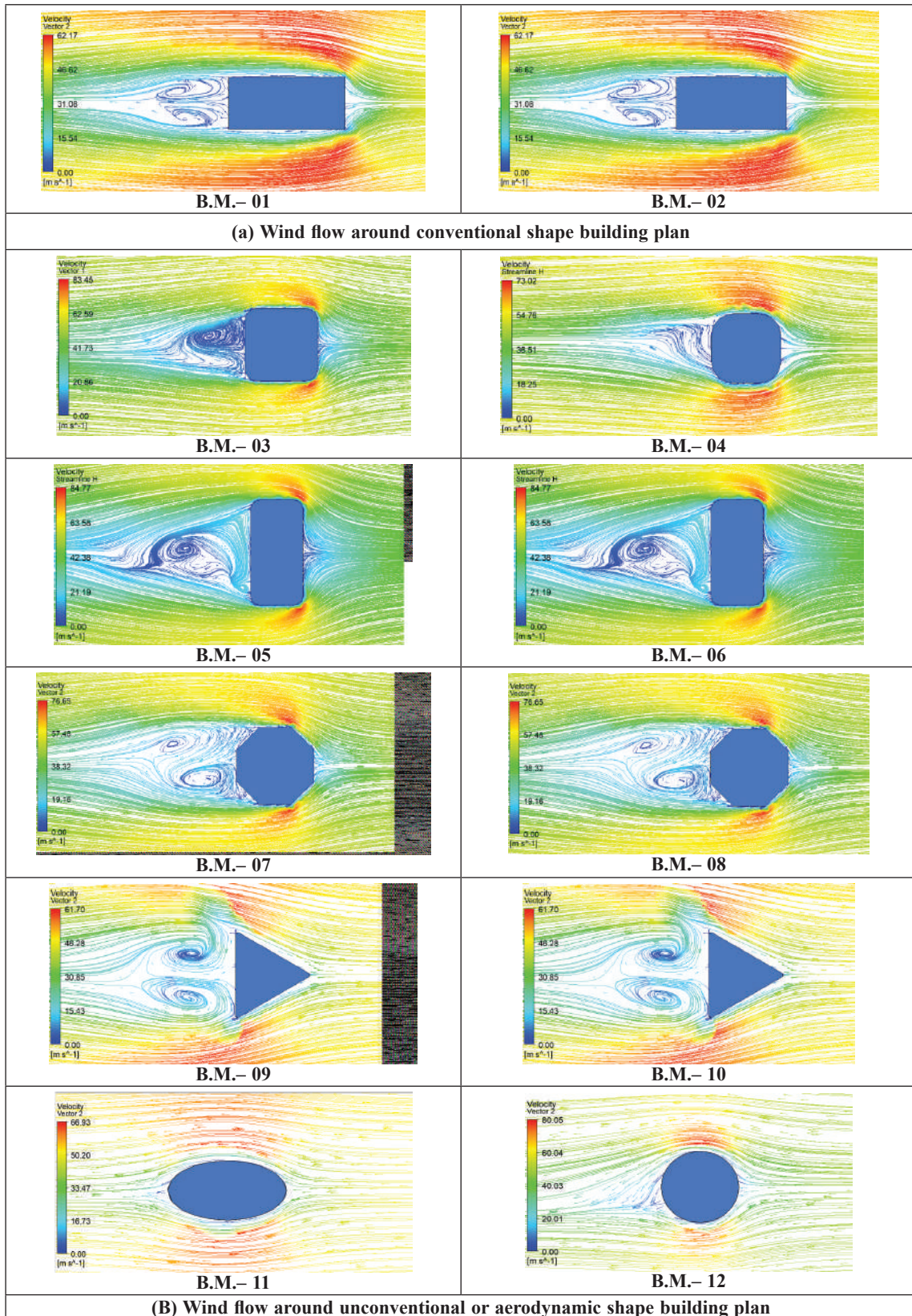


Fig. 7 – Aerial view of a velocity vector around tall building for 0° wind incidence angle.

- As the number of sides rises, B.M. – 09 exhibits a more noticeable sharp edge corner effect than B.M. – 07 or B.M. – 08.
- For wind incidence angles of  $0^\circ$ , a CFD numerical technique based on  $k - \epsilon$  (Realizable) turbulence models predict good agreement for various shapes with smooth surfaces and tetrahedral meshing. The  $k - \omega$  (SST) turbulence model revealed excellent agreement for the various shape of the building with a sharp edge corner. Both turbulence models gave very comparable results.

### Compliance with ethical standards

Conflict of interest: On behalf of all authors, the corresponding author states that there is no conflict of interest.

### Acknowledgments

The research described in this paper was not financially supported by any organization.

### References

- 1 Amin, J. A., and A. K. Ahuja. "Experimental study of wind-induced pressures on buildings of various geometries." *International Journal of Engineering, Science and Technology*, 3.5, 2011.
- 2 Bandi, Eswara Kumar, et al. "Experimental investigation on aerodynamic characteristics of various triangular-section high-rise buildings." *Journal of Wind Engineering and Industrial Aerodynamics*, 122, 60-68, 2013.
- 3 Baskaran, A., Stathopoulos, T.: Computational evaluation of wind effects on buildings. *Building and Environment*, 24(4), 325 – 333, 1989.
- 4 Deng, Ting, Xianfeng Yu, and Zhuangning Xie. "Aerodynamic measurements of across-wind loads and responses of tapered super high-rise buildings." *Wind & structures*, 21.3, 331-352, 2015.
- 5 Franke, J., Hirsch, C., Jensen, A., Krus, H., Schatzmann, M., Westbury, P., Miles, S., Wisse, J., Wright, N.: "Recommendations on the use of CFD in predicting pedestrian wind environment." *Cost action C*. Vol. 14. 2004.
- 6 Gomes, M. Glória, A. Moret Rodrigues, and Pedro Mendes. "Experimental and numerical study of wind pressures on irregular-plan shapes." *Journal of Wind Engineering and Industrial Aerodynamics*, 93.10, 741-756, 2005.
- 7 IS: 875 (Part 3), 2015: Indian standard code of practice for design loads (other than earthquake) for buildings and structures, part - 3 (Wind Loads) 2015. Bureau of Indian Standards, New Delhi 2015.
- 8 Li, Yi, Q. S. Li, and Fubin Chen. "Wind tunnel study of wind-induced torques on L-shaped tall buildings." *Journal of Wind Engineering and Industrial Aerodynamics*, 167, 41-50, 2017.
- 9 Mathews, E. H., and J. P. Meyer. "Numerical modelling of wind loading on a film clad greenhouse." *Building and Environment*, 22.2, 129-134, 1987.
- 10 Revuz, Julia, D. M. Hargreaves, and J. S. Owen. "On the domain size for the steady-state CFD modelling of a tall building." *Wind and structures*, 15.4, 313, 2012.
- 11 Sevalia, Jigar K., A. K. Desai, and S. A. Vasanwala. "Effect of geometric plan configuration of tall building on wind force coefficient using CFD." *International Journal of Advanced Engineering Research and Studies*, 1, 127-130, 2012.
- 12 Touma, Jawad S. "Dependence of the wind profile power law on stability for various locations." *Journal of the Air Pollution Control Association*, 27.9, 863-866, 1977.
- 13 Tse, Kam-Tim, et al. "Economic perspectives of aerodynamic treatments of square tall buildings." *Journal of Wind Engineering and Industrial Aerodynamics*, 97.9-10, 455-467.2009.
- 14 Verma, S. K., A. K. Ahuja, and A. D. Pandey. "Effects of wind incidence angle on wind pressure distribution on square pan tall buildings." *Journal of Academic Industrial Research*, 1.12, 747-752, 2013.
- 15 Canonsburg, ANSYS, Inc. ANSYS ICEM CFD Tutorial Manual, 15317, 1 – 320, 2012.
- 16 Mochida, Akashi, et al. "Comparison of various k-ε models and DSM applied to flow around a high-rise building-report on AIJ cooperative project for CFD prediction of wind environment." *Wind and Structures*, 5.2\_3\_4, 227-244, 2002.
- 17 Blocken, Bert. "Computational Fluid Dynamics for urban physics: Importance, scales, possibilities, limitations and ten tips and tricks towards accurate and reliable simulations." *Building and Environment*, 91, 219-245, 2015.
- 18 Hang, Jian, Mats Sandberg, and Yuguo Li. "Effect of urban morphology on wind condition in idealized city models." *Atmospheric Environment*, 43.4, 869-878, 2009.
- 19 Janssen, W. D., Bert Blocken, and Twan van Hooff. "Pedestrian wind comfort around buildings: Comparison of wind comfort criteria based on whole-flow field data for a complex case study." *Building and Environment*, 59, 547-562, 2013.
- 20 Kim, Yong Chul, and Jun Kanda. "Wind pressures on tapered and set-back tall buildings." *Journal of Fluids and Structures*, 39, 306-321, 2013.
- 21 Tanaka, Hideyuki, et al. "Experimental investigation of aerodynamic forces and wind pressures acting on tall buildings with various unconventional configurations." *Journal of Wind Engineering and Industrial Aerodynamics*, 107, 179-191.2012.
- 22 Xie, Jiming. "Aerodynamic optimization of super-tall buildings and its effectiveness assessment." *Journal of Wind Engineering and Industrial Aerodynamics*, 130, 88-98, 2014.

**Statement about the ownership and other particulars about newspapers  
JOURNAL OF THE MAHARAJA SAYAJIRAO UNIVERSITY OF BARODA**

(To be published in the first issue every year after the last day of February)

**FORM IV**

(See Rule 8)

1. Place of the Publication : The The Maharaja Sayajirao University of Baroda  
M.S. University of Baroda, Vadodara - 390 002.
2. Periodicity of its Publication : Science & Technology  
at any time during the year.
3. Printer's Name : Shri Jatin H. Somani  
Nationality : Indian  
Address : Offg. Manager, The M.S.University of Baroda Press,  
(Sadhana Press), Vadodara - 390 001.
4. Publisher's Name : Prof. P. K. Jha  
Nationality : Indian  
Address : The M. S. University of Baroda,  
Vadodara - 390 002.
5. Editor's Name : Prof. P. K. Jha  
Nationality : Indian  
Address : The M. S. University of Baroda,  
Vadodara - 390 002.
6. Names & Addresses of Individuals : The M. S. University of Broda,  
who own the newspaper and Vadodara - 390 002.  
partners or shareholders holding  
more than one percent of the  
total capital

I, C. N. Murthy declare that the particulars given above are true to the best of my knowledge and belief.

**Prof. P. K. Jha**



## **JOURNAL OF THE MAHARAJA SAYAJIRAO UNIVERSITY OF BARODA**

The Journal is mainly intended to publish original research papers contributed by the teachers and research scholars of the M.S. University of Baroda.

One volume of the Journal is issued every year in three parts. These parts are devoted respectively to topics relating to Humanities, Social Science, Science & Technology, Medicine. All manuscripts, books and publications for review should be addressed to :

The Editor (Science & Technology),  
Journal of the M.S. University of Baroda,  
A.I.C.S. Training Centre,  
Baroda - 390 002.

email: [editor.msujst@gmail.com](mailto:editor.msujst@gmail.com)

Contributors are requested to submit manuscripts, by email attachment which should be typed with double spacing and on one side of the paper only. Authors are advised to retain a copy of the paper that they send for publication as the Editors cannot accept responsibility for any loss.

Authors of papers printed in the Journal are entitled to one copy of the issue free of charge.

### **ADVERTISEMENT**

All advertising matters should be send so as to reach the office of the Journal a month before the publication of the Journal. Further information on rates and space can be had on writing to [\*\*editor.msujst@gmail.com\*\*](mailto:editor.msujst@gmail.com).



"The full-blown lotus growing out of the lake symbolises the emergence of the mind and its triumph over matter. The flame rising from the center of the lotus is the flame of the human knowledge, spreading light and learning for the coming generations. The motto inscribed below the lotus defines the purpose and existence of life which is love of beauty, goodness and intellectual curiosity."

## महाराजा सयाजीराव विश्वविद्यालय गीत

अमे वडोदराना विद्यापीठनां सपनां सारवनारा  
अमे ज्योत जलावी सृष्टि नवली सहसा सर्जनहारा.

अमे गगनकुसुम कर धरनारा  
अमे मगन मगन थई फरनारा  
अगनबाथ अमे भरनारा  
अमे दैन्यतिमिरने हरनारा.

श्री सयाजी विद्यापीठना ज्ञानदीपने धरनारा  
सत्यं शिवं सुन्दरम् नो मंत्र अनंतर भणनारा.

*सयाजीराव*